A study of spatial structures of bremsstrahlung continuum and Z_{eff} based on visible spectroscopy in LHD

Zhou Hangyu

Doctor of Philosophy

Department of Fusion Science
School of Physical Sciences
The Graduate University for Advanced Studies

2010 (School Year)

Abstract

Impurity control is significantly important to reduce substantial power loss and to achieve high performance plasmas in controlled nuclear fusion research. Effective ion charge, Z_{eff}, is a key parameter to characterize the impurity contents in fusion plasmas and the radial distribution gives clear information on the impurity transport. The Z_{eff} value has been observed using bremsstrahlung continuum in high-temperature plasmas. A Z_{eff} diagnostic system based on a visible spectrometer has been newly designed and constructed instead of an old interference filter system in Large Helical Device (LHD) to eliminate line emissions and to obtain Z_{eff} in low-density plasmas. An astigmatism-corrected Czerny-Turner-type visible spectrometer coupled with a charge coupled device (CCD) has been installed with a 44-channel optical fiber array to detect the visible bremsstrahlung continuum profile in LHD. The diagnostic system has been absolutely calibrated with a standard tungsten lamp and an integrated sphere to analyze the visible bremsstrahlung continuum at 530nm quantitatively.

A full vertical bremsstrahlung profile ($-0.6\text{m} \leq Z \leq 0.6\text{m}$) has been successfully observed for horizontally elongated plasma cross section in both discharges using H_2 gas-puffing at normal density range ($n_e \leq 10^{14}\text{cm}^{-3}$) and solid H_2 multi-pellet injection at extremely high-density range ($n_e \geq 10^{14}\text{cm}^{-3}$). The line emissions are entirely eliminated from the signal due to the high spectral resolution with which the bremsstrahlung continuum can be clearly separated from spectral lines, whereas nonuniform bremsstrahlung emission originating in the ergodic layer is indentified in the radial profile for the normal discharges with outwardly shifted magnetic axis configurations ($R_{ax} > 3.60\text{m}$). At present, the lower half of the vertical bremsstrahlung profile ($-0.6\text{m} \leq Z \leq 0\text{m}$) is applicable to the Z_{eff} profile analysis for the gas-puff discharges in inwardly shifted magnetic axis configurations ($R_{ax} \leq 3.60\text{m}$). On the contrast, the vertical bremsstrahlung profile measured from the pellet discharges is fully available for the Z_{eff} profile analysis in all the magnetic axis configurations because the plasma edge boundary shrank in the high-density operation and the nonuniform bremsstrahlung emission disappeared.

Local bremsstrahlung emissivity profile has been derived from the vertical bremsstrahlung profile as a function of normalized minor radius, ρ, through Abel inversion taking finite β-effect into account. Errors in the calculation due to the magnetic surface distortion have been examined with uncertainty of the edge plasma boundary. The result

indicates that determination of the normalized minor radius for each observation chord gives the largest influence on the error estimation rather than the chord length determination. Thus, the Z_{eff} profile has been calculated from the radial bremsstrahlung emissivity profile by considering the temperature and density profiles in a wide density range of $3.0 \leq n_e \leq 30\times10^{13}cm^{-3}$ and for a variety of density profiles. The Z_{eff} values measured in the present system are checked by neutral-beam-heated discharges with H_2 and C pellet injections, in which the Z_{eff} values should be close to 1 and 6, respectively. The result shows a good agreement between the measurement and the estimation. The line-averaged Z_{eff} value decreases from 3.8 to 1.4 as the density varies from 3 to $9\times10^{13}cm^{-3}$ in the gas-puff discharges with R_{ax}=3.6m, while it keeps a constant value close to 1.0 for density range of 9 to $30\times10^{13}cm^{-3}$ in the pellet discharges with R_{ax}=3.85m. The Z_{eff} profiles have been extensively analyzed in the LHD discharges. As a result, it is found that the Z_{eff} profile becomes generally flat in helical plasmas even if the density profile is changed to peaked, flat or hollow one. It indicates that the impurity partial pressure is radially constant to the electron or ion pressure.

Total bremsstrahlung radiation has been studied from the visible bremsstrahlung profile by integrating over the whole energy region and plasma volume. The total bremsstrahlung radiation is correlated with several plasma parameters for the gas-puff and pellet discharges. It is found that the total bremsstrahlung radiation quickly increases in proportion to the square of the density for the pellet discharges, while it is roughly constant against the density in the gas-puff discharges. The total radiation loss is entirely dominated by the total bremsstrahlung radiation in the high-density pellet discharges. The ratio of the total bremsstrahlung radiation to the total input power only ranges in 3-10% in the gas-puff discharge. However, the ratio starts to increase with the density in the pellet discharges and reaches 40% at $n_e=30\times10^{13}cm^{-3}$. Flat Z_{eff} profiles are also found not only in the gas-puff discharges but also in the pellet discharges. It strongly suggests that the impurity accumulation is not occurred in the pellet discharges of LHD.

The Z_{eff} profile diagnostics based on the visible bremsstrahlung in LHD has often become difficult because of the presence of the nonuniform visible bremsstrahlung emissions originating in the edge ergodic layer. For solving this problem, an alternative approach to the Z_{eff} profile diagnostics using a space-resolved flat-field extreme ultraviolet (EUV) spectrometer has been newly adopted to detect the bremsstrahlung continuum in the EUV wavelength range of 7.0-7.5nm. The EUV bremsstrahlung intensity profiles have been measured and checked for all the magnetic configurations in LHD. It is found that the nonuniform bremsstrahlung emission can be entirely eliminated by use of the EUV bremsstrahlung. As a result, the Z_{eff} profile has been successfully measured for most of discharges regardless of magnetic field structures of the ergodic layer which can be usually controlled by the magnetic axis shift in the range of $3.5 \le R_{ax} \le 4.1$m. The Z_{eff} profiles measured in the EUV range are compared with those measured in the visible range for inwardly shifted configurations ($R_{ax} \le 3.60$m). The result is in good agreement between the two Z_{eff} profiles. It verifies that the use of the EUV bremsstrahlung continuum is a novel way for the Z_{eff} diagnostics in toroidal plasmas with such nonuniform bremsstrahlung emissions at the plasma edge. Typical analysis on the EUV bremsstrahlung also shows a fairly flat Z_{eff} profile with error bars of ±14% in the outwardly shifted configuration of $R_{ax}=3.75$m at which the Z_{eff} profile diagnostics is not available from the visible bremsstrahlung measurement.

Contents

1 **Introduction** **1**

1.1 Thermonuclear fusion research ··· 1

1.2 Impurity behavior in fusion plasmas ··· 4

1.3 Large Helical Device and impurity research ··· 5

1.4 Aim of the present study ··· 7

1.5 Structure of the thesis ··· 9

References ··· 11

2 **Principle of Z_{eff} diagnostics** **13**

2.1 Bremsstrahlung continuum radiation ··· 13

2.2 Effective ion charge ··· 15

3 **Development of visible spectrometer system** **19**

3.1 Introduction ··· 19

3.2 Visible spectrometer system ··· 20

3.3 System calibration ··· 24

3.4 Experimental results ··· 27

3.4.1 Images and spectra ··· 27

3.4.2 Bremsstrahlung intensity profile ··· 29

3.5 Comparison with old system ··· 32

3.6 Summary ··· 34

Reference ············ 35

4 Reconstruction of bremsstrahlung profile 37

4.1 Introduction ············ 37
4.2 Principle of Abel inversion technique ············ 38
4.3 Slice and stack method based on magnetic geometry ············ 39
    4.3.1 Determination of magnetic geometry ············ 40
    4.3.2 Nonlinear fitting method for integrated bremsstrahlung profile ············ 44
4.4 Error estimation in Abel inversion calculation ············ 44
4.5 Density dependence of bremsstrahlung emission ············ 48
4.6 Summary ············ 50
References ············ 51

5 Analysis of radial Z_{eff} profile 53

5.1 Introduction ············ 53
5.2 Experimental verification of measured Z_{eff} values ············ 54
5.3 Comparison of Z_{eff} profiles among different density profiles ············ 57
5.4 Z_{eff} profiles for NBI discharges with single C pellet ············ 68
5.5 Summary ············ 71
References ············ 72

6 Evaluation of total bremsstrahung radiation 73

6.1 Introduction ············ 73
6.2 Experimental setup ············ 74
6.3 Analysis of total bremsstrahlung radiation ············ 78
6.4 Core bremsstrahlung radiation in different density regimes ············ 79
    6.4.1 Emissivity profile of bremsstrahlung radiation ············ 79
    6.4.2 Density dependence of total bremsstrahlung radiation ············ 82
    6.4.3 Behavior of Z_{eff} ············ 87

6.4.4 Bremsstrahlung radiation from ergodic layer 89

6.5 Summary 91

References 92

7 Alternative approach to Z_{eff} diagnostics 93

7.1 Introduction 93

7.2 EUV spectrometer for bremsstrahlung profile measurement 94

7.3 Comparison between visible and EUV bremsstrahlung profiles 96

7.3.1 Visible and EUV spectra 96

7.3.2 Visible and EUV bremsstrahlung profiles 99

7.4 Analysis of radial Z_{eff} profile from EUV bremsstrahlung 99

7.5 Summary 103

References 104

8 Summary and conclusion 105

Acknowledgements 109

Publications 111

List of Figures

1.1 Key parameter of reaction rate as a function of ion temperature ··· 2

1.2 Toroidal plasmas and external magnetic coils in tokamak and stellarator ··· 3

1.3 Schematic of Large Helical Device ··· 6

2.1 Bremsstrahlung radition from electron-ion coulomb collision ··· 14

2.2 Arrangement of Thomson scattering diagnostics in LHD ··· 16

3.1 Schematic top view of LHD with view line of fiber array ··· 21

3.2 Magnetic surfaces at horizontally elongated plasma cross section and parallel observation chords of fiber array ··· 21

3.3 Optical layout of 300mm astigmatism-corrected Czerny-Turner-type visible spectrometer ··· 23

3.4 Spectral resolution for three gratings as a function of entrance slit width ··· 24

3.5 Absolute sensitivities of three gratings for two entrance widths ··· 25

3.6 Relative sensitivities of two gratings for fiber channels ··· 26

3.7 Output CCD images against wavelength and fiber channel ··· 27

3.8 Typical visible spectra in wavelength range of 450-600 nm at Z = 26mm for high density and low density cases ··· 28

3.9 Vertical profiles of chord-integrated bremsstrahlung intensity and magnetic surface structures with observation chords for R_{ax} = 3.6m and R_{ax} = 3.75m and nonuniform factor as a function of magnetic axis position ··· 30

3.10 Vertical profiles of chord-integrated bremsstrahlung intensity in high-density plasmas with R_{ax} = 3.65m and R_{ax} = 3.95m ··· 31

3.11 Comparison of bremsstrahlung intensity profiles measured by visible spectrometer system and old interference filter system ········ 33

4.1 Circular cross section and coordinate for Abel inversion ········ 38

4.2 Nonaxisymmetric cross section for slice and stack method ········ 39

4.3 Pressure profiles for deriving magnetic surface structures against normalized radius ········ 41

4.4 Magnetic surface structures and electron temperature profiles ········ 42

4.5 Chord-integrated bremsstrahlung intensity, bremsstrahlung emissivity after Abel inversion and normalized errors of intensity for two different fitting curves ········ 43

4.6 Chord-integrated bremsstrahlung intensity, observation chord length and bremsstrahlung emissivity for β = 1.44%(8020) and their normalized errors for different pressure profiles ········ 46

4.7 Chord-integrated bremsstrahlung intensity, observation chord length and bremsstrahlung emissivity for β = 0.33%(8020) and their normalized errors for different pressure profiles ········ 47

4.8 Profiles of chord-integrated bremsstrahlung intensity, electron density profiles and bremsstrahlung emissivity for different density ranges as a function of normalized radius and bremsstrahlung emissivity as a function of the density at ρ = 0.2 ········ 49

5.1 Waveform of electron density with H_2 multi-pellet injection and radial profiles of electron density, electron temperature, bremsstrahlung emissivity and Z_{eff} ········ 55

5.2 Waveform of electron density with C pellet injection and radial profiles of electron density, electron temperature, bremsstrahlung emissivity and Z_{eff} ········ 56

5.3 Waveforms of high-density discharge with multi-pellet injection for peaked density profile ········ 58

5.4 Radial profiles of plasma parameters for a peaked density distribution as a function of normalized radius ρ at t_1 = 1.82 s, indicated in Fig. 5.3 ········ 60

5.5 Radial profiles of plasma parameters for a peaked density distribution as a function of normalized radius ρ at t_2 = 2.17 s, indicated in Fig. 5.3 ········ 61

5.6 Waveforms of stable discharge for flat density profile ········ 63

5.7 Radial profiles as a function of normalized radius ρ at t = 2.53 s, indicated in

Fig. 5.6 ········ 64
5.8 Waveforms of density rise discharge for hollow density profile ········ 66
5.9 Radial profiles as a function of normalized radius ρ at *t* = 1.13 s, indicated in Fig. 5.8 ········ 67
5.10 Discharge waveforms with single C pellet injection ········ 69
5.11 Z_{eff} and carbon ion density profiles for three different times during the density decay phase denoted in Fig. 5.10 as a function of normalized radius ········ 70
6.1 Typical waveforms of gas-puff discharge and pellet discharge and radial profiles of electron density and electron temperature ········ 76
6.2 Calculated bremsstrahlung radiation as a function of wavelength for different central electron temperatures ········ 77
6.3 Typical visible bremsstrahlung profiles and local emissivity bremsstrahlung profiles against normalized radius for gas-puff discharge and pellet discharge ········ 80
6.4 Wavelength-integrated bremsstrahlung radiation per unit volume and bremsstrahlung radiation per unit normalized radius for gas-puff discharge and pellet discharge as a function of normalized radius ········ 81
6.5 Total bremsstrahlung radiation for different magnetic axis configurations as a function of line-averaged electron density ········ 83
6.6 Total radiation loss and total bremsstrahlung radiation as a function of line-averaged electron density in gas-puff and pellet discharges ········ 84
6.7 Ratio of total bremsstrahlung radiation to NBI birth deposition power as a function of line-averaged electron density ········ 85
6.8 Line-averaged effective ion charge and ratio of total number of carbon ions to total number of electrons as a function of line-averaged electron density for different magnetic configurations ········ 86
6.9 Radial Z_{eff} profiles for discharges with different densities in different magnetic configurations as a function of normalized radius ········ 88
6.10 Radial profiles of local bremsstrahlung emissivity at different wavelengths as a function of normalized radius ········ 90

List of Figures

7.1 Arrangement of view chords at horizontally elongated plasma cross section for EUV spectrometer and visible spectrometer ······ 95
7.2 EUV spectrum at 5-24 nm and visible spectrum at 450-600 nm ······ 97
7.3 Visible and EUV bremsstrahlung intensity profiles ······ 98
7.4 Radial profiles of electron density, electron temperature, bremsstrahlung emissivity, Z_{eff} from EUV bremsstrahlung and Z_{eff} from visible bremsstrahlung ······ 101
7.5 Radial profiles of electron density, electron temperature, bremsstrahlung emissivity, Z_{eff} from EUV bremsstrahlung ······ 102

Chapter 1

Introduction

1.1 Thermonuclear fusion research

Exploration of fusion energy source is a critical approach to solve human-faced energy source crisis in the near future. Thermonuclear fusion [1-2] was identified as a possible energy source and investigated through experiments in 1950s. During the past 50 years, remarkable progress [3] has been made in thermonuclear fusion research and major facility aimed at demonstrating Deuterium-tritium (D-T) burning plasmas, i.e., ITER [4], has been planned 20 years ago and has been under construction at present.

The D-T reaction is a promising way to achieve thermonuclear fusion [5] because the reaction rate is entirely large in relatively low ion temperature range, e.g., 10keV, as seen in Fig. 1.1. The D-T reaction is expressed by the following equation;

$$\mathbf{{}_1D^2 + {}_1T^3 \rightarrow {}_2He^4\ (3.52MeV) + n^1\ (14.06MeV),} \tag{1.1}$$

where n is the neutron, He the helium, so called α particle. The subscript and superscript denote the atomic number and the atomic mass unit, respectively. In the fusion reaction, the difference in the biding energy of the atomic nucleus before and after the reaction is opened as the kinetic energy of 3.52 and 14.06MeV. α particles with energy of 3.52MeV maintain high-temperature plasma in the steady state fusion reactor as the internal heating power, so called α heating, whereas the neutron is utilized for the output energy.

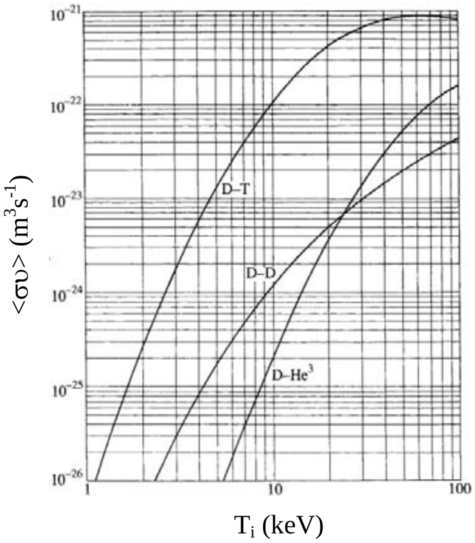

Fig. 1.1. Key parameter of reaction rate, $<\sigma\upsilon>$, as a function of ion temperature for different types of fusion reaction.

The ignition condition for D-T self-burning reaction is fundamentally defined by Lawson criterion [6]. In this criterion, however, the α-heating is not taken into account, assuming that the reactor is sustained only by the external heating source. The corrected ignition condition with the α heating can be then defined by

$$\mathbf{nT\tau_E > 3 \times 10^{21}\ m^{-3}keVs,} \tag{1.2}$$

where n and T are the ion density and the ion temperature, respectively. The symbol of τ_E means the energy confinement time which is defined by ratio of total stored energy to total heating power. Typical parameters for the ignition condition are given by n = 10^{20}m^{-3}, T = 10keV and τ_E = 3s.

Magnetic confinement fusion (MCF) is one of two main approaches to the thermonuclear fusion reactor. In the MCF high-temperature plasmas are totally confined by helical magnetic fields. Two toroidal devices with different magnetic field system, i.e. tokamak and stellarator, exist in the MCF as the most promising candidate for the fusion reactor. In tokamaks, the high-temperature plasma is confined by helical magnetic fields combined toroidal magnetic field from external toroidal magnets with poloidal magnetic field from internal inductive plasma current. In stellarators, on the contrary, the helical magnetic fields are fully generated by external helical magnets. Principles for the plasma confinement in both devices are illustrated in Fig. 1.2. Up to now, the plasma parameters in tokamaks have been close to the reactor condition, so called 'break even'. However, the stellarator has inherent capability [7] of easy access to the steady state operation of the fusion reactor.

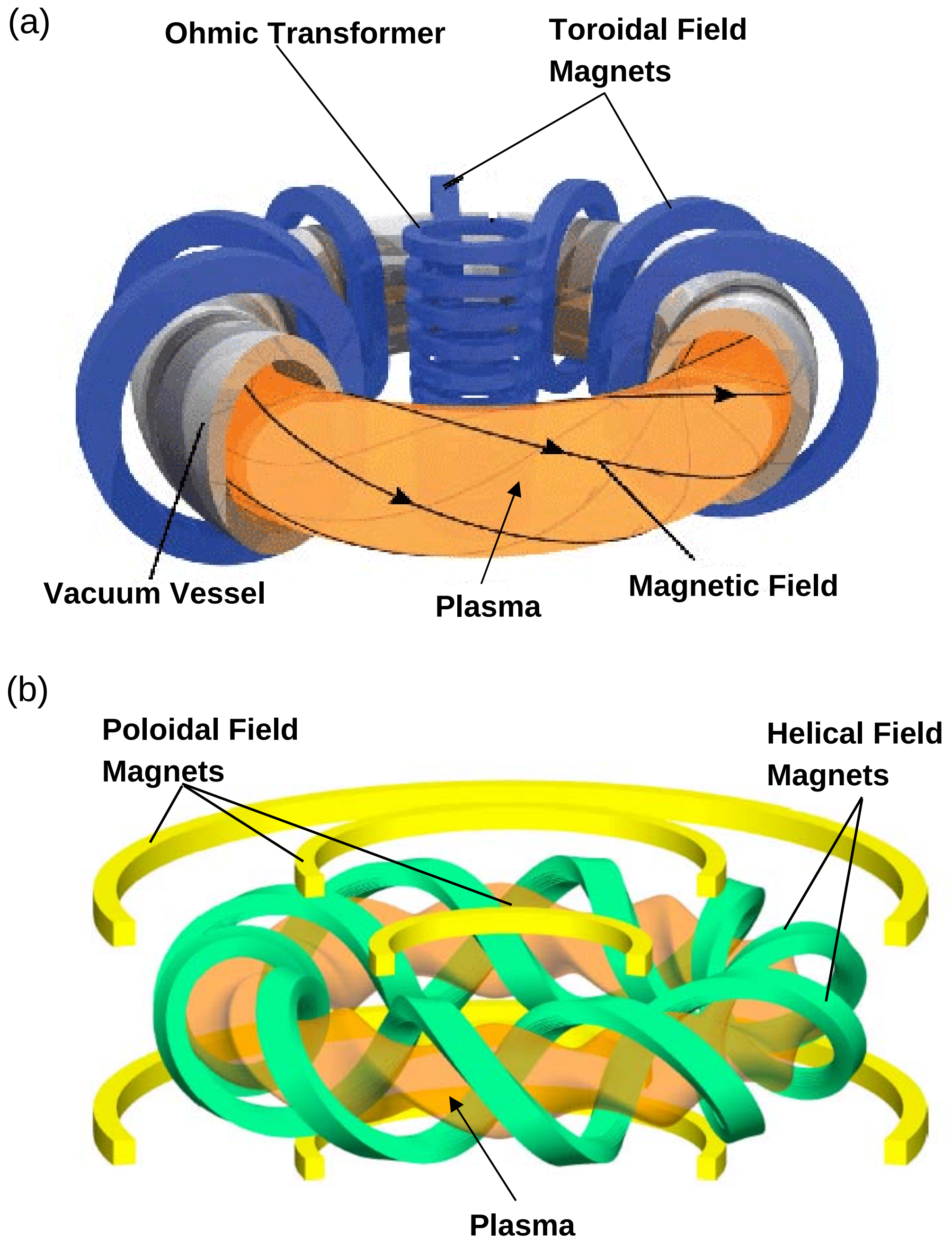

Fig. 1.2. Toroidal plasmas and external magnetic coils in (a) tokamak and (b) stellarator.

1.2 Impurity behavior in fusion plasmas

Impurities [8] play an important role in fusion plasmas. The impurities are mainly produced by sputtering based on the interaction [9] between plasmas and facing in-vessel components, e.g., divertor plates, vacuum vessel wall and radio-frequency antennas. The impurities can be divided into two groups of light impurities, e.g., C, N and O and heavy impurities, e.g., Ti, Fe and W. The light impurities are fully ionized and the heavy impurities are partially ionized in the present high-temperature plasmas because the ionization potential of impurity ions largely increases with the atomic number. At present the light impurity influx is well controlled by carrying out effective wall baking and discharge cleaning. The heavy impurity influx is kept at an extremely low level by installing carbon materials on the vacuum vessel.

Impurity contamination [10] is a critical issue for the fusion devices. The most critical influence of impurities is the radiation loss which leads to degrade the plasma performance. In particular, it is important for the heavy impurities, since the radiation loss quickly increases with the atomic number of impurities. Furthermore, if heavy impurities accumulate [11-12] in the plasma core, the central temperature is easy to drop. The exclusion of the heavy impurities from the plasma core should be also important to obtain the improved confinement such as internal transport barriers (ITBs) [13-14]. On the other hand, the effect of the radiation loss from light impurities on the plasma performance is quite different. The light impurities are fully ionized in the plasma core and the radiation is localized at the plasma edge [15-16]. This is often used to reduce the local heating load on divertor plates and vacuum vessel.

Another important influence of the light impurities is the dilution of the plasma fuel ions which leads to the reduction of the fusion output. The ignition of D-T fusion plasmas can be terminated by the presence of only 3% of carbon. Here, the purity of plasmas is defined by the effective ion charge;

$$Z_{eff} = \frac{\sum_{j,z} n_{j,z} Z_j^2}{\sum_{j,z} n_{j,z} Z_j} = \frac{\sum_{j,z} n_{j,z} Z_j^2}{n_e}, \tag{1.3}$$

where $n_{j,z}$ is the ion density in a charge state of certain ion species, Z_j and n_e the electron density. The value of Z_{eff} is more sensitive to the light impurities, since the concentration of light impurities in plasmas is usually much larger than that of heavy impurities. Z_{eff} is also important in analyzing the plasma resistivity which plays a key role in shaping the plasma current in tokamaks.

1.3 Large Helical Device and impurity research

Large Helical Device (LHD) is the largest superconducting device in the stellarators which consists of a set of l=2 / m=10 continuous helical coils and three sets of poloidal coils, as illustrated in Fig. 1.3. The major specification of LHD is summarized in Table 1.1. LHD is aimed to study the following objectives [17];

a. To achieve high performance steady state plasmas in fusion reactor relevant plasma regime,

b. To solve the existing physical issues in toroidal plasmas

c. To contribute fusion technology development.

Table 1.1 Major specifications in standard configuration of LHD device

Major radius	3.6m
Averaged plasma radius	0.64m
Plasma volume	30m^3
Toroidal magnetic field	2.85T

LHD plasmas are initialized by electron cyclotron heating (ECH) and sustained by hydrogen neutral beam injection (NBI). Working gas is fueled by hydrogen gas puffing for normal discharges ($n_e \leq 10^{14}$cm^{-3}) and by hydrogen multi-pellets injection for high density discharges ($n_e \geq 10^{14}$cm^{-3}). Achieved plasma parameters [17] are listed in Table 1.2. For NBI, three tangential beams based on negative ion sources are employed generating total power of 16MW and one perpendicular beam from positive ion sources produces power of 7MW. ECH from three gyrotrons can supply heating power of 3.5MW. Ion cyclotron resonance heating (ICRH) mainly adopted for steady-state operation produces total power of 2.7MW.

Table 1.2 Achieved plasma parameters

Central ion temperature	13.5keV (n_e=0.3×$10^{19}$$m^{-3}$)
Central electron temperature	10keV (n_e=0.5×$10^{19}$$m^{-3}$)
Central electron density	1.1×$10^{21}$$m^{-3}$ (T_e=0.4keV)
Volume averaged beta	5%
Stored energy	1.62MJ
Fusion triple product	5.0×$10^{19}$$m^{-3}$skeV

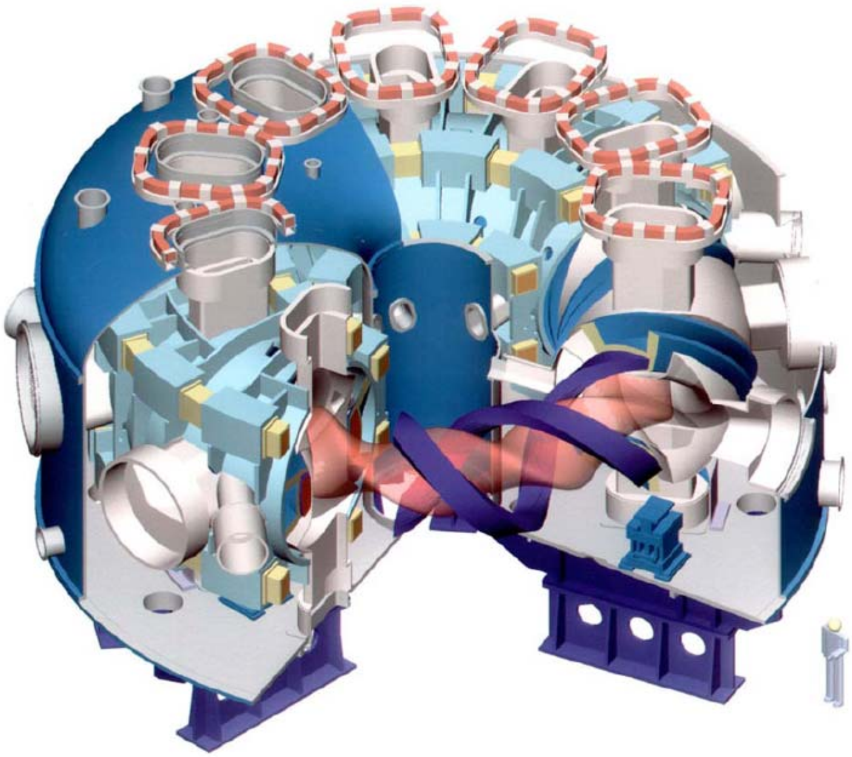

Fig. 1.3. Schematic of Large Helical Device.

Impurity research is one of the critical issues in the LHD experiments. The main impurity in LHD plasmas is carbon. Most of the carbon influxes are believed to originate from the divertor plates on which the magnetic field lines are touched through divertor legs. Another impurity of iron sometimes appears in some magnetic configurations in which the divertor legs are spread out of the divertor plates. Extrinsic impurities such as neon and argon injected with gas puffing are usually used for ion temperature measurement and those such as titanium, molybdenum and tungsten injected through impurity pellet injector are used for the impurity transport and spectroscopic studies. Two favorable mechanisms on the impurity behavior are found in LHD. Impurity screening [18-19] in the plasma edge region with stochastic magnetic fields, so called ergodic layer, is experimentally verified by analyzing the ratio of CV+CVI to CIII+CIV. The impurity screening could be enhanced by increasing the density and changing the edge stochastic magnetic field structures. The experimental results are well reproduced by the three-dimensional edge transport code, EMC3-EIRENE [20]. On the other hand, impurity hole [21] with extremely hollow carbon profile is observed in high-Ti discharges after carbon pellet injection. Impurity transport [22] has been studied using active method [23] combining impurity pellet injection and high-spatial resolution bremsstrahlung measurement. The diffusion coefficient and the convection velocity are derived through a transport code analysis by minimizing residual errors between the experimental and simulated bremsstrahlung intensities. Several passive methods based on radial profile measurements of X-ray (≤0.5nm) [24] and extreme ultraviolet (EUV: ≤50nm) [25-26] impurity line emissions have been also applied to the impurity transport study in LHD.

1.4 Aim of the present study

Study of the impurity transport is fundamentally important in addition to the determination of the impurity concentration for understanding the impurity behavior perpendicular to the magnetic field and for improving the plasma performance in the field of fusion research. In LHD, high-density operation [27] ($n_e > 10^{14}$cm^{-3}) has been achieved in NBI (neutral beam injection) heated plasmas using hydrogen multi-pellets. An alternative direction to the fusion reactor is proposed in such a high-density regime. The study of the impurity content in the high-density regime is important in viewpoint of the increased bremsstrahlung continuum as well as the normal density regime ($n_e < 10^{14}$cm^{-3}) with gas puffing. A variety of density profiles, i.e., peaked, flat and hollow profiles, have been observed in LHD under different experimental conditions, in particular, heating power, fueling method, magnetic axis position, while peaked density profiles are commonly observed as the typical case in tokamaks. It indicates that the particle transport in helical plasmas is quite different from that in tokamak plasmas. Impurity transport study is thus greatly interesting in terms of general understanding of toroidal plasmas on the impurity transport. In addition, it is important to investigate the impurity behavior in discharges with hydrogen and impurity pellet injections [28]. Especially, high-ion temperature discharges [29-30] are achieved by negative-ion-based neutral beam injection after impurity pellet injection, in particular, carbon pellet injection.

For the purposes mentioned above, a new diagnostic system for measuring visible bremsstrahlung profile is planned to obtain spatial structures of Z_{eff} in LHD based on visible spectroscopy. In LHD the bremsstrahlung profile has been measured using an interference filter since 1998 when the LHD experiment was started. The diagnostic system [31] consists of photomultipliers and 82 optical fibers in addition to the interference filter with the transmission band of 6.2nm at the central wavelength of 536.6nm. However, the measurement was disturbed by strong line radiation [32] emitted from the thick ergodic layer [33] at plasma edge characterized by stochastic magnetic fields with length from 10 to 2000m and the presence of high density and low temperature plasmas. Therefore, the new bremsstrahlung measurement system is to be developed based on an astigmatism-corrected Czerny-Turner-type visible spectrometer with a short focal length to eliminate strong line emissions and to measure the bremsstrahlung intensity in lower density regime ($n_e<4\times10^{13}cm^{-3}$). In order to satisfy such conditions, good spectral and spatial resolutions have to be realized with high throughput of the Czerny-Turner-type visible spectrometer. A flat grating and two spherical mirrors were traditionally used for the Czerny-Turner-type spectrometer to transfer the fiber image to the focal plane. However, the astigmatism was always appeared in such a simple spectrometer system. The output image of the circular-shaped fiber had different focal spot sizes on both meridional and sagittal planes. Cross-talks between neighboring channels became something of a serious problem leading to worse spectral and spatial resolutions. The correction of the astigmatism is necessary in the new spectrometer system. In addition, a compact spectrometer is desired to achieve high throughout and to detect sufficient bremsstrahlung intensity even in low density discharges.

Abel inversion technique based on the magnetic surface geometry is also important to obtain the bremsstrahlung emissivity profile from the measured bremsstrahlung intensity profile. The magnetic surface geometry for nonaxisymmetric plasmas in LHD is calculated by variation moments equilibrium code (VMEC) in three-dimensional space. When the bremsstrahlung intensity profile is flat or hollow, the bremsstrahlung emissivity profile is much hollowed after the Abel inversion. A large error is easily transferred to the central profile. In order to solve this problem, the iterative method is required assuming a special function suitable for variation of the bremsstrahlung emissivity profile. The uncertainties can be checked taking into account the profiles of bremsstrahlung intensity, chord length and bremsstrahlung emissivity as a function of the normalized radius in high-β plasmas with a large magnetic axis shift.

1.5 Structure of the thesis

In Chapter 2, the principle of Z_{eff} diagnostics based on bremsstrahlung continuum is introduced. The bremsstrahlung emission due to free-free coulomb collisions between electrons and ions in high-temperature plasmas is evaluated in detail. The value of Z_{eff} is defined by three parameters of bremsstrahlung emissivity, electron density and electron temperature.

In Chapter 3, the visible spectrometer system for the Z_{eff} measurement is presented. An astigmatism-corrected Czerny-Turner-type visible spectrometer coupled with a charge-coupled device (CCD) is installed in LHD to measure the visible bremsstrahlung continuum. A 44-fiber parallel array is equipped to observe a full vertical profile in the horizontally elongated plasma cross section. The system is absolutely calibrated with a standard integrated sphere. Spectral images are checked and excellent performance of the present diagnostic system is verified having no astigmatism. Comparison of bremsstrahlung intensity profiles are presented between the new visible spectrometer system and the old interference filter system.

In Chapter 4, conversion method from the line-integrated bremsstrahlung intensity to the local bremsstrahlung emissivity profile is presented. Abel inversion technique is applied for nonaxisymmetric plasmas with finite β. The slice and stack method based on magnetic surface geometries are used for the Abel inversion. The influence of the magnetic surface distortion due to the finite β effect is examined as error estimation with the influence of unclear edge plasma boundary in the ergodic layer.

In Chapter 5, analysis of radial Z_{eff} profile is performed. Z_{eff} profile is calculated through radial bremsstrahlung emissivity profile as well as radial electron density and temperature profiles. The analysis is done for NBI discharges with H_2 and C pellet injections as a benchmark estimation, in which the Z_{eff} values should be close to 1 and 6, respectively. After the benchmark test the Z_{eff} profiles are analyzed for peaked, flat and hollow density profiles.

In Chapter 6, the total bremsstrahlung radiation power, by which the upper operational density range in the fusion reactor is practically limited, is evaluated in high-density discharges ($n_e \geq 10^{14}cm^{-3}$) with hydrogen pellet injection. After comparison of the bremsstrahlung emissivity profiles between the gas-puff and pellet fueled discharges the total bremsstrahlung radiation power is analyzed with electron density, total radiation and deposited NBI power.

In Chapter 7, alternative approach to Z_{eff} profile diagnostic is presented. The radial profile measurement of Z_{eff} using visible bremsstrahlung (530nm) in LHD has often encountered difficulties in several outwardly shifted magnetic configurations because the intensity profile was largely deformed by the nonuniform visible bremsstrahlung emissions. A space-resolved flat-field extreme ultraviolet (EUV) spectrometer is newly adopted to measure the Z_{eff} profile using the EUV bremsstrahlung continuum in the wavelength range of 7.0-7.5nm. The EUV bremsstrahlung intensity profiles are measured and checked for all the magnetic configurations with totally different magnetic field structures in the ergodic layer of LHD. The Z_{eff} profiles measured in the EUV range are compared with those measured in the visible range for inwardly shifted magnetic configurations. The Z_{eff} profile measured from EUV range is presented for outwardly shifted magnetic configurations.

In Chapter 8, the thesis is summarized and concluded.

References

[1] A. D. Sakharov, *Plasma Physics and the Problem of Controlled Thermonuclear Reactions*, 1961. **1**: p. 21.

[2] L. J. Spitzer, D.J. Grove, W. E. Johnson et al., *Problems of the Stellarator as a Useful Power Source PM-S-14, USAEC NYO-6074*, 1954.

[3] L. A. Artsimovich et al., *Proc. 3rd Int. Conf. on Plasma Physics and Controlled Nuclear Fusion Research*, 1968. **3**: p. 17.

[4] ITER Physics Basis, Nucl. Fusion, 1999. **39**: p. 2137.

[5] J. Wesson, "Tokamaks (Third Edition)", Oxford Univ. Press, 2004.

[6] J. D. Lawson, Proc. Phys. Soc. B, 1957. **70**: p. 6.

[7] A. Iiyoshi et al., Nucl. Fusion, 1999. **39**: p. 1245.

[8] C. D. Michelis and M. Mattioli, Rep. Prog. Phys. , 1984. **47**: p. 1233.

[9] R. Parker, G. Janeschitz, H. D. Pacher et al., J. Nucl. Mater, 1997. **241-243**: p. 1.

[10] R. C. Isler, Nucl. Fusion, 1984. **24**: p. 1599.

[11] J. Stober et al., Nucl. Fusion, 2003. **43**: p. 1265.

[12] H. Takenaga et al., Nucl. Fusion, 2003. **43**: p. 1235.

[13] H. Takenaga et al., Phys. Plasmas, 2001. **8**: p. 2217.

[14] P. C. Efthimion et al., Nucl. Fusion, 1999. **39**: p. 1905.

[15] H. Kubo, S. Sakurai, N. Asakura et al., Nucl. Fusion, 2001. **41**: p. 227.

[16] O. Gruber, A. Kallenbach, M. Kaufmann et al., Phys. Rev. Lett. , 1995. **74**: p. 4217.

[17] A. Komori et al., Nucl. Fusion, 2009. **49**: p. 104015.

[18] M. B. Chowdhuri, S. Morita, M. Kobayashi et al., Phys. Plasmas, 2009. **16**: p. 062502.

[19] M. Kobayashi, Y. Feng, S. Masuzaki et al., Contrib. Plasma Phys., 2008. **48**: p. 255.

[20] Y. Feng, F. Sardei, J. Kisslinger et al., Contrib. Plasma Phys., 2004. **44**: p. 57.

[21] M. Yoshinuma, K. Ida, M. Yokoyama et al., Nucl. Fusion, 2009. **49**: p. 062002.

[22] S. Morita, M. Goto, M. Kobayashi et al., Plasma Sci. Tech., 2009. **11**: p. 402.

[23] H. Nozato, S. Morita, M. Goto et al., Phys. Plasmas, 2004. **11**: p. 1920.

[24] S. Muto and S. Morita, Rev. Sci. Instrum., 2001. **72**: p. 1206.

[25] M. B. Chowdhuri, S. Morita, M. Goto et al., Rev Sci Instrum, 2007. **78**: p. 023501.

[26] C. F. Dong, S. Morita, M. Goto and H. Y. Zhou, Rev Sci Instrum, 2010. **81**: p. 033107.

[27] R. Sakamoto, M. Kobayashi, J. Miyazawa et al., Nucl. Fusion, 2009. **49**: p. 085002.

[28] R. Katai, S. Morita, M. Goto et al., Jpn. J. Appl. Phys., 2007. **46**: p. 3667.

[29] Y. Takeiri, S. Morita, and K. Ikeda et al., Nucl. Fusion, 2007. **47**: p. 1078.

[30] S. Morita, M. Goto, Y. Takeiri et al., Nucl. Fusion, 2003. **43**: p. 899.

[31] H. Nozato, S. Morita, and M. Goto, J. Plasma Fusion Res. SERIES, 2002. **5**: p. 442.

[32] H. Nozato, S. Morita, and M. Goto, J. Plasma Fusion Res. SERIES, 2006. **7**: p. 14.

[33] S. Masuzaki, T. Morisaki, N. Ohyabu et al., Nucl. Fusion, 2002. **42**: p. 750.

Chapter 2

Principle of Z_{eff} diagnostics

2.1 Bremsstrahlung continuum radiation

Bremsstrahlung continuum radiation is emitted from charged particles accelerated by free-free coulomb collision in high-temperature plasmas. Since the mass of electrons is light in weight, the acceleration of electrons is much more dominant than that of ions for the bremsstrahlung radiation. The electron-electron or ion-ion coulomb collision does not emit the bremsstrahlung radiation. The bremsstrahlung radiation is therefore emitted by only the electron-ion coulomb collision.

The acceleration of electrons due to the electron-ion coulomb collision (see in Fig. 2.1) is expressed by

$$a = \frac{F}{m_e} = \frac{Z_i e^2}{4\pi\varepsilon_0 m_e r^2}, \tag{2.1}$$

where r is the distance between electron and ion, Z_i the charge of ion and m_e the mass of electron. The radiation power emitted from the accelerated electron can be given by the following equation [1];

$$P = \frac{e^2}{6\pi\varepsilon_0 c^3}\frac{(\vec{a})^2 - (\vec{v}\times\vec{a})^2 / c^2}{(1 - v^2/c^2)^3}, \tag{2.2}$$

where v is the velocity of electron. If $\left(\frac{v}{c}\right)^2$ << 1, the radiation power can be rewritten by

$$P = \frac{e^2}{6\pi\varepsilon_0 c^3} a^2. \tag{2.3}$$

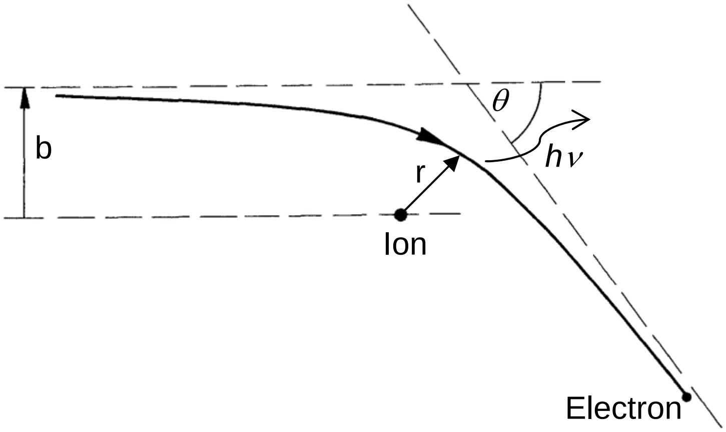

Fig. 2.1. Bremsstrahlung radition from electron-ion coulomb collision

Taking into account the duration of the collision (= 2r/v), the bremsstrahlung radiation power per collision is expressed by the following equation when Eq. (2.1) is substituted into Eq. (2.3);

$$dP = \frac{P2r}{v} = \frac{{Z_i}^2 e^6}{6(2\pi\varepsilon_0 cr)^3 m_e^2 v}. \tag{2.4}$$

Integrating Eq. (2.4) over r, the bremsstrahlung radiation power per unit volume is obtained by the following equation;

$$P_{brem} = n_e n_i \int dPv2\pi r dr = \frac{n_e n_i Z_i^{\,2} e^6}{24\pi^2 \varepsilon_0^3 c^3 m_e^2} \int \frac{1}{r^2} dr, \tag{2.5}$$

where n_e and n_i are the electron and ion densities, respectively. If the value of r is smaller than the minimum limit, the classical process has to be replaced by the quantum mechanics process. Thus, by considering Maxwellian velocity distribution for charged particles the bremsstrahlung radiation power per collision is expressed by [2];

$$P_{brem,\lambda} = \frac{16e^6}{3c^2}\left(\frac{\pi}{6m_e^3}\right)^{1/2} \frac{n_e n_i Z_i^2 g_{ff}}{T_e^{1/2}\lambda^2} \exp\left(-\frac{hc}{T_e\lambda}\right), \tag{2.6}$$

where T_e is the electron temperature and g_{ff} is the free-free gaunt factor. Since various ions in different charge states exist in fusion plasmas, the Eq. (2.6) has to be summed. The bremsstrahlung radiation power per unit volume and per unit wavelength is finally given by

$$P_{brem,\lambda} = \frac{1.89\times 10^{-28} n_e^2 Z_{eff}\, g_{ff}}{T_e^{1/2}\lambda^2} \exp\left(-\frac{12400}{T_e\lambda}\right)\ (\mathrm{W\cdot cm^{-3}\cdot \mathring{A}^{-1}}), \tag{2.7}$$

where the units of n_e, T_e, and λ are given in cm^{-3}, eV and Å, respectively.

2.2 Effective ion charge

Effective ion charge, Z_{eff}, is defined to characterize the impurity content in the fusion plasmas. The Z_{eff} is defined by

$$Z_{eff} = \frac{\sum_{j,z} n_{j,z} Z_j^2}{\sum_{j,z} n_{j,z} Z_j} = \frac{\sum_{j,z} n_{j,z} Z_j^2}{n_e}. \tag{2.8}$$

The value of g_{ff}, is calculated by Karzas and Latter [3]. It weakly depends on T_e and can be approximated by the following relation [4] in the range of 0.03keV ≤ T_e ≤ 10.0keV;

$$g_{ff} = 1.35 T_e^{0.15}. \tag{2.9}$$

From Eq. (2.7), Eq. (2.8) and Eq. (2.9), the Z_{eff} is given by

$$Z_{eff} = \frac{3.92 \times 10^{27} P_{brem,\lambda} T_e^{0.35} \lambda^2}{n_e^2 \exp(-12400/\lambda T_e)}. \tag{2.10}$$

According to Eq. (2.10), the Z_{eff} can be calculated from three parameters of bremsstrahlung emissivity, electron density and temperature. The electron density and temperature are measured by Thomson scattering diagnostics [5] in LHD, by which the entire profiles along major radius on the mid-plane can be observed as shown in Fig.2.2. The radial profiles of T_e and n_e consisting of 200 data positions can be measured with spatial resolution of 1.5~3cm and temporal resolution of 1~100ms. The radial profile of the visible bremsstrahlung emissivity is measured with an absolutely calibrated visible spectrometer system which is explained in the following chapters in detailed.

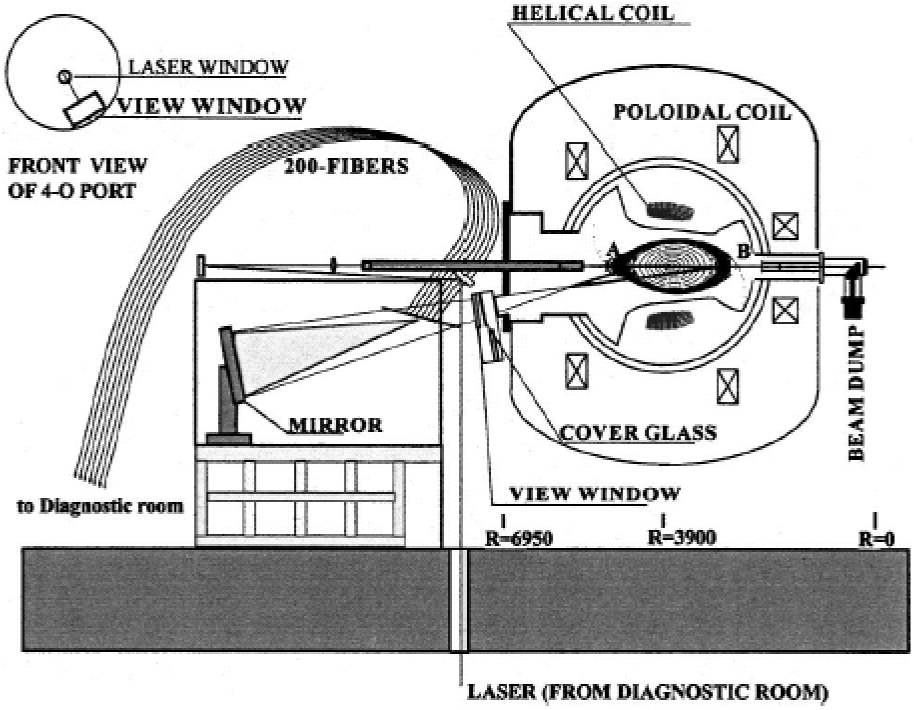

Fig. 2.2. Arrangement of Thomson scattering diagnostics for observation of horizontally elongated plasma cross-section in LHD.

References

[1] Z. L. Xiang and C. X. Yu, "High-temperature Plasma Diagnostic Technology", Shang Hai Sci. and Tech. Press, 1982.

[2] W. Finkelnburg and T. Peters, Handbüch der Physik, 1957. **28**: p. 79.

[3] W. J. Karzas and R. Latter, Astrophys. J. Suppl., 1961. **55**: p. 167.

[4] S. Morita and J. Baldzuhn, IPP-report III/199 (Max-Planck-Institut für Plasmaphysik, Garching , Germany, 1994).

[5] K. Narihara, I. Yamada, H. Hayashi et al., Rev. Sci. Instrum., 2001. **72**: p. 1122.

Chapter 3

Development of visible spectrometer system

3.1 Introduction

Effective ion charge, Z_{eff}, is a key parameter for evaluating the impurity content in fusion plasmas. When the Z_{eff} profile is measured in high-temperature plasmas, significant progress can be given for the impurity transport study in addition to the knowledge on the plasma collisionality and the plasma purity [1]. This information is entirely necessary for understanding the transport nature of magnetically confined toroidal plasmas. The Z_{eff} profile diagnostics based on the visible bremsstrahlung continuum measurement is planned in the Large Helical Device (LHD). Up to this day the visible bremsstrahlung continuum has been always measured through an interference filter [2-4] coupled with optical fibers and photomultipliers. However, line emissions [5] existing within the transmission wavelength band of the interference filter have always disturbed the exact diagnostics on visible bremsstrahlung continuum. In LHD, the presence of extremely strong line emissions resulted from low-temperature and high-density plasmas in the thick ergodic layer [6-7], which particularly characterizes the LHD edge plasmas, were a serious problem in the visible bremsstrahlung diagnostics [8]. In order to eliminate the line emission, therefore, an astigmatism-corrected Czerny-Turner-type visible spectrometer coupled with a charge-coupled device (CCD) has been designed in LHD to achieve a good spatial resolution and high throughput. The visible bremsstrahlung measurement was also measured through a micro-spectrometer [9] in W7-AS, whereas the system has no spatial resolution.

A standard Czerny-Turner-type spectrometer [10-11] is basically characterized by two spherical mirrors which can collimate the incident light against flat grating and transfer the image at the entrance slit to the exit slit. However, the astigmatism [12-14] still remains in such a simple spectrometer system due to different focus spots between meridional and sagittal planes. Focal images are thus deformed resulting in cross-talk between the fiber channels. To solve this problem, a computer-optimized toroidal mirror for correcting the astigmatism is added to the present visible spectrometer. Another requirement for the visible bremsstrahlung diagnostics is that the spectrometer should be bright to detect weak visible bremsstrahlung from low-density plasmas. Therefore, a compact Czerny-Turner-type spectrometer (Model: MK-300, Bunkoh-Keiki Co.LTD) is applied with a focal length of 300mm.

The diagnostic instrument was installed on a large rectangular glass window (220mm in horizontal size and 1300mm in vertical size) of LHD. The visible bremsstrahlung continuum is measured at a horizontally elongated cross section of the LHD elliptical plasmas through a 44-fiber parallel array. A full vertical bremsstrahlung emission profile is thus measured in the range of $-0.6\text{m} \le Z \le 0.6\text{m}$. As a result, the influence of the line emission was entirely removed from the bremsstrahlung continuum analysis. However, the vertical profile of the measured visible bremsstrahlung continuum was unfortunately still nonuniform. In this chapter, the visible bremsstrahlung profile diagnostics in LHD is presented with the study of the nonuniform visible bremsstrahlung emission profile, resulting from the low-temperature and high-density edge plasmas in the ergodic layer.

3.2 Visible spectrometer system

The parallel fiber array is installed on a rectangular glass window port of LHD with a small angle of 6° from the axis perpendicular to the toroidal magnetic filed in order to avoid nonuniform bremsstrahlung emission resulting from the inboard side of the torus, as illustrated in Fig. 3.1. Since the rectangular glass window has enough large vertical size (1300mm×220mm), the full vertical bremsstrahlung profile of LHD plasmas ($-0.6\text{m} \le Z \le$

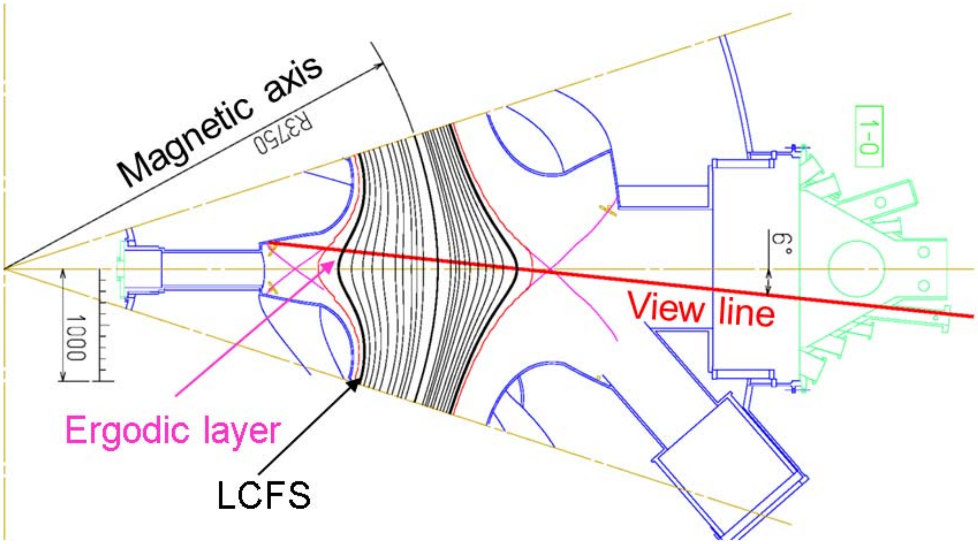

FIG. 3.1. Schematic top view of LHD (R_{ax}=3.75m) with view line of fiber array. View angle is tilted by 6° from port center axis perpendicular to toroidal magnetic field.

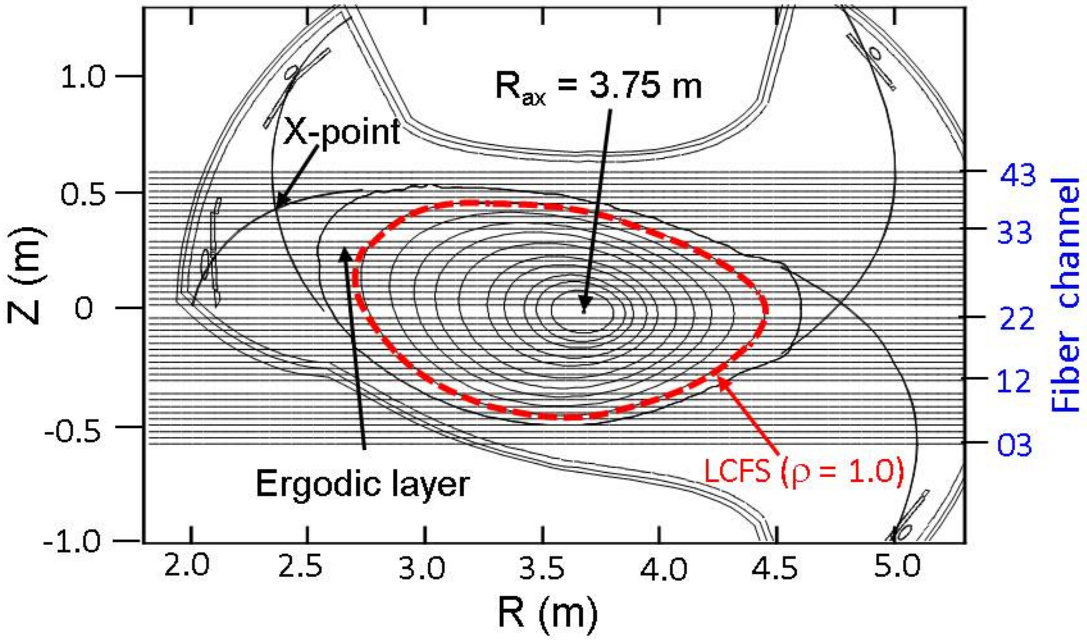

FIG. 3.2. Magnetic surfaces at horizontally elongated plasma cross section and parallel observation chords of fiber array. R and Z denote major radius and vertical distance from equator plane, respectively. Fiber channels mean sequential numbers of fibers.

0.6m) can be observed using parallel view chords, as shown in Fig. 3.2. The vertical fiber array consists of 44 parallel optical fibers with core and clad diameters of 100μm and 125μm, respectively. An optical lens with the focal length of 30mm set to each fiber defines spatial resolution of 30mm at the plasma center. It is seen in the figure that the ergodic layer near the inboard side x-point, at which the nonuniform bremsstrahlung continuum is strongly emitted, moves to upper side from the equator plane (Z=0) by tilting the observation chord at the small angle of 6°.

Figure 3.3 shows optical layout of the astigmatism-corrected Czerny-Turner-type visible spectrometer. The visible spectrometer consists of one removable entrance slit, four mirrors, three gratings and three masks. The short focal length of 300mm makes a high throughput optical system. The inner wall of the spectrometer is covered with carbon powder to reduce the visible light reflection. The optical mirrors and gratings are coated with aluminum and magnesium fluoride, respectively. The three masks are used for eliminating the unnecessary scattered light. The removable entrance slit can adjust the slit width in the range of 0-500μm through an external electric controller. The fiber array closely set to the entrance slit is arranged with interval of 128μm between each fiber. As a result, the spectral intensity and resolution can be optimized by choosing an appropriate slit width. The slit width of 60μm is used when a good spectral resolution is required and the slit width of 130μm is used when a high spectral intensity is required. Four mirrors consist of one toroidal mirror (M4), one flat mirror (M3) and two spherical mirrors (M1 and M2), as seen in Fig. 3.3. In particular, the curvature of the toroidal mirror is optimized by a computer simulation which calculates all the possible optical paths. Thus, the astigmatism, which is the main problem in the multi-channel fiber array measurement, can be entirely corrected for both the sagittal and meridional planes. The three gratings of 120, 300, 1200 grooves/mm have different blaze wavelengths of 330nm, 500nm, 200nm, respectively. All the gratings mounted in a rotatable turret can be also controlled by the electric controller. Among them, the 300 grooves/mm grating is usually used in the experiment to measure the wavelength interval of 450-600nm with the central wavelength of 530nm. In this case a wider wavelength range of 200nm to 900nm can be observed by changing the central wavelength.

The CCD (Andor SOLIS-DU934N) is adopted as a 2-dimensional detector for recording output images at the focal position. The size of CCD is 13.3mm × 13.3mm with 1024 pixels × 1024 pixels and the size of unit pixel is 13μm × 13μm. The CCD is usually cooled at the temperature of -20°C to reduce the thermal noise and operated in full-image and multi-track modes. The full-image mode is used to check the spectral and spatial resolutions by accumulating enough counts with long exposure time. The multi-track mode is set for the routine experiment making vertical 12 pixels into one through the binning to improve signal-to-noise ratio and time resolution. The CCD is then usually operated at the exposure time of 31ms and the time resolution of 100ms with vertical readout speed of 11 μs/line and horizontal readout time of 0.4 μs/pixel. A little higher time resolution of 80ms is alternatively used with the exposure time of 12ms according to the discharge waveform. The exposure time can be precisely defined by use of a mechanical shutter mounted in front of the CCD the motion of which is synchronized with the CCD operation.

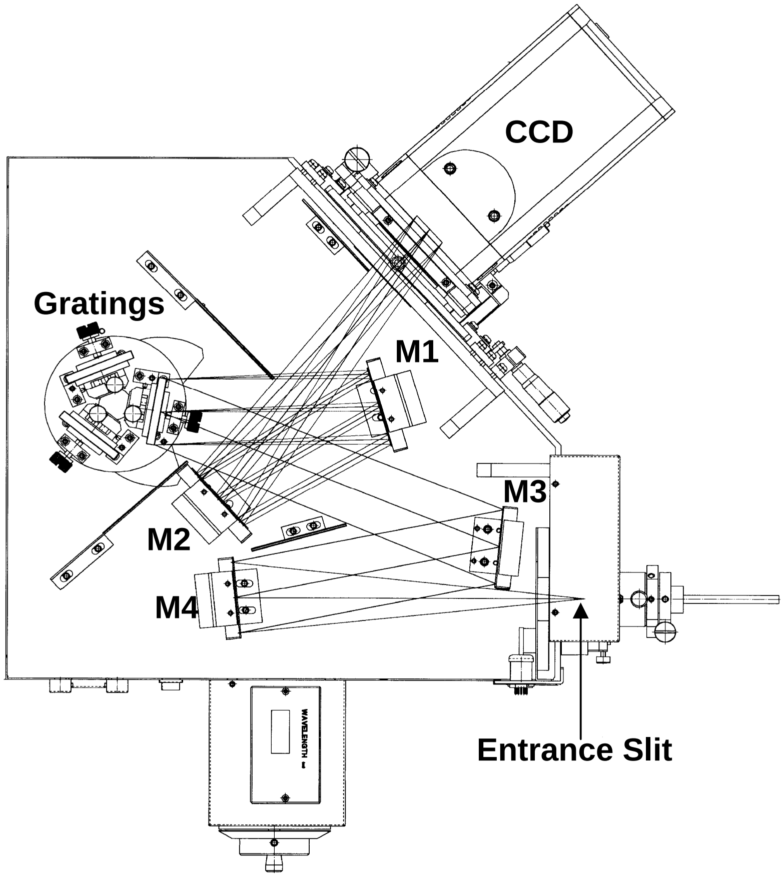

FIG. 3.3. Optical layout of 300mm astigmatism-corrected Czerny-Turner-type visible spectrometer (M1: spherical mirror, M2: spherical mirror, M3: flat mirror, M4: toroidal mirror).

3.3 System calibration

The spectral resolution of the visible spectrometer is checked by the line emission at wavelength of 546nm from a standard mercury lamp. Figure 3.4 shows the spectral resolution for three different gratings as a function of the entrance slit width. The spectral width, Δλ, is defined as the full width at half maximum (FWHM) of the line spectrum. The slit width of 60μm improves the spectral resolution to about 35% compared to the case of the 130μm slit width. The spectral resolution seems to improve linearly with the groove density. The 1200 grooves/mm grating is used to check the presence of line emissions within the wavelength interval to be measured.

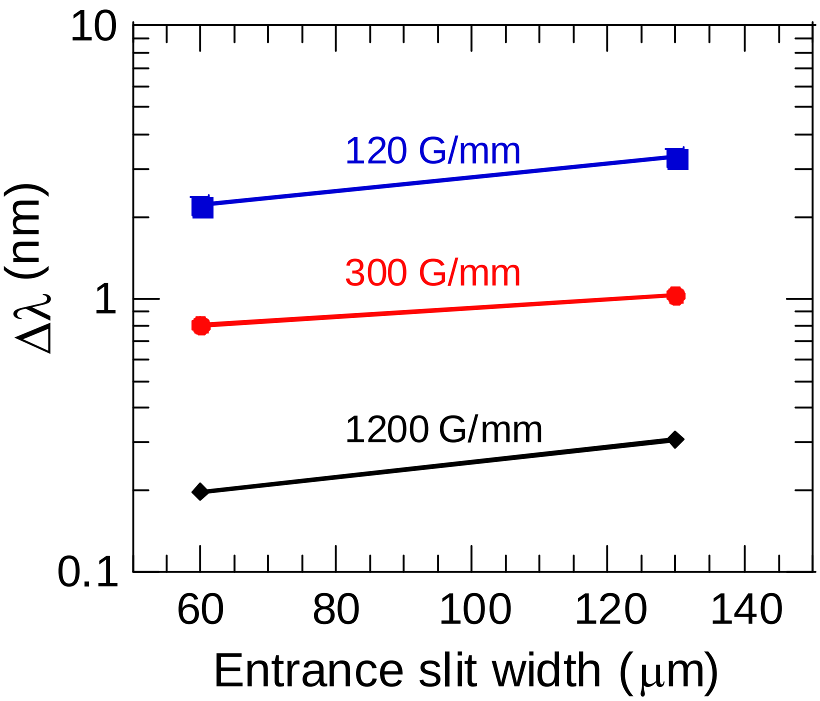

FIG. 3.4. Spectral resolution, Δλ, at FWHM for three gratings as a function of entrance slit width. Solid squares, solid circles and solid diamonds indicate 120 grooves/mm, 300 grooves/mm and 1200 grooves/mm gratings, respectively.

Absolute sensitivity calibration of the present diagnostic system is performed with an integrating sphere using the same optical system as the actual measurement. The efficiency of the three gratings for different entrance slit widths is absolutely calibrated in the wavelength range of 450-600nm (510-550nm for 1200 grooves/mm grating), as plotted in Fig. 3.5. The variable, $d_{s,}$ denotes the width of the entrance slit. The 300 grooves/mm grating shows the best sensitivity resulting from the large effective ruled area and the optimum braze wavelength. The sensitivity of 1200 grooves/mm grating is less in two orders compared to other two gratings. The 300 grooves/mm grating is therefore favorable to the present purpose as well as the 120 grooves/mm grating, since the bremsstrahlung emission is very weak in low-density discharges. The entrance slit width of d_s = 130μm is also better for the present measurement, because the sensitivity of the optical system is increased by 50% compared with that of d_s = 60μm.

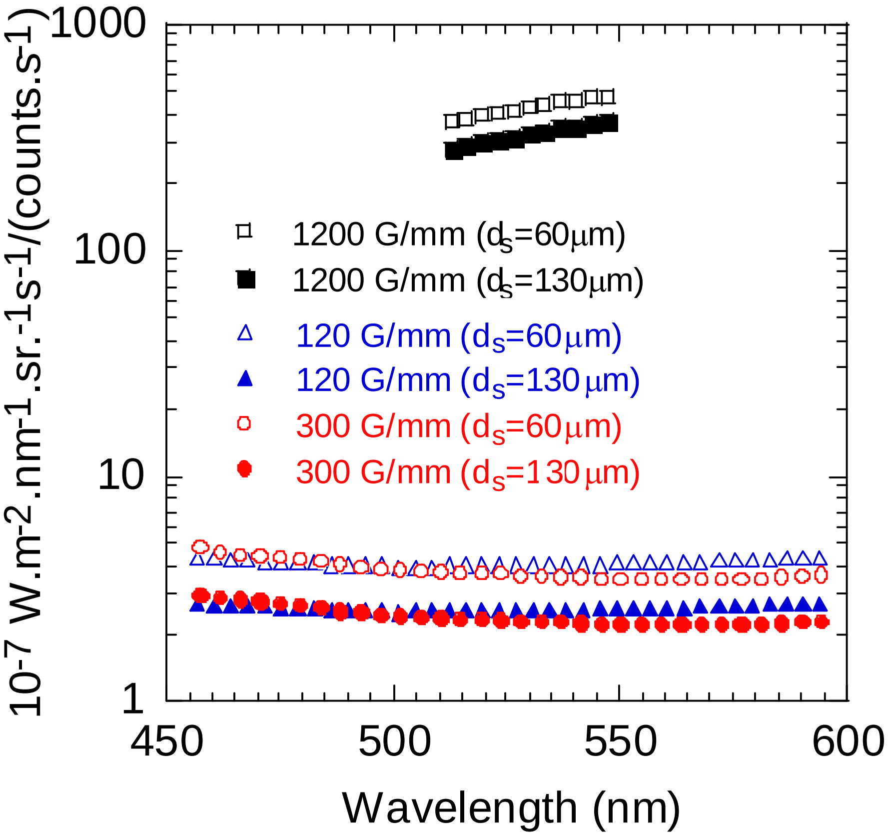

FIG. 3.5. Absolute sensitivities of three gratings with different grooves for two entrance widths, d_s, in wavelength range of 450-600nm.

The relative sensitivity among fiber channels is examined with the integrating sphere. Figure 3.6 shows the result for the 120 grooves/mm and 300 grooves/mm gratings. The data measured at the central wavelength of 530nm are normalized by the intensity at the central chord of #22. The sensitivity profile for the 300 grooves/mm grating is relatively flat indicating the sensitivity difference within 10% to the central chord intensity, whereas the 120 grooves/mm grating has a scattered sensitivity profile. As a result, we conclude that the 300 grooves/mm grating is the best choice for the present study.

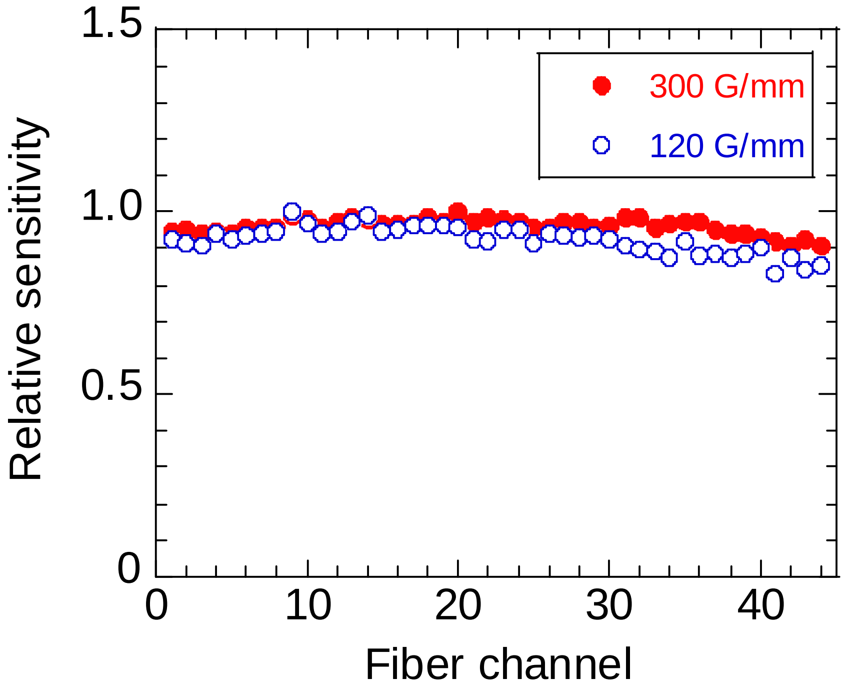

FIG. 3.6. Relative sensitivities of two gratings for fiber channels from 1 to 44. Sensitivity is normalized to central channel.

3.4 Experimental results

3.4.1 Images and spectra

The output images are recorded by the CCD operated in the full-image mode. The 300 grooves/mm grating is used at the central wavelength of 480nm. The entrance slit is fully opened to check the fiber image. The results shown in Fig. 3.7 trace all the fiber images of H_{β} 486.13nm, CIII 465.15nm and OII 459.59nm. The image of each fiber chord is clearly isolated indicating negligible crosstalk between adjacent channels, which leads to an excellent spatial resolution in the present diagnostic system. It is also examined that the well-defined good images are not entirely deformed when the wavelength is changed. The good focal image is resulted from the corrected astigmatism, in particular, by use of the toroidal mirror. Since the size of the images and the interval between the images are constant, a fixed vertical binning value can be used for the multi-track mode in the CCD operation.

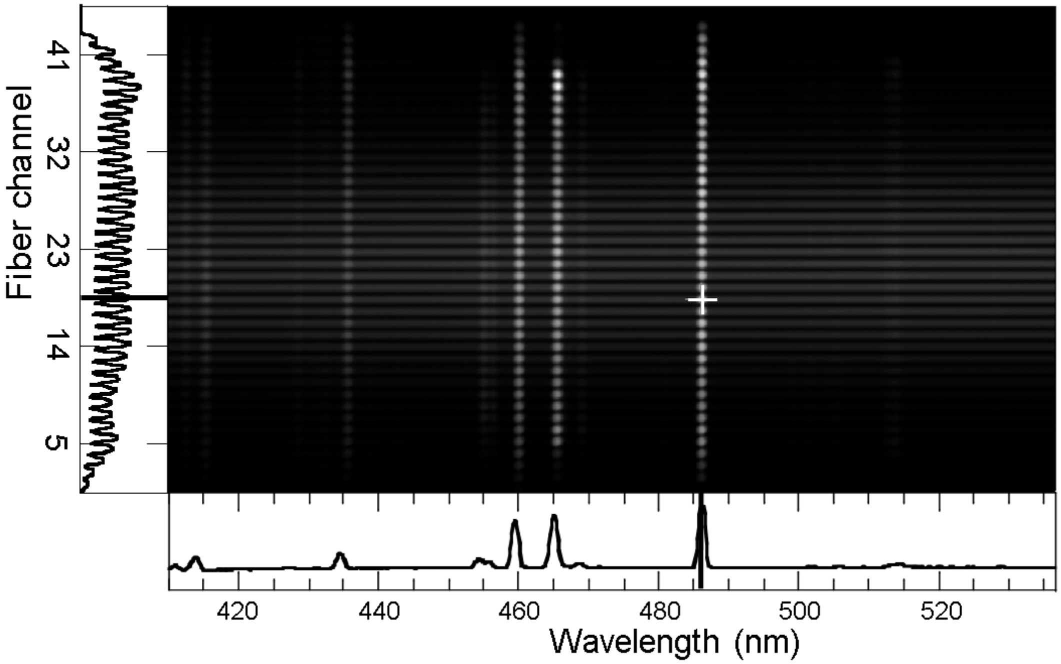

FIG. 3.7. Output CCD images against wavelength and fiber channel with 300 grooves/mm grating at central wavelength of 480nm. Images of Hβ 486.13nm, CIII 465.15nm and OII 459.59nm are clearly visible.

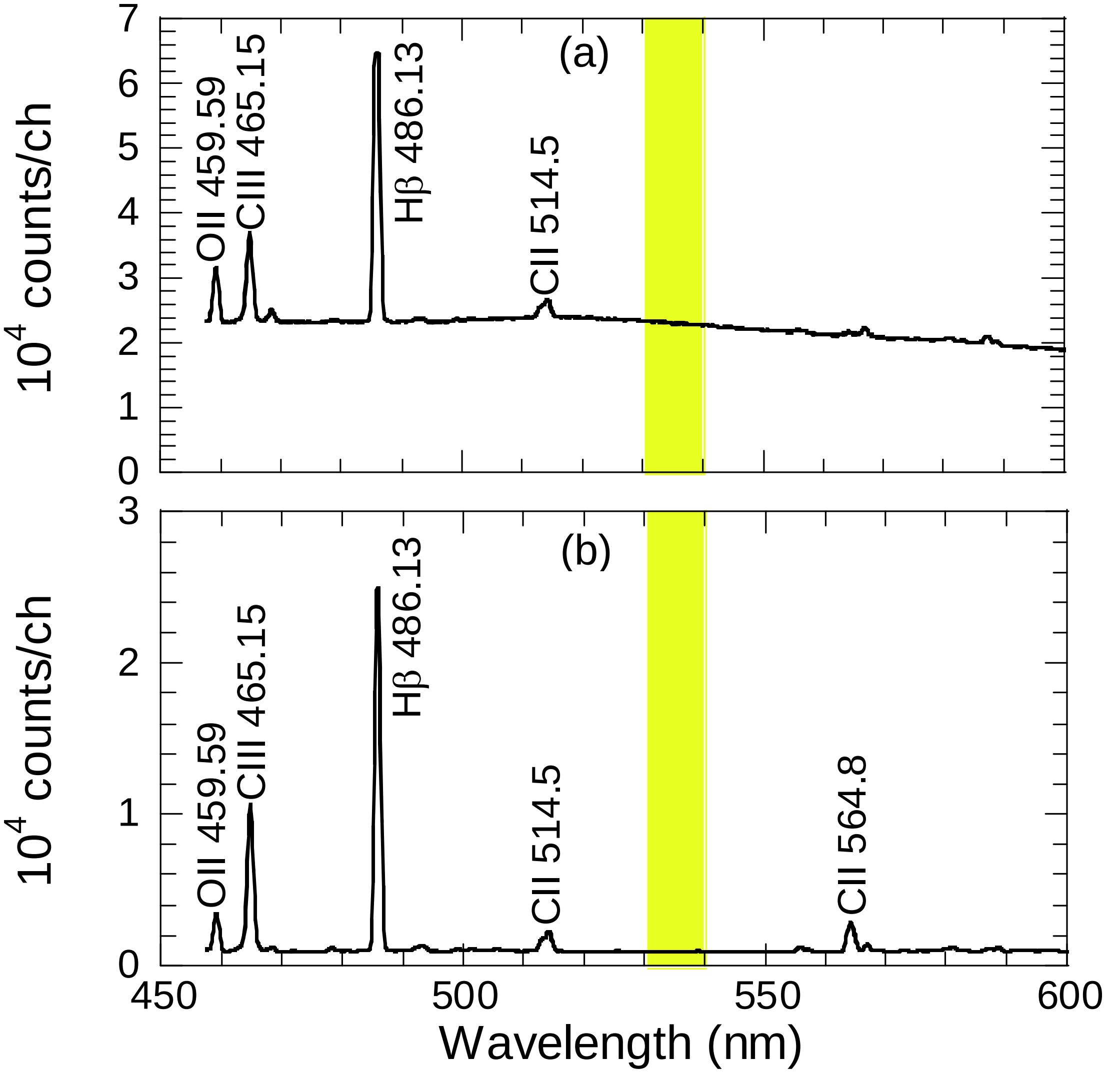

FIG. 3.8. Typical visible spectra in wavelength range of 450-600 nm at Z = 26mm for (a) $n_e = 2.9 \times 10^{14}\mathrm{cm}^{-3}$ and (b) $n_e = 2.0 \times 10^{13}\mathrm{cm}^{-3}$. Hatched areas indicate spectral region (530-540nm) for bremsstrahlung continuum measurement.

The visible spectra are measured with the 300 grooves/mm grating at the central wavelength of 530nm. Figure 3.8(a) shows a typical visible spectrum measured at high-density discharge with $n_e = 2.9 \times 10^{14}\text{cm}^{-3}$. The spectral interval of 530-540nm used for the bremsstrahlung profile measurement is indicated with the hatched area. The absence of line emissions in this region is always confirmed using the 1200 grooves/mm grating. The bremsstrahlung continuum intensity is quite strong in such high-density discharges, e.g., 2.3×10^4 counts/ch, where the well-known line emission such as H_β 486.13nm easily saturates at 65,536counts in the present 16bit CCD detector. The bremsstrahlung intensity is, on the other hand, very weak at low density discharge with $n_e = 2.0 \times 10^{13}\text{ cm}^{-3}$, as seen in Fig. 3.8(b), e.g., 0.1×10^4 counts/ch. We have to say, however, the counts for the bremsstrahlung continuum are still enough for the analysis. These results demonstrate high performance of the present diagnostic system.

3.4.2 Bremsstrahlung intensity profile

A typical profile of the chord-integrated bremsstrahlung emission is measured at standard magnetic configurations of R_{ax} = 3.60m and R_{ax} = 3.75m in LHD, as shown in Figs. 3.9 (a) and (b), respectively. Nonuniform bremsstrahlung emission peak is clearly seen in the upper half profile ($0 \le Z \le 0.6$m). Here, we define the values of I_{core}, $I_{asy}(U)$ and $I_{asy}(L)$ as the chord integrated bremsstrahlung intensity at center (Z = 0) and the maximum intensities at upper half and lower half ($-0.6 \le Z \le 0$m), respectively. In the upper half profiles the peak position is found at Z = 0.32m. Hatched areas in the two figures denote the lower half region. In the case of R_{ax} = 3.60m, however, the lower half profile is monotonic, whereas in case of the R_{ax} = 3.75m, an nonuniform emission peak is also appeared at Z = -0.18m. For understanding the reason, the magnetic surface structures are plotted in Figs. 3.9 (c) and (d) with structures of the ergodic layer, which is characterized by the presence of thick stochastic magnetic field layer surrounding the last closed flux surface (LCFS). The thick ergodic layer is located in particular at the regions near X-points in the inboard and outboard sides of the torus, where the magnetic flux density is very high. Then, the nonuniform bremsstrahlung profile appeared in the upper half indicates the presence of low-temperature and high-density plasma at the region around the inboard or outboard side X-point. The magnetic configuration dependence of the nonuniform bremsstrahlung profile is further checked as a function of the plasma axis position. The maximum intensity relative to the central chord intensity, 'nonuniform factor', F_{asy}, defined as the ratio of $I_{asy}(U)/ I_{core}$ or $I_{asy}(L) /I_{core}$, is here introduced. It characterizes the intensity increase in the chords lying further away from the central chord. Figure 3.9(e) displays the

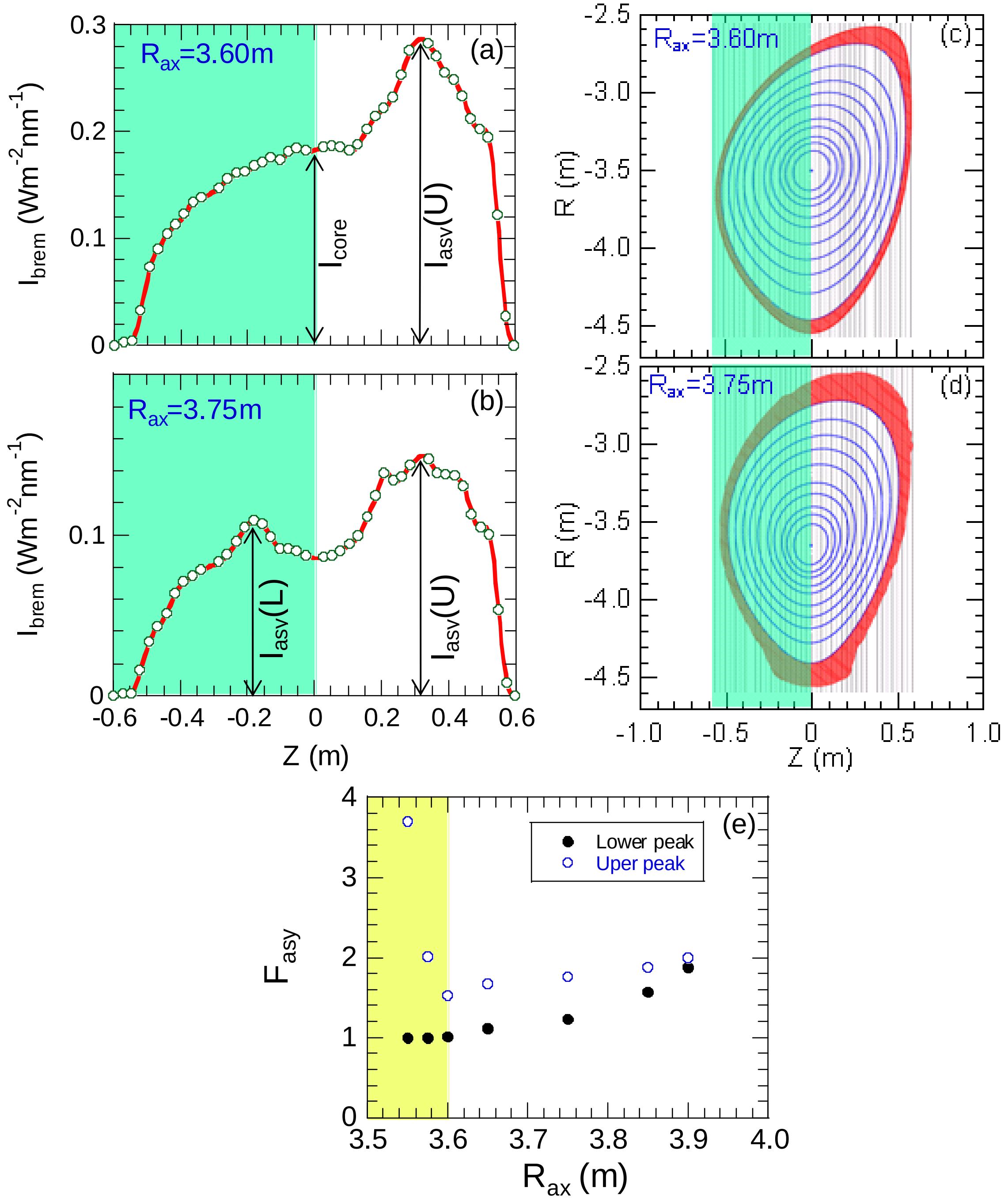

FIG. 3.9. Vertical profiles of chord-integrated bremsstrahlung intensity in magnetic configurations of (a) R_{ax} = 3.6m and (b) R_{ax} = 3.75m, magnetic surface structures with observation chords for (c) R_{ax} = 3.6m and (d) R_{ax} = 3.75m, and (e) nonuniform factor, F_{asy}, of chord-integrated bremsstrahlung intensity profile as a function of magnetic axis position, R_{ax}. Hatched areas in (a), (b), (c) and (d) indicate lower half of observation chords. Hatched area in (e) indicates nonexistence of asymmetric bremsstrahlung in lower half of plasmas.

result. The nonuniform factors for the lower half profile are nearly constant in $R_{ax} \leq 3.6$m, whereas those gradually increase with R_{ax} in $R_{ax} \geq 3.65$m. In the upper half profile the intensity increase in the chords lying further away from the central chord is clearly visible in all the magnetic configurations. The hatched area indicates the fiber array which can be free of the bremsstrahlung intensity increase. Thus, we find that the analysis of the bremsstrahlung profile is possible only for the inwardly shifted magnetic configurations ($R_{ax} \leq 3.6$m) in general discharges with high temperature.

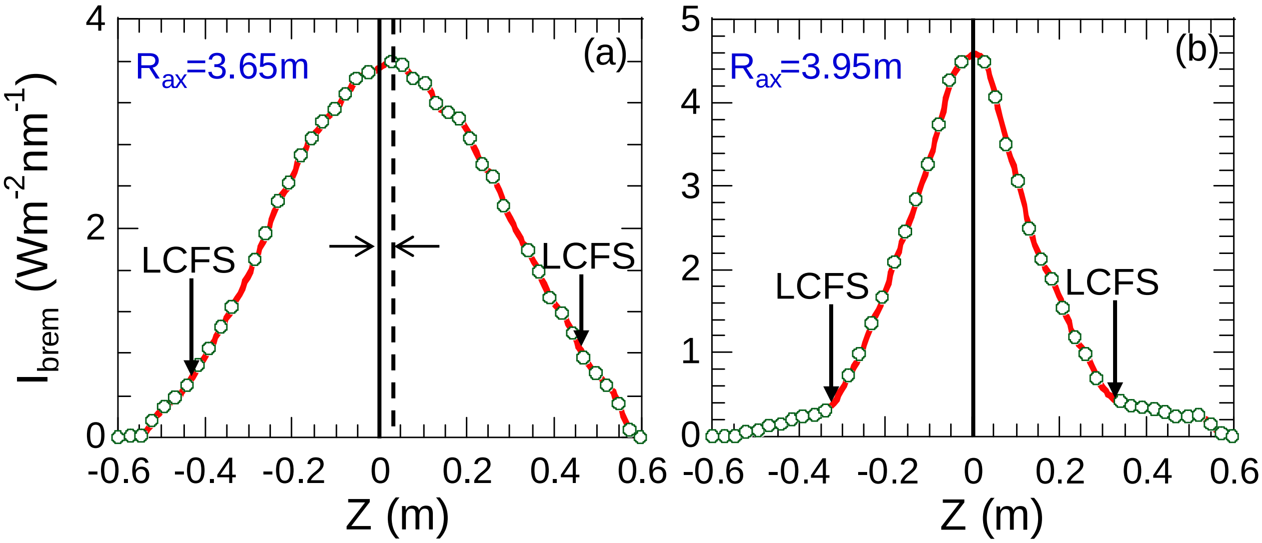

FIG. 3.10. Vertical profiles of chord-integrated bremsstrahlung intensity in high-density plasmas with (a) R_{ax} = 3.65m and (b) R_{ax} = 3.95m. Vertical solid and dashed lines mean plasma center and intensity maximum, respectively. Radial positions of last closed flux surface (LCFS) are also indicated with vertical arrows.

A peaked profile of the chord-integrated bremsstrahlung emission is produced in extremely high-density discharges with H_2 multi-pellet injection. The nonuniform bremsstrahlung emission observed in the general discharges can be entirely eliminated in such discharges due to the temperature decrease followed by the reduction of the plasma radius. Figures 3.10 (a) and (b) show typical peaked profiles of the bremsstrahlung emission in the high-density discharges for the magnetic configurations of R_{ax} = 3.65m and

R_{ax} = 3.95m. Since the plasma radius defined by the LCFS decreases as the magnetic axis is outwardly shifted, the emission profile becomes remarkably peaked as indicated for the case of R_{ax} = 3.95m. The shift of the peak position from the central axis at Z = 0 seen in Fig. 3.10 (a) is originated in the chord length difference (also see Fig. 3.2). Here, we conclude that the Z_{eff} measurement is possible even in outwardly shifted configurations (R_{ax} > 3.6m) since the nonuniform bremsstrahlung emission is disappeared in high-density operation.

3.5 Comparison with old system

The bremsstrahlung intensity profiles are compared between the visible spectrometer system and the old interference filter system in different density regimes, as shown in Fig. 3.11. In the high density regime ($n_e = 16\times10^{13}cm^{-3}$), similar peaked profiles are observed in the bremsstrahlung intensity profile for both systems (see Figs. 3.11 (a) and (d)). It indicates that the two diagnostic systems are well working as a monitor of the visible bremsstrahlung signal because the plasma edge boundary in the ergodic layer tends to shrink in such high-density discharges and the effect of line emissions is relatively small compared to the bremsstrahlung. In the middle density regime ($n_e = 6.4\times10^{13}cm^{-3}$), lower half of the bremsstrahlung profile in the visible spectrometer system represents the accurate profile, whereas upper half of the profile is clearly deformed by nonuniform bremsstrahlung emission (see Fig. 3.11 (b)). However, the bremsstrahlung profile in the old system is deformed in all the radial positions, as illustrated in Fig. 3.11 (e). In the low density regime of $n_e = 2.6 \times10^{13}cm^{-3}$, lower half of the bremsstrahlung profile in the visible spectrometer system seems to be good, while the old system expresses the entirely worse profile. The poloidally nonuniform line emissions originated in the edge boundary in the ergodic layer is possibly the reason why the strange profile is seen in the old system, in addition to the nonuniform bremsstrahlung emission.

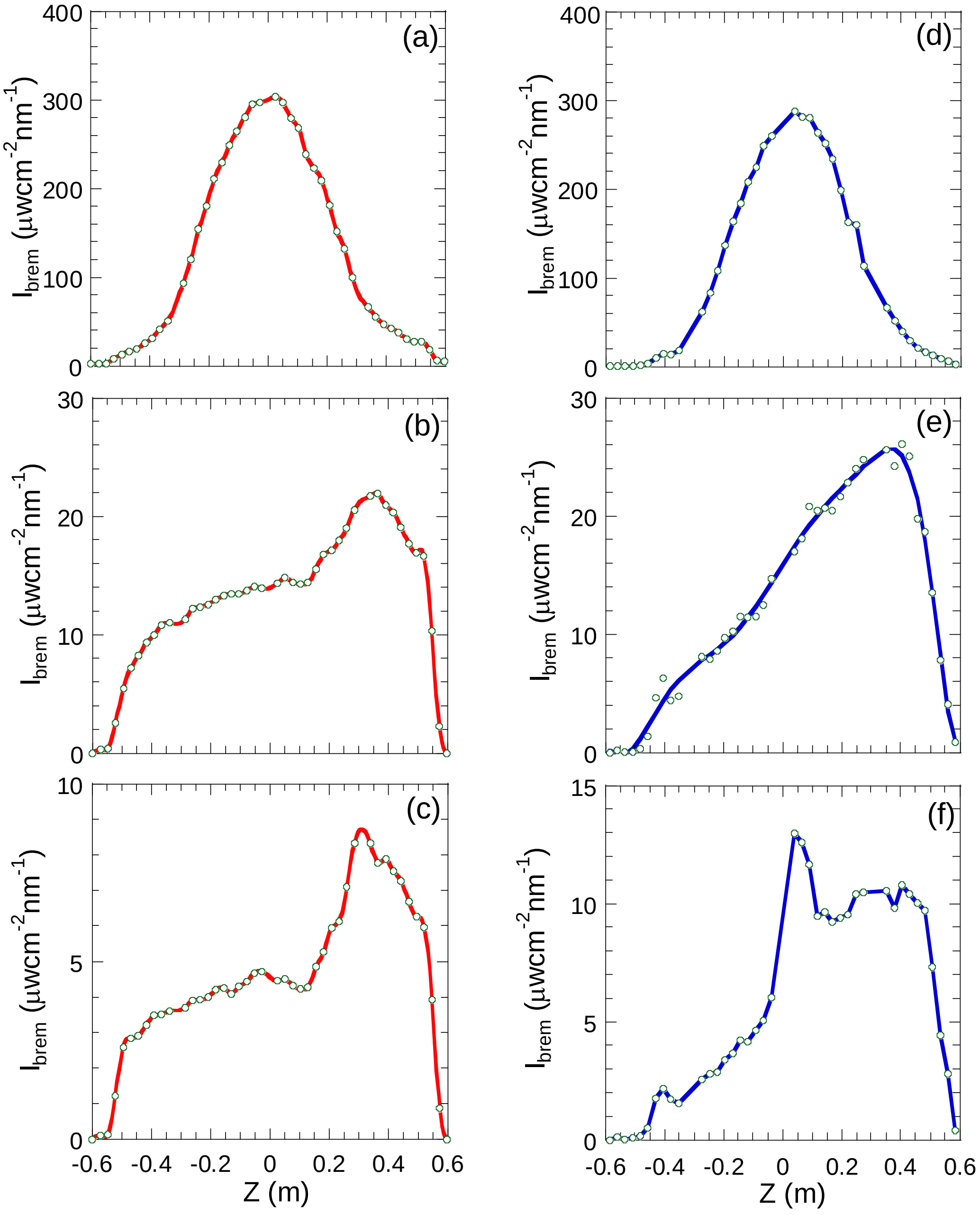

FIG. 3.11. Comparison of bremsstrahlung intensity profiles at R_{ax} = 3.6m measured by visible spectrometer system in (a) high density ($n_e = 16\times10^{13}\text{cm}^{-3}$), (b) middle density ($n_e = 6.4\times10^{13}\text{cm}^{-3}$) and (c) low density ($n_e = 2.6 \times10^{13}\text{cm}^{-3}$) ranges and by old interference filter system in (d) high density, (e) middle density and (f) low density ranges.

3.6 Summary

The astigmatism-corrected Czerny-Turner-type visible spectrometer has been installed in LHD to measure the bremsstrahlung continuum without contribution of the line emission. The high throughput optical system is achieved by adopting a compact spectrometer with the short focal length of 300mm. The good spectral and spatial resolutions are simultaneously obtained by correcting the astigmatisms through the introduction of a computer-optimized toroidal mirror. The scattered light is entirely eliminated by the masks carefully placed in the spectrometer. The visible spectrometer system is absolutely calibrated by an integrating sphere.

The lower half of the full vertical bremsstrahlung profile can be free of the nonuniform bremsstrahlung emission for inwardly shifted magnetic configurations ($R_{ax} \leq 3.6$m) by tilting the horizontal angle by 6° from the direction perpendicular to the toroidal magnetic field. The symmetric bremsstrahlung emission profile is measured in the extremely high-density discharge for all the configurations because of the low edge temperature followed by the shrinkage of the edge boundary.

References

[1] S. P. Hirshman and D.J. Sigmar, Nucl. Fusion, 1981. **21**: p. 1079.

[2] B. Schunke, G. T. A. Huysmans and P.R. Thomas, Rev. Sci. Instrum., 2005. **76**: p. 083501.

[3] G. Verdoolaege, G. Telesca, E. Delabie et al., Rev. Sci. Instrum., 2006. **77**: p. 10F310.

[4] F. Orsitto, M. R. Belforte, M.Borra et al., Rev Sci Instrum, 1997. **68**: p. 1024.

[5] H. Nozato, S. Morita and M. Goto, J. Plasma Fusion Res. SERIES, 2006. **7**: p. 14.

[6] S. Masuzaki, T. Morisaki, N. Ohyabu et al., Nucl. Fusion, 2002. **42**: p. 750.

[7] M. B. Chowdhuri, S. Morita, M. Kobayashi et al., Phys. Plasmas, 2009. **16**: p. 062502.

[8] H. Nozato, S. Morita and M. Goto, J. Plasma Fusion Res. SERIES, 2002. **5**: p. 442.

[9] M. Krychowiak, R. König, T. Klinger and R. Fischer, J. Appl. Phys., 2004. **96**: p. 4784.

[10] U. Litzen, Physica Scripta., 1970. **2**: p. 84.

[11] B. Bates, M. Mcdowell, and A.C. Newton, J. Phys. E, 1969. **3**: p. 206.

[12] R. C. Preston, J. Phys. E, 1970. **3**: p. 737.

[13] N. C. Das, Appl. Opt., 1991. **30**: p. 3589.

[14] M. Goto and S. Morita, Rev. Sci. Instrum., 2006. **77**: p. 10F124.

Chapter 4

Reconstruction of bremsstrahlung profile

4.1 Introduction

Abel inversion method is required to covert the chord-integrated bremsstrahlung intensity profile to the radial bremsstrahlung emissivity profile. For the axisymmetric plasmas, the basic method of Abel inversion is given by solving the integration equation. However, the differential approach and the singularity formation in the usual Abel inversion technique make the uncertainty in the calculation extremely large. Many numerical methods are therefore employed by Cormack [1], Bockasten [2] and Barr [3] to fit the chord-integrated signals with a numerical function, whereas those have disadvantages that a large number of chord data and a long computational time are required. The slice and stack method [4] based on the geometrical data is also developed assuming that the local signal emissivity is equal in the same geometrical surface. Since the nonaxisymmetric three-dimensional magnetic structure in LHD is easily deformed by Shafranov shift and the toroidal plasma current, such methods cannot be simply applied to the LHD plasma. Thus, the slice and stack method [5-6] based on the magnetic surface data instead of the geometrical data is adopted for the Abel inversion to obtain the radial bremsstrahlung emissivity profile in LHD. The magnetic surface structure is calculated by variation moments equilibrium code [7] (VMEC) usable in three-dimensional space.

Error estimation is important for checking the reliability of Abel inversion technique. In JET, the random noise is added to check the robustness in the inversion process [8]. In TFTR, the error propagation is examined in the calculation [9-10]. In LHD, the radial bremsstrahlung emissivity profile after the Abel inversion is usually hollow because the density profile is flat. A large error is easily appeared in the central region of the emissivity profile because the signal-to-noise ratio is quite small. The uncertainty based on the magnetic surface deformation has to be also examined, in particular, for the chord length.

4.2 Principle of Abel inversion technique

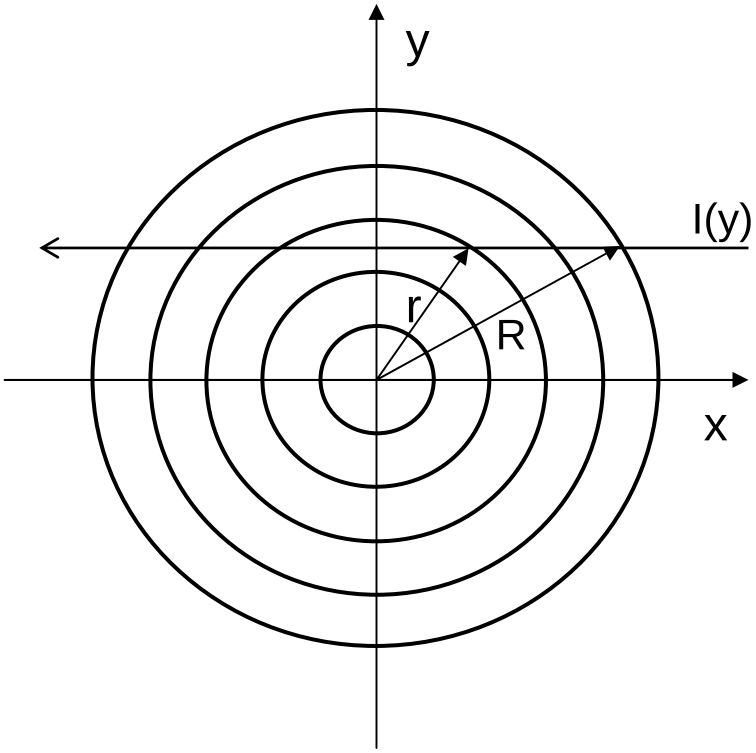

FIG. 4.1. Circular cross section and coordinate for Abel inversion

Abel inversion is used to obtain the local signal from the chord-integrated signal. It is formularized by Abel and Jacobi in 1827. Here, the principle of the Abel inversion method is introduced for circular cross-section, as seen in Fig. 4.1. The circular cross section is defined by;

$$x^2 + y^2 = r^2 \quad (0 \le r \le R). \tag{4.1}$$

The signal along the horizontal view chord, I(y), can be expressed by the local signal, ε(r), as follows;

$$I(y) = \int \varepsilon(r)dx = 2\int_y^R \frac{\varepsilon(r)r}{(r^2 - y^2)^{1/2}}dr. \tag{4.2}$$

The solution of Eq. (4.2) for the circular cross section is then given by

$$\varepsilon(r) = -\frac{1}{\pi}\int_r^R \frac{\frac{d}{dr}I(y)}{(y^2 - r^2)^{1/2}}dy. \tag{4.3}$$

4.3 Slice and stack method based on magnetic geometry

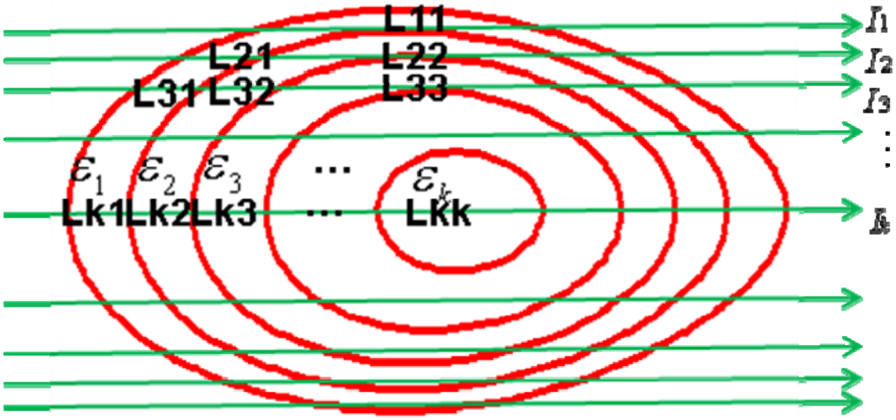

FIG. 4.2. Nonaxisymmetric cross section for slice and stack method based on magnetic surfaces.

The Abel inversion method is commonly adopted to convert the chord-integrated signal to the local emissivity signal for an axisymmetric configuration [11-12], i.e., circular and elliptical configurations. For a nonaxisymmetric configuration (see Fig. 4.2), in particular, LHD plasmas, however, the usually used Abel inversion method is not well applicable. The slice and stack method with finite β-effect is therefore used in the present analysis based on the assumption that the bremsstrahlung emissivity is constant at the same magnetic surface. The plasma geometry for the present analysis is calculated with the three-dimensional equilibrium code (VMEC). The bremsstrahlung emissivity after Abel inversion is expressed as follows;

$$\varepsilon = L^{-1} I \quad \text{or} \quad \begin{pmatrix} \varepsilon_1 \\ \varepsilon_2 \\ \varepsilon_3 \\ \vdots \\ \varepsilon_k \end{pmatrix} = \begin{pmatrix} L_{11} & 0 & 0 & \cdots & 0 \\ L_{21} & L_{22} & 0 & \cdots & 0 \\ L_{31} & L_{32} & L_{33} & \cdots & 0 \\ \vdots & \vdots & \vdots & \cdots & \vdots \\ L_{k1} & L_{k2} & L_{k3} & \cdots & L_{kk} \end{pmatrix}^{-1} \begin{pmatrix} I_1 \\ I_2 \\ I_3 \\ \vdots \\ I_k \end{pmatrix}, \tag{4.4}$$

where ε, L and I mean the bremsstrahlung emissivity profile, the matrix of the chord length and the bremsstrahlung intensity profile, respectively.

4.3.1 Determination of magnetic geometry

As the first step of the analysis an appropriate magnetic surface structure is determined so that the electron temperature profile can be symmetric against a derived normalized radius. A set of magnetic configurations is calculated according to discrete numbers of volume-averaged β values with assumed three pressure profiles. Figure 4.3 shows the assumed pressure profiles for calculating the magnetic surface structure as a function of the normalized radius. The broad pressure profile of $P_0(1-\rho^8)(1-\rho^2)$ indicates the usual pressure profile appeared in LHD plasmas.

The temperature profile measured by Thomson diagnostic basically covers the whole plasma range at the equatorial plane in the horizontally elongated plasma cross section. The temperature profile measured as a function of the major radius is converted into a function of the normalized radius, based on a set of magnetic surface structures. The symmetric temperature profile as a function of the normalized radius is obtained by adjusting the β values and the pressure profiles. As a result, the corresponding appropriate magnetic configuration can be finally selected. A typical example of this procedure is illustrated in Fig. 4.4. Two magnetic surface structures with β = 0% and β = 0.55% are displayed in Figs. 4.4 (a) and (b), respectively. The value of ΔR shows the Shafranov shift for the β = 0.55% case. The temperature profile plotted as a function of the normalized radius is carefully examined on its symmetric property, as shown in Fig. 4.4 (c). In this case, β = 0.55% is selected as the β value giving the best symmetric T_e profile.

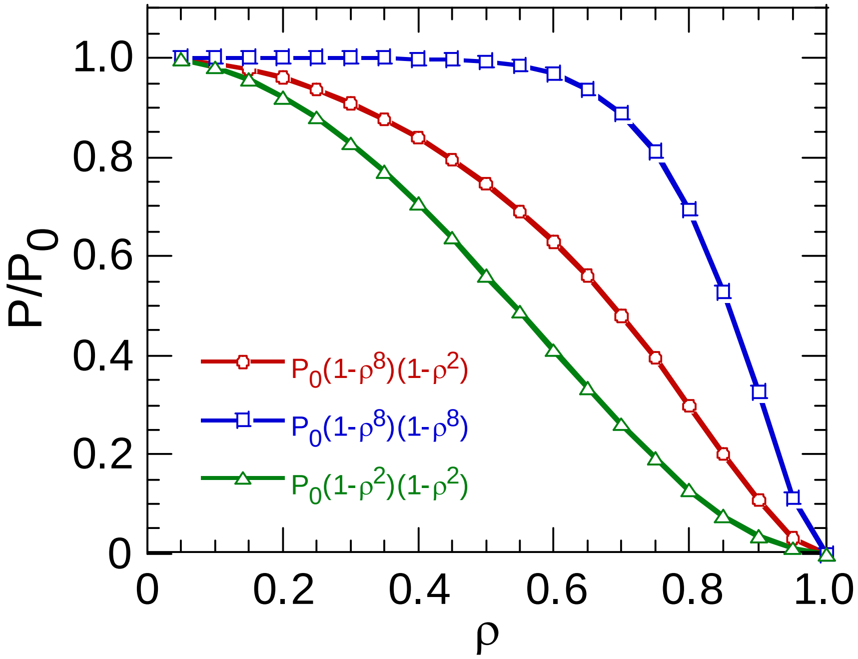

FIG. 4.3. Pressure profiles for deriving magnetic surface structures against normalized radius.

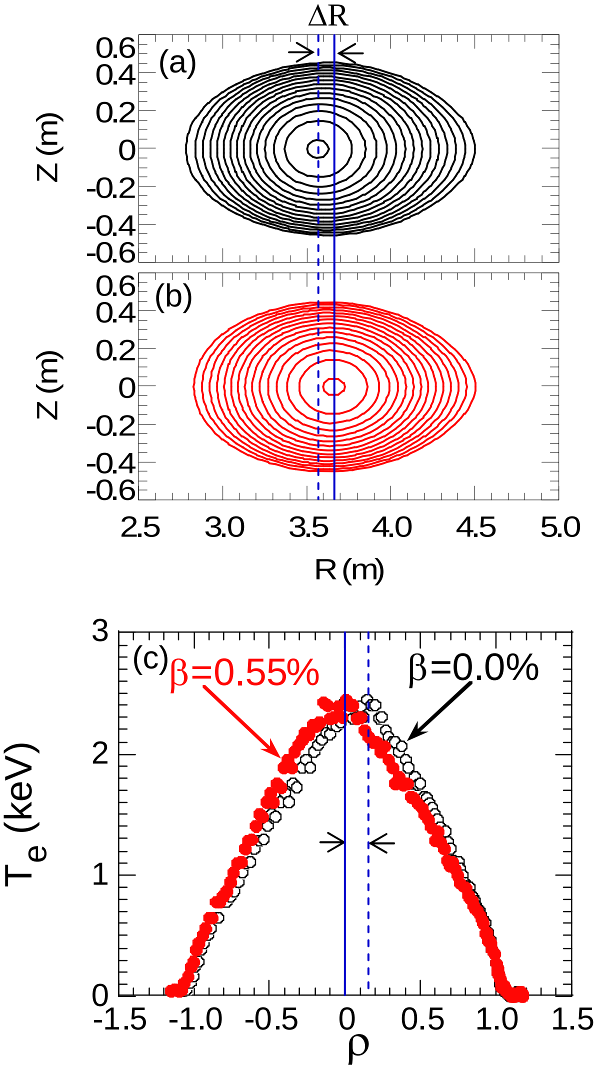

FIG. 4.4. Magnetic surface structures in (a) β = 0.0% and (b) β = 0.55% and (c) electron temperature profiles for β = 0.0% (open circles) and β = 0.55% (solid circles) as a function of normalized radius. Value of ΔR means Shafranov shift.

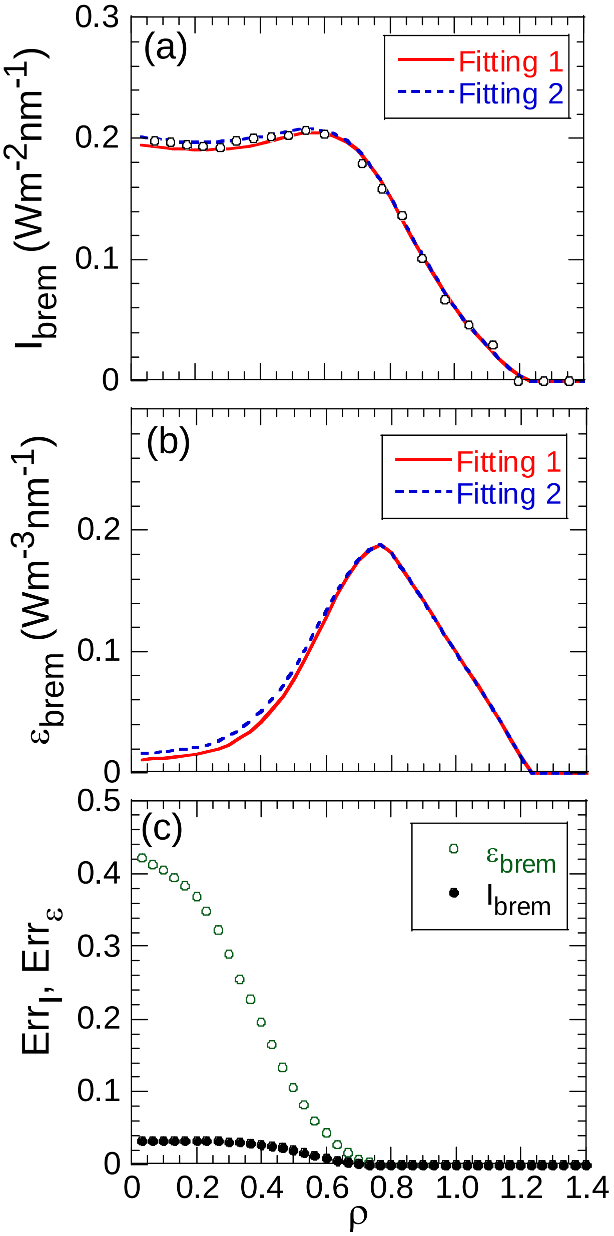

FIG. 4.5. (a) Chord-integrated bremsstrahlung intensity, (b) bremsstrahlung emissivity after Abel inversion for two different fitting curves, (c) normalized errors of intensity (solid circles), $Err_I=(I_{fit1}-I_{fit2})/I_{fit1}$, and emissivity (open circles), $Err_\varepsilon=(\varepsilon_{fit1}-\varepsilon_{fit2})/\varepsilon_{fit1}$, between two fitting profiles.

4.3.2 Nonlinear fitting method for integrated bremsstrahlung profile

For the extremely hollow profile case, the emissivity profile is easily affected by the small difference in the chord-integrated intensity profile. An iterative method is adopted to fit the bremsstrahlung intensity profile. At first, a certain emissivity profile is assumed and then the bremsstrahlung intensity profile is calculated with the matrix of chord length. The exact emissivity profile is determined by minimizing the χ^2 test between the calculated and experimental bremsstrahlung intensity profile through the iterative procedure. The example of the result is shown in Fig. 4.5. A little different two fitting curves are traced in the figure. The small difference in the intensity profile fitting is transferred into the emissivity profile. The emissivity error between the two fitting curves, $Err_\varepsilon=(\varepsilon_{fit1}-\varepsilon_{fit2})/\varepsilon_{fit1}$, is very large, i.e., 40% at the plasma center, whereas the intensity error, $Err_I=(I_{fit1}-I_{fit2})/I_{fit1}$, is only 3% at the plasma center.

4.4 Error estimation in Abel inversion calculation

The uncertainty in the Z_{eff} profile analysis is basically resulted from the uncertainty of the used magnetic surface structure. In practice, however, the determination of an exact magnetic surface structure completely consistent with the experimental result is really difficult in the analysis. Hence, it is critical to examine the influence of the uncertainty based on the magnetic surface structure. For the purpose the high-density discharge with high-β and the moderate-density discharge with low-β are used for the examination.

Figures 4.6 (a), (b) and (c) display the bremsstrahlung intensity profile, the integrated-chord length profile and the bremsstrahlung emissivity profile in the outwardly shifted magnetic configuration of R_{ax} = 3.85m. The data are taken at extremely high density with central electron density of $n_e(0) = 7.0\times10^{14}cm^{-3}$ after H_2 multi-pellet injection. The pressure profile of β = 1.44% (8020) is used for the analysis, where 1.44% is the β value and "8020" means the type of assumed pressure profile (see Fig. 4.3). The emission profile is entirely peaked in the discharge. The integrated-chord length is calculated with the observation chord within $\rho = \pm1.5$ (see Fig. 3.2). Here, the magnetic surfaces at $\rho > 1.0$ are assumed to be the extension of the magnetic surface contour at LCFS (ρ = 1.0) considering the linear extrapolation in the plasma volume between the adjacent magnetic surfaces. In this extremely peaked profile case the emissivity profile becomes very similar to the chord-integrated intensity profile.

The normalized error of the intensity profile is defined as I_{error}/I_{brem}, where I_{error} means the difference between intensity profiles (I_{brem}) for a certain magnetic surface structure, e.g., β = 1.44% (8020), and other magnetic surface structures with different β value or pressure profile, e.g., β =1.56% (8020) or β = 1.44% (8080). The definition is also the same for the normalized error of the integrated-chord length profile (L_{error}/L_{chord}) and for that of the emissivity profile ($\varepsilon_{error}/\varepsilon_{brem}$). The I_{error}/I_{brem}, as plotted in Fig. 4.6(d), has large errors of ±15% and ±30% in the vicinities of ρ = 0.85 and ρ = 1.4 for all the assumed magnetic surface structures, respectively, while the radial structures are similar each other. On the contrary, the L_{error}/L_{chord} has a quite different radial structure for the four different magnetic surface structures, as seen in Fig. 4.6(e). The $\varepsilon_{error}/\varepsilon_{brem}$ is calculated using Eq.(4.4) from the results of Figs. 4.6 (d) and (e), as shown in Fig. 4.6(f). The profile of $\varepsilon_{error}/\varepsilon_{brem}$ is very similar to the I_{error}/I_{brem} profile for all the cases. The large difference in the L_{error}/L_{chord} does not give any effect on the final result of $\varepsilon_{error}/\varepsilon_{brem}$. Then, it is concluded that the error seen in the emissivity profile is caused by the chord-integrated intensity profile, 'I', in the Eq. (4.4), not the chord length matrix, 'L'. If we say simply, the determination of the normalized radius for each observation chord is very important in the magnetic surface deformation with the finite-β value. In the Z_{eff} analysis the error seen in the present emissivity profile directly transfers the same error to the Z_{eff} profile. The Z_{eff} profile has the same uncertainty of ±25% as the emissivity profile in the present discharge at the region of $0.8 \leq \rho \leq 1.0$ for the high-density discharge. The error originated in the Abel inversion is very small at core region in the peaked pressure profile. It should be noticed here that measured T_e and n_e profiles, in practice, make much large error in the Z_{eff} profile, as mentioned later.

Next, we consider the low-β discharge case with moderate density of $n_e = 4\times10^{13}\mathrm{cm}^{-3}$. The bremsstrahlung intensity, the integrated-chord length and the bremsstrahlung emissivity profiles are plotted in Figs. 4.7 (a), (b) and (c) for the inwardly shifted magnetic configuration with R_{ax} = 3.60m and β = 0.33% (8020). The intensity profile is slightly peaked, but the resultant emissivity profile becomes hollow. The I_{error}/I_{brem} are entirely constant inside ρ = 1.0 having very small error except for the edge region of $\rho \geq 1.0$. The result is clearly different from that in the high-β discharge. It also indicates less uncertainty of the magnetic surface structure in the low-β discharge. The above conclusion is again confirmed in the low-β discharge, because the relatively large error in the L_{error}/L_{brem} shown in Fig. 4.7(e) is not reflected in the $\varepsilon_{error}/\varepsilon_{brem}$. Then, the Abel inversion in the low-β discharges does not bring any big uncertainty to the Z_{eff} profile analysis.

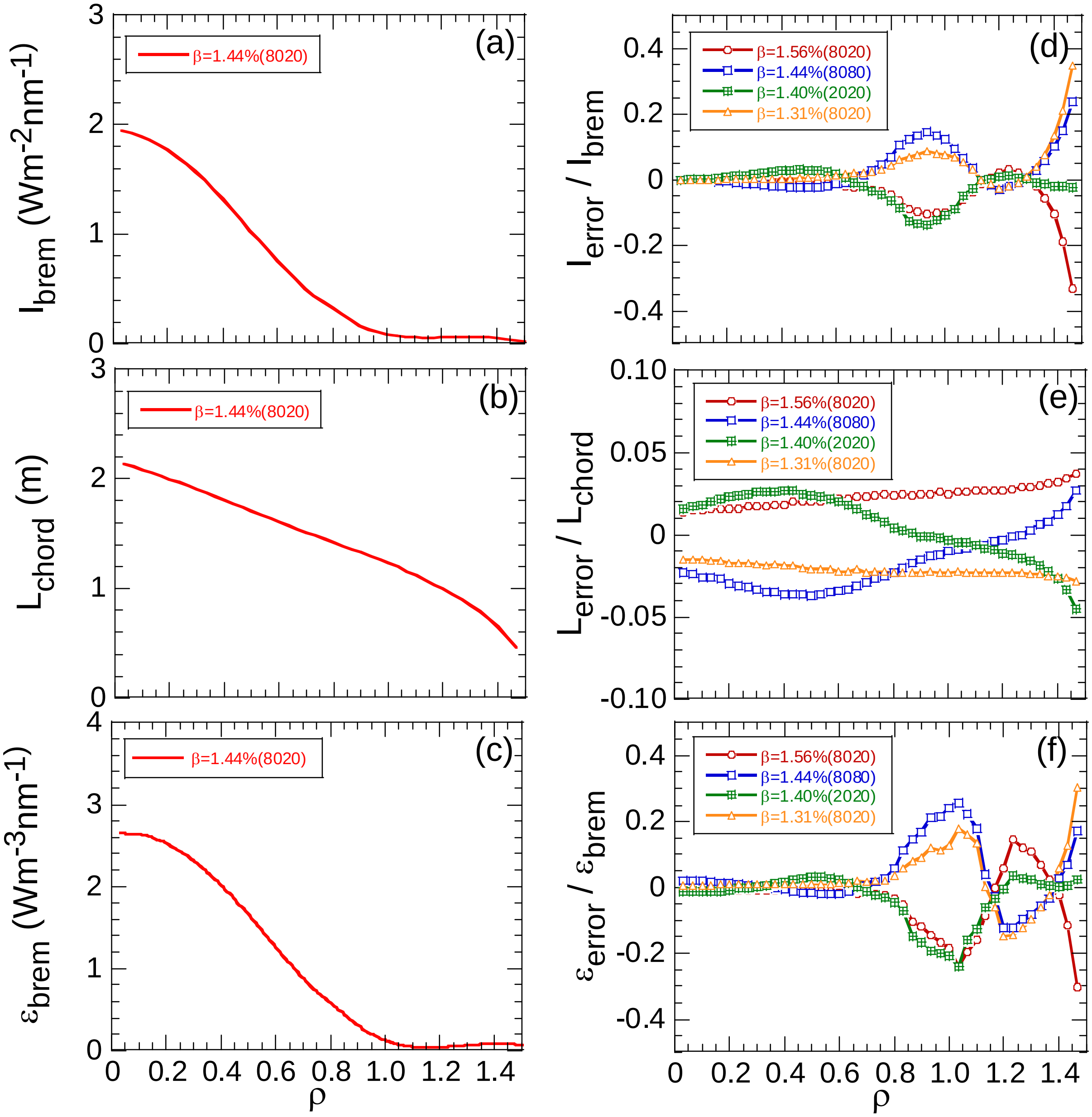

FIG. 4.6. (a) Chord-integrated bremsstrahlung intensity, I_{brem}, (b) observation chord length, L_{chord}, and (c) bremsstrahlung emissivity after Abel inversion for β = 1.44%(8020) at R_{ax}=3.85m and normalized errors of (d) chord-integrated bremsstrahlung intensity, I_{error}/I_{brem}, (e) observation chord length, L_{error}/L_{chord}, and (f) bremsstrahlung emissivity, $\varepsilon_{error}/\varepsilon_{brem}$ for different pressure profiles. 'β=1.44%(8020)' means pressure profile of $P(\rho)=P_0(1-\rho^8)(1-\rho^2)$ with volume-averaged beta of 1.44%, where P_0 is central pressure.

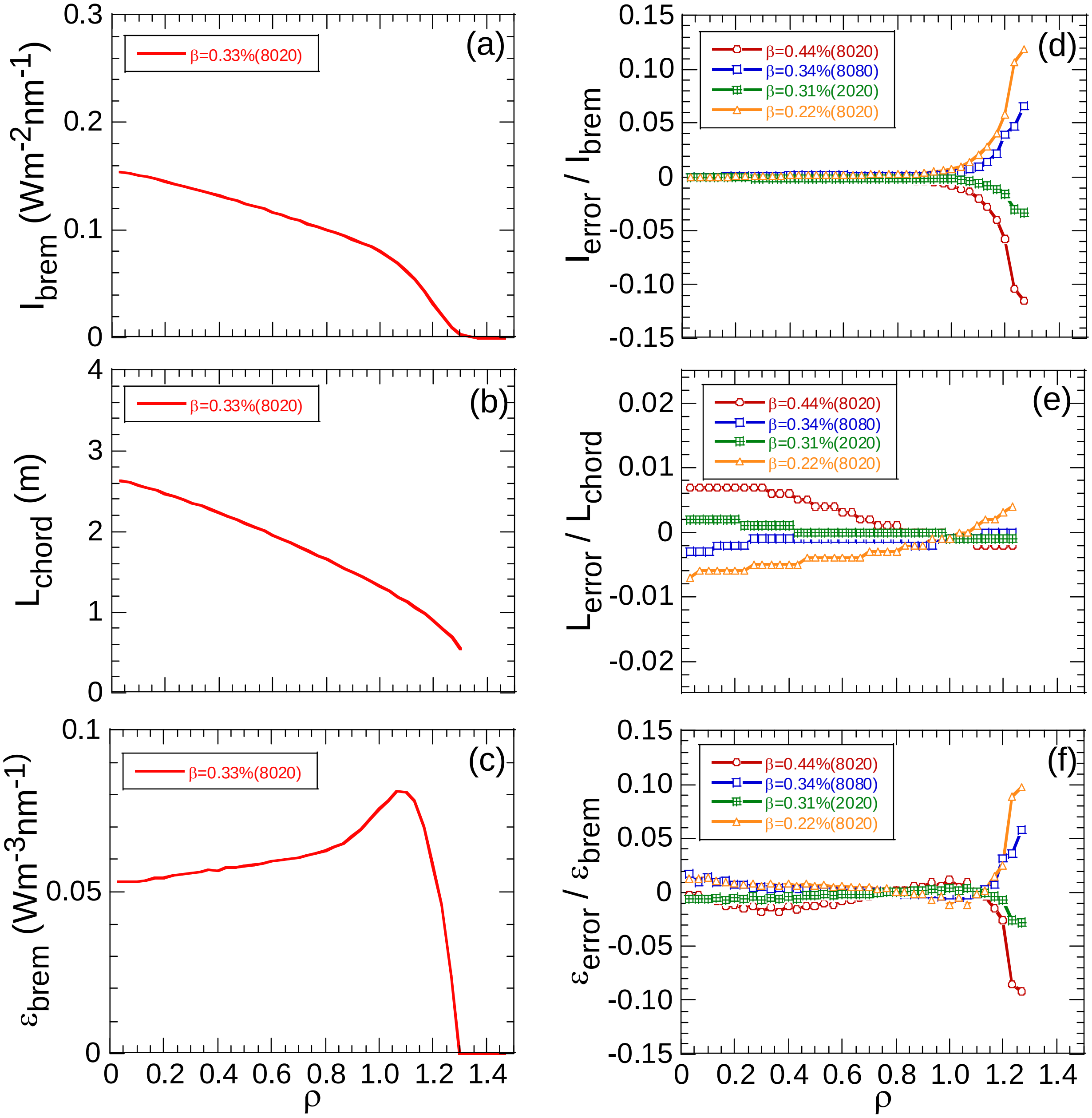

FIG. 4.7. (a) Chord-integrated bremsstrahlung intensity, I_{brem}, (b) observation chord length, L_{chord}, and (c) bremsstrahlung emissivity after Abel inversion for β = 0.33%(8020) at R_{ax}=3.60m and normalized errors of (d) chord-integrated bremsstrahlung intensity, I_{error}/I_{brem}, (e) observation chord length, L_{error}/L_{chord}, and (f) bremsstrahlung emissivity, $\varepsilon_{error}/\varepsilon_{brem}$ for different pressure profiles. 'β=0.33%(8020)' means pressure profile of $P(\rho)=P_0(1-\rho^8)(1-\rho^2)$ with volume-averaged beta of 0.33%, where P_0 is central pressure.

4.5 Density dependence of bremsstrahlung emission

Since the bremsstrahlung intensity is a strong function of the electron density, it is important to examine the relationship between the density and the bremsstrahlung intensity. Figure 4.8(a) shows the intensity profile at different densities. The bremsstrahlung intensity profile has a similar shape for different densities. The density profile also shows a similar shape for different densities, as plotted in Fig. 4.8(b). The central value of the bremsstrahlung intensity increases from 0.044 to $0.33 \mathrm{Wm}^{-2}\mathrm{nm}^{-1}$, when the line-averaged density increases from $2.5\times10^{13}\mathrm{cm}^{-3}$ to $8.3\times10^{13}\mathrm{cm}^{-3}$. It resembles the quadratic relationship between the bremsstrahlung and the electron density. In order to examine the relationship in more detail, the line-integrated bremsstrahlung profiles in Fig. 4.8(a) are converted into local emissivity profiles using the Abel inversion technique. The result is shown in Fig. 4.8(c). The Abel inversion method used in the present analysis is described in section V in detail. A hollow emissivity profile is seen in all the cases. The bremsstrahlung emissivity at $\rho = 0.2$ is correlated to the density at the same normalized radial position. The result is plotted in Fig. 4.8(d). Fitting the data, we obtain the relationship that the bremsstrahlung emissivity, ε_b, is proportional to the square of the density such as $\varepsilon_b = 0.00158 n_e^2$. This relationship suggests that the value of Z_{eff}, which is mainly determined by the carbon density, is constant against the electron density (see Eq. (2.7)), whereas a little deviation is seen in low-density range ($2 \leq n_e \leq 4\times10^{13}\mathrm{cm}^{-3}$) indicating the increment in Z_{eff} value. In the extremely low-density region ($n_e < 2\times10^{13}\mathrm{cm}^{-3}$) denoted by the hatched area, it is difficult to analyze the reliable emissivity profile at present because of the uncertainty based on scattered intensities among observation chords. This can be resolved by the extension of the wavelength interval for determining the visible bremsstrahlung continuum.

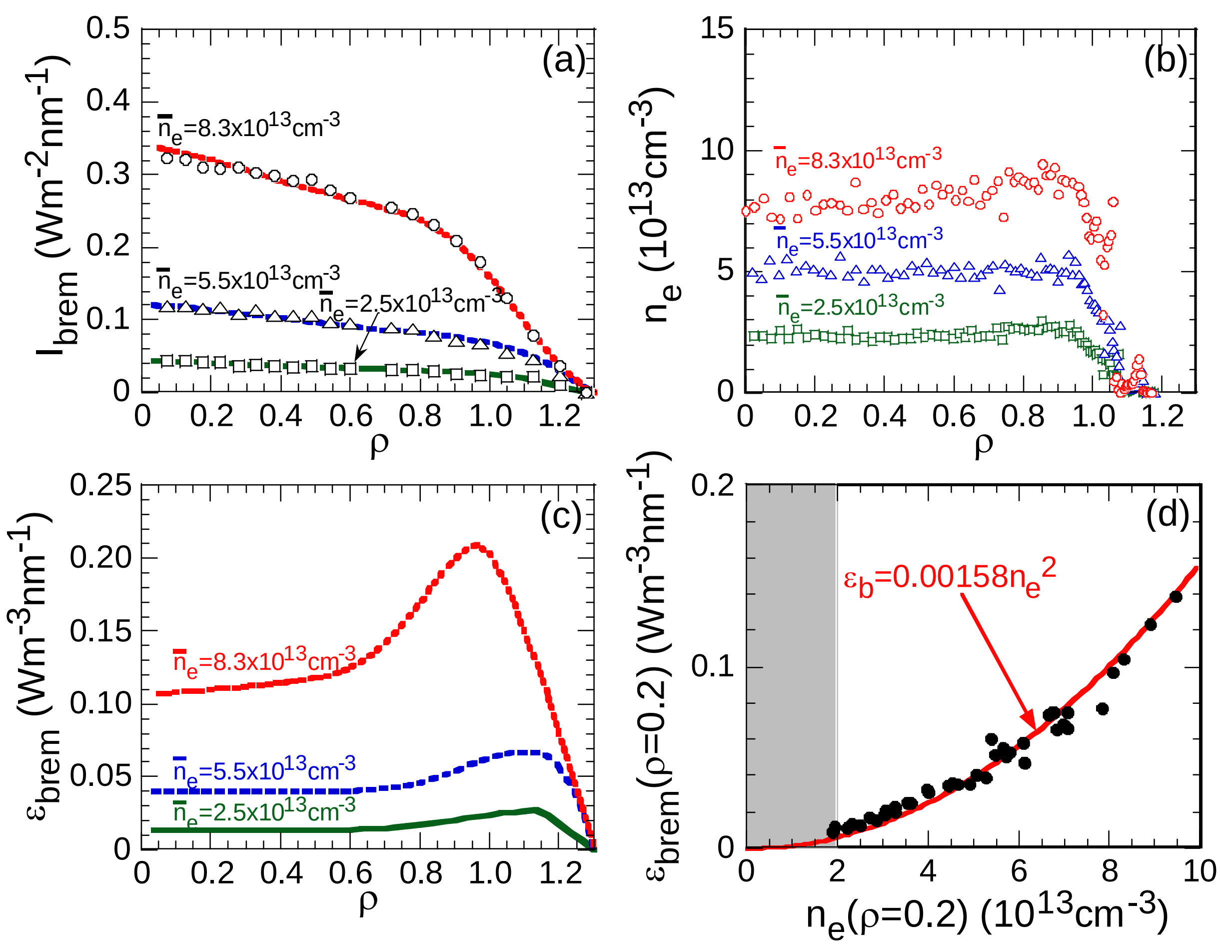

FIG. 4.8. (a) Chord-integrated bremsstrahlung intensity profiles, (b) electron density profiles, (c) bremsstrahlung emissivity profiles after Abel inversion for different density ranges as a function of normalized radius and (d) bremsstrahlung emissivity at ρ = 0.2 as a function of the density at ρ = 0.2. Solid, dashed and dotted curves indicate fitting curves. Hatched area in (d) indicates out of range for the present bremsstrahlung measurement.

4.6 Summary

The slice and stack method based on magnetic structures has been applied to LHD plasmas with nonaxisymmetric configurations and converted the chord-integrated bremsstrahlung intensity profile to the radial bremsstrahlung emissivity profile. The uncertainty of the emissivity calculated with Abel inversion technique due to the magnetic surface deformation is examined in two clearly different discharges with high-β and low-β values. For the high-β case, the error in the bremsstrahlung emissivity calculation is mainly caused by the uncertainty on the magnetic surface structure deformation based on the assumed incorrect pressure profile. For the low-β case, the error in the calculated emissivity is considerably small, in particular, within the LCFS. In the hollow bremsstrahlung emissivity profile, the iterative method is applied to reduce the effect of relatively low signal-to-noise ratio in the plasma center. The density dependence of bremsstrahlung emission has been checked in detail. The bremsstrahlung emissivity is proportional to the square of the density such as $\varepsilon_b = 0.00158n_e^2$.

References

[1] A. M. Cormack, J. Appl. Phys., 1964. **10**: p. 2908.

[2] K. Bockasten, J. Opt. Sco. Am., 1961. **51**: p. 943.

[3] W. Barr, J. Opt. Sco. Am., 1962. **52**: p. 885.

[4] N. Gottardi, J. Appl. Phys., 1979. **50**: p. 2647.

[5] H. Nozato, S. Morita, and M. Goto, J. Plasma Fusion Res. SERIES, 2002. **5**: p. 442.

[6] H. Y. Zhou, S. Morita, M. Goto and C. F. Dong J. Appl. Phys., 2010. **107**: p. 053306.

[7] S. P. Hirshman, W. I. V. Rij, and P. Merkel, Comput. Phys. Commum., 1986. **43**: p. 143.

[8] G. Gorini and N. Gottardi, *JET Joint Undertaking Report JET-R-(90)03,* 1990.

[9] H. K. Park, Rev. Sci. Instrum., 1990. **61**: p. 2879.

[10] A.T. Ramsey and M. Diesso, Rev. Sci. Instrum., 1999. **70**: p. 380.

[11] R. K. Paul, Rev. Sci. Instrum., 2007. **78**: p. 093701.

[12] Y. T. Cho and S.-J. Na, Meas. Sci. Technol., 2005. **16**: p. 878.

Chapter 5

Analysis of radial Z_{eff} profile

5.1 Introduction

In magnetically confined fusion plasmas, impurities make a substantial power loss through strong radiation. The study of the impurity behavior is significantly important, in particular, for the improvement of plasma performance in addition to the understanding of impurity transport [1-5]. In LHD, on the other hand, a variety of electron density profiles, i.e., peaked, flat and hollow profiles, is formed in different experimental conditions, whereas the peaked density profile is usually seen in tokamaks [6]. It is then important to investigate the impurity behavior under such different ion density profiles. High-density discharges up to 10^{15}cm^{-3} are produced with extremely peaked density profiles using H_2 multi-pellet injection [7], and C pellet [8] is also injected in LHD for density profile control. High-ion temperature discharges [9-10] are recently achieved by negative-ion-based neutral beam injection in high-Z discharges with peaked density profiles after Ne and Ar glow discharge cleaning. It is quite interesting to study the impurity transport in those discharges. For the purpose, Z_{eff} profile diagnostics is planned based on the absolutely calibrated measurement of bremsstrahlung continuum when the radial profiles of electron density and temperature are known.

Visible bremsstrahlung emission has been measured along the vertical direction of a horizontally elongated plasma cross section with an optimized Czerny-Turner-type visible spectrometer [11] installed on the LHD. The full vertical chord-integrated visible bremsstrahlung profile is observable, including the upper and lower edge emission, in a range of $-0.6\ \mathrm{m} \leq z \leq 0.6\ \mathrm{m}$. The instrument can entirely eliminate line emission from the bremsstrahlung signal, which was a serious problem in old bremsstrahlung measurement systems with an interference filter [12]. The new visible spectrometer system consists of a 44-fiber array, an astigmatism-corrected Czerny-Turner visible spectrometer, and a charge-coupled device (CCD). The vertical spatial and the time resolution are 30 mm and 100 ms, respectively. However, a nonuniform bremsstrahlung profile has still been observed after changing the diagnostic system. Detailed data analysis revealed that the nonuniform part of the signal originates in strong edge bremsstrahlung emission from a thick ergodic layer, since all the observation chords cover the edge emission. Fortunately, we could confirm that the lower half of the full vertical bremsstrahlung profile was not influenced by the edge emission in inwardly shifted magnetic configurations ($R_{ax} \leq 3.6$ m), where the ergodic layer is relatively thin. The local bremsstrahlung emission profile is obtained from chord-integrated signals through an Abel inversion, assuming an elliptical magnetic surface with the finite-β effect. The Z_{eff} profile is finally obtained, taking into consideration electron density and temperature profiles measured by the Thomson scattering diagnostic [13].

5.2 Experimental verification of measured Z_{eff} values

The Z_{eff} profile can be calculated with electron density and temperature profiles according to the Eq. (2.10) after analyzing the emissivity profile of the bremsstrahlung continuum. The Z_{eff} profile obtained by the present system is experimentally verified using discharges with H_2 multi-pellet and C pellet injections.

Six H_2 pellets are repetitively injected to the NBI discharge during 1.70-1.94s, as shown in Fig. 5.1(a). The average electron density quickly increases up to $2.1\times10^{14}\mathrm{cm}^{-3}$. At t = 1.95s after the pellet injection, the Z_{eff} profile is analyzed for the high-density plasma with $\beta = 1.44\%$. The electron density profile is peaked, plotted in Fig. 5.1(b), due to the central deposition of the hydrogen atoms by the pellet injection. The temperature profile, plotted in Fig. 5.1(c), is fairly flat in $\rho \leq 0.8$ and quickly decreases in $\rho > 0.8$. The bremsstrahlung emissivity profile similar to the density profile is shown in Fig. 5.1(d). The Z_{eff} profile is calculated from the three profiles. The result is plotted in Fig. 5.1(e). A totally flat Z_{eff} profile is formed in $\rho \leq 0.8$ with values of around 1.0 indicating the pure H_2 plasma. In $\rho > 0.8$, however, the value of Z_{eff} tends to increase with large uncertainty. The uncertainty due to the magnetic surface deformation is only 26%, which is similar to the

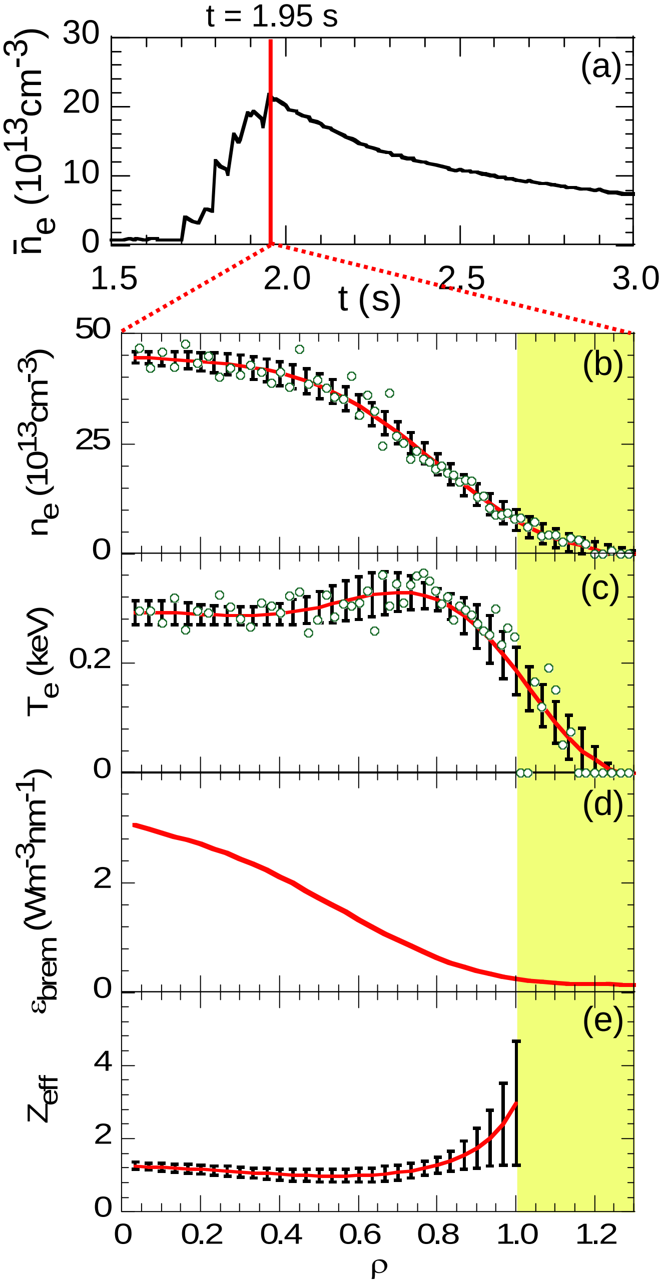

FIG. 5.1. (a) Waveform of electron density with H_2 multi-pellet injection and radial profiles of (b) electron density, (c) electron temperature, (d) bremsstrahlung emissivity after Abel inversion and (e) effective ion charge. Hatched areas indicate radial location where Z_{eff} profile analysis is difficult. Z_{eff} profile is analyzed at t=1.95s.

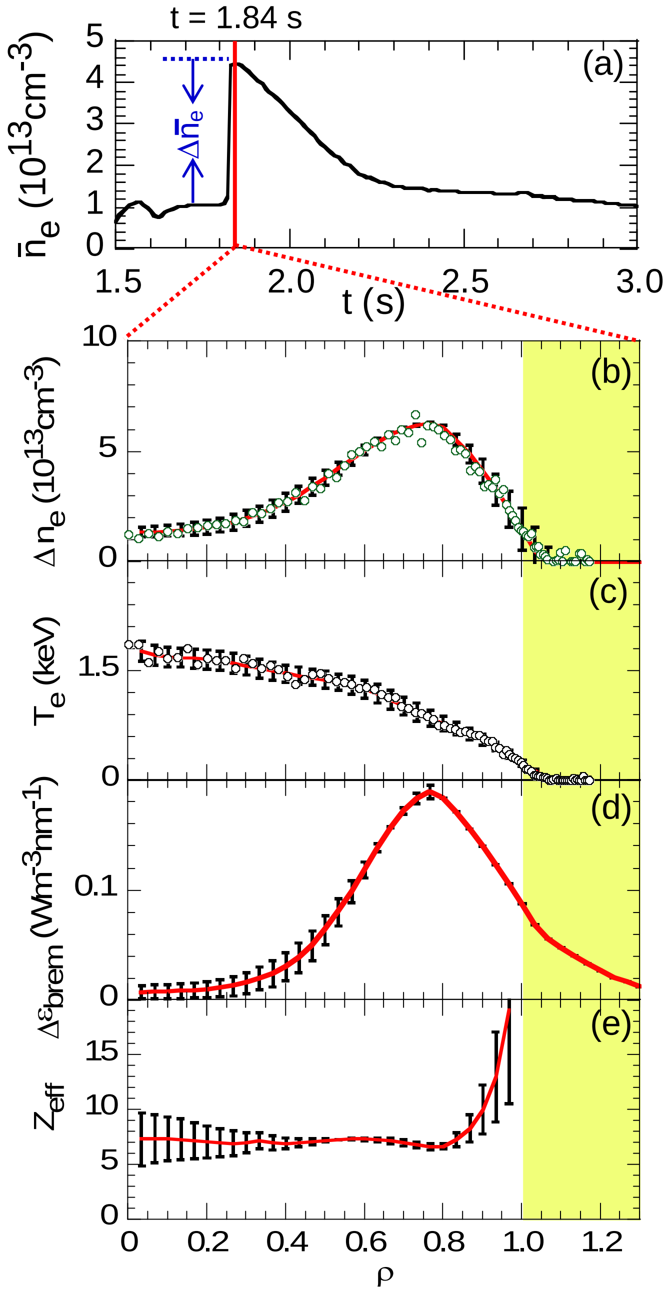

FIG. 5.2. (a) Waveform of electron density with C pellet injection and radial profiles of (b) electron density, (c) electron temperature, (d) bremsstrahlung emissivity after Abel inversion and (e) effective ion charge. Hatched areas indicate radial location where Z_{eff} profile analysis is difficult. Z_{eff} profile is analyzed at t=1.84s.

high-β plasma mentioned in chapter 4. The errors are mainly caused by the scattered electron density and temperature profiles. In particular, the uncertainty in the density profile gives a crucial effect in deriving the reliable Z_{eff} profile, whereas the error bars in the density profile (Fig. 5.1(b)) are smaller than ones in the temperature profile (Fig. 5.1(c)). Of course, it is originated in strong density and the weak temperature dependences of the visible bremsstrahlung emission as expressed by the Eq. (2.10).

Single C pellet, which has carbon ion density increment of 0.8×10^{13}cm^{-3}, is injected to the NBI discharges. The electron density drastically increases up to 4.5×10^{13}cm^{-3} as seen in Fig. 5.2(a). The Z_{eff} profile is analyzed at t = 1.84s when the density increment takes the maximum. At the moment the density increment profile, plotted in Fig. 5.2(b), is considerably hollow, while the temperature profile, plotted in Fig. 5.2(c), is peaked. The analyzed bremsstrahlung emissivity increment profile becomes further hollow, as shown in Fig. 5.2(d). The peak position at ρ=0.76 clearly indicates the radial location where the C pellet is deposited. The fairly flat Z_{eff} profile, plotted in Fig. 5.2(e), is also obtained with values of around 7, which suggests the formation of the pure carbon plasma. The reason why the value is a little bigger than 6 is unclear at present, although other impurities can contribute to the increment of the Z_{eff} value. The errors in the Z_{eff} profile appeared in $\rho \leq 0.4$ are resulted from weak bremsstrahlung emissivity in addition to a little scattered electron density and temperature profiles. The error is estimated to be about 40% in the plasma core. A large error in the Z_{eff} profile is, on the contrary, estimated in $\rho \geq 0.8$, which are mainly caused by uncertainties of density and temperature profiles. The density is disappeared at $\rho = 1.05$, whereas the bremsstrahlung emissivity profile is much broader at the plasma edge. At present we do not have reliable mapping of n_e and T_e to the coordinate along the lines of sight outside of LCFS. Hence, reliable analysis is difficult in this region.

5.3 Comparison of Z_{eff} profiles among different density profiles

Density profiles in the LHD change according to the heating power, magnetic field strength, magnetic axis position, and fueling method. A peaked density profile is easily produced by hydrogen multi-pellet injection. The Z_{eff} profile is analyzed for a peaked density profile formed in the high-density range with pellet injection. Figure 5.3 shows typical waveforms: (a) plasma stored energy W_p and H_α intensity, (b) line-averaged electron density $\overline{n_e}$, (c) central electron temperature T_{e0}, and (d) chord-integrated bremsstrahlung emission I_{brem}.

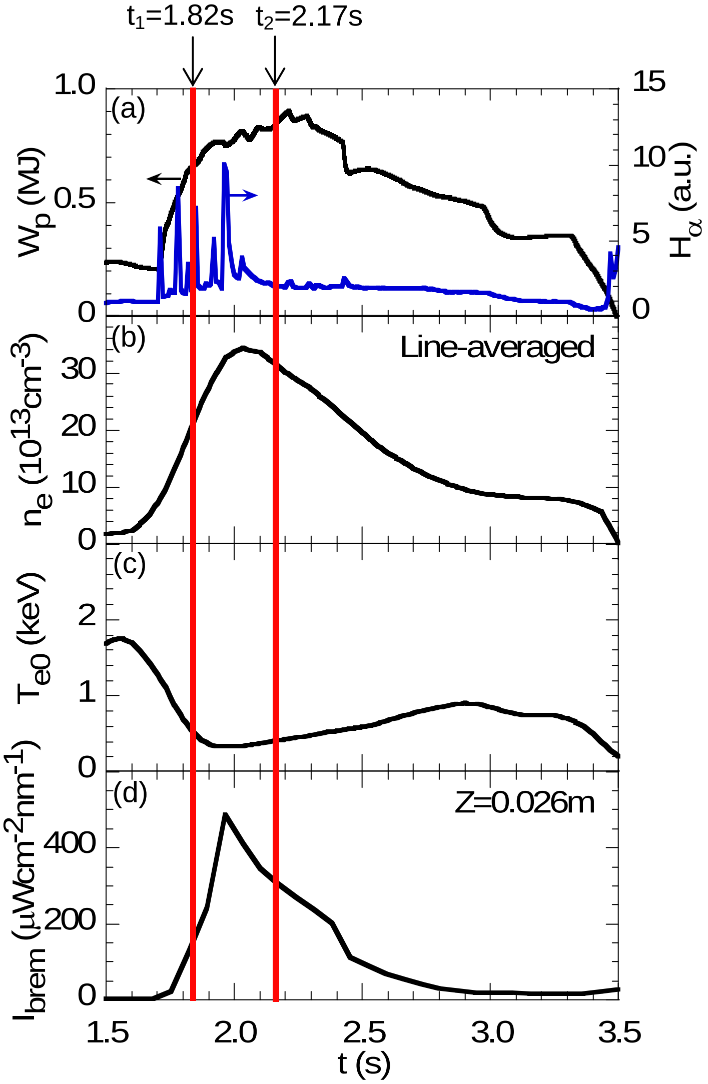

Fig. 5.3. Waveforms of high-density discharge with multi-pellet injection for peaked density profile: (a) Plasma stored energy W_p and H_α intensity, (b) Line-averaged electron density $\overline{n_e}$, (c) Central electron temperature T_{e0}, and (d) Chord-integrated bremsstrahlung emission I_{brem}. Z_{eff} profiles are analyzed at two different time slices, $t_1 = 1.82$ s and $t_2 = 2.17$ s, indicated by vertical lines.

Ten H_2 pellets were successively injected along magnetic axis of 3.85 m from 1.70–2.02 s. Plasma energy quickly increased during pellet injection and reached 0.9 MJ. The line-averaged electron density, evaluated from the density profile measured with Thomson scattering, continuously increased and reached 3.5×10^{14} cm^{-3}, whereas the electron temperature in the plasma center decreased drastically to 0.3 keV. Chord-integrated bremsstrahlung emission also increased in the same manner and reached quite a large value of 490 $\mu\mathrm{Wcm}^{-2}\mathrm{nm}^{-1}$. Here, the β value increased greatly, becoming 1.13%.

At 1.82 s after the third pellet injection, the radial Z_{eff} profile was analyzed with electron density and temperature profiles in addition to the local bremsstrahlung emissivity calculation based on the Abel inversion technique with $\beta = 1.07\%$. Figure 5.4 shows the radial distribution of plasma parameters for a super-dense core (SDC) plasma at $t_1 = 1.82$ s: (a) electron density n_{e}, (b) electron temperature T_{e}, (c) Abel-inverted bremsstrahlung emissivity $\varepsilon_{\mathrm{brem}}$, and (d) Z_{eff} from the above measurement. The radial distribution of $Z_{\mathrm{eff}}(\rho)$ in Fig. 5.4(d) is calculated based on the above three values: $n_{\mathrm{e}}(\rho)$, $T_{\mathrm{e}}(\rho)$, and $\varepsilon_{\mathrm{brem}}(\rho)$. The temperature profile is entirely flat at $\rho < 0.8$ and quickly decreases at $\rho > 0.8$. The outside boundary of the edge temperature expands to $\rho = 1.2$ in the ergodic layer. The bremsstrahlung emissivity profile is also peaked, like the density profile. The Z_{eff} profile analyzed from the peaked density profile is fairly flat in the core plasma region inside $\rho = 1.0$. The analysis of the Z_{eff} profile can be extended to $\rho \sim 1.13$. However, it is difficult to analyze Z_{eff} exactly, because uncertainties in the density and temperature profiles of Thomson scattering become large in the ergodic layer, which is denoted with square hatch marks in Fig. 5.4. The error bars of the Z_{eff} profile originating in the density and temperature profiles are quite small inside $\rho = 0.7$ but gradually increase at the edge plasmas, e.g., 23% at $\rho = 1.0$. The fitting curves for electron density and temperature profiles used in the present analysis are also indicated in Figs. 5.4 (a) and (b). Another important point regarding the uncertainty of the Z_{eff} profile is in the selection of a magnetic surface deformed by plasma pressure. The magnetic surface is of course necessary for Abel inversion of the line-integrated bremsstrahlung signal.

Figure 5.5 shows (a) n_{e}, (b) T_{e}, (c) $\varepsilon_{\mathrm{brem}}$, and (d) Z_{eff} at 2.17 s, just after pellet injection ends, indicated by a vertical line in Fig. 5.3. The radial bremsstrahlung emissivity is calculated based on the Abel inversion technique with $\beta = 1.94\%$. The electron density profile is more peaked with a higher density at the plasma core, and the outside density boundary is close to $\rho = 1.0$. This means the plasma size has shrunk. Meanwhile, the electron temperature is slightly lower than that at 1.82 s, but the profile is still flat. The

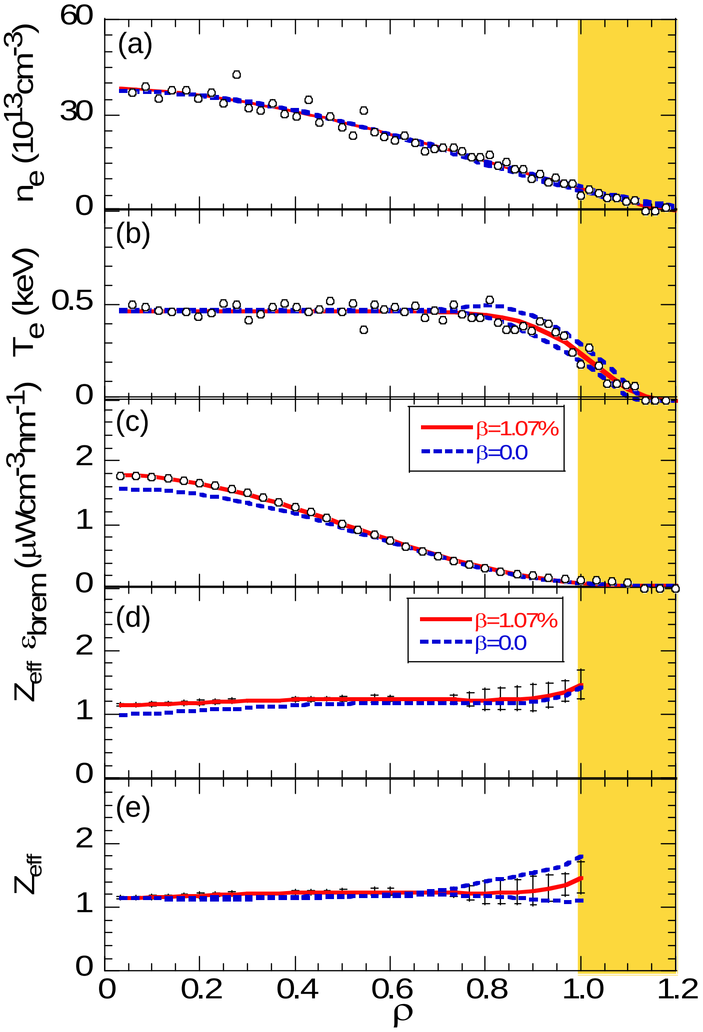

Fig. 5.4. Radial profiles of plasma parameters for a peaked density distribution as a function of normalized radius ρ at t_1 = 1.82 s, indicated in Fig. 5.3, during multi-pellet injection: (a) Electron density n_e, (b) Electron temperature T_e, (c) Bremsstrahlung emissivity after Abel inversion ε_{brem}, (d) Calculated effective ion charge from the above measurement of Z_{eff} for different magnetic surfaces, and (e) Calculated effective ion charge Z_{eff} with uncertainty due to scattered Thomson data. Dashed lines in (a), (b), and (e) indicate the uncertainty of the corresponding profile.

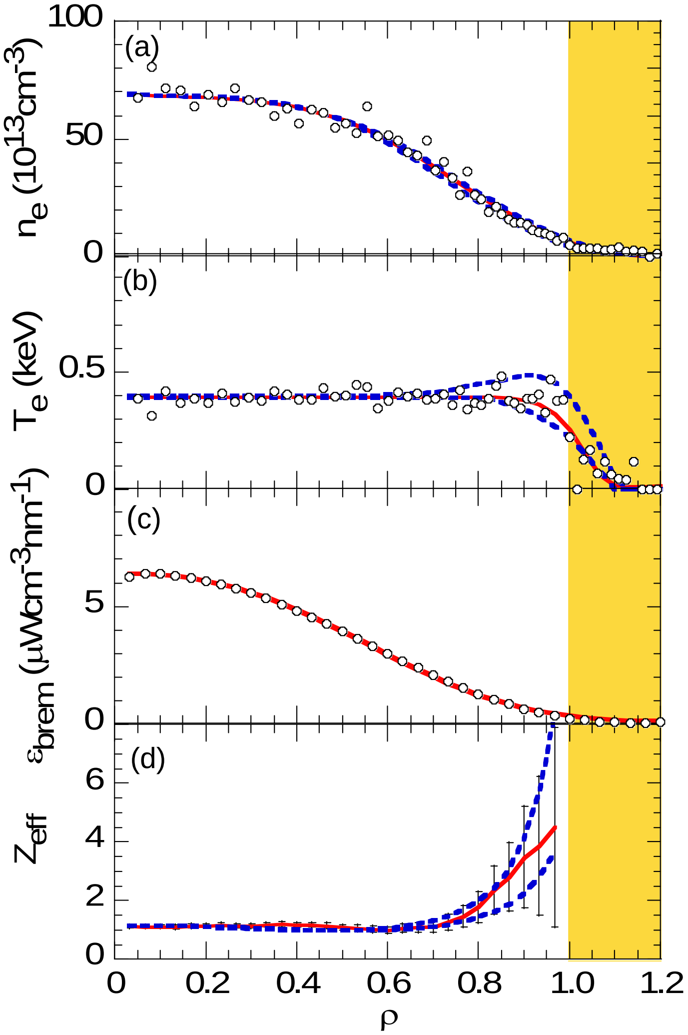

Fig. 5.5. Radial profiles of plasma parameters for a peaked density distribution as a function of normalized radius ρ at t_2 = 2.17 s, indicated by a vertical line in Fig. 5.3, after multi-pellet injection and super-dense core (SDC) plasma formation (a) n_e, (b) T_e, (c) ε_{brem}, and (d) Z_{eff} with uncertainty due to scattered Thomson data. Dashed lines in (a), (b), and (d) indicate the uncertainty of the corresponding profile.

bremsstrahlung emissivity profile then becomes more peaked than the density profile, as seen in Fig. 5.5(c). The analyzed Z_{eff} profile shown in Fig. 5.5(d) seems to also be flat, at least inside $\rho \leq 0.7$, and the values are distributed around 1.11. Although the error bars of Z_{eff} are quite small inside $\rho = 0.7$, they quickly increase with plasma radius. The error bars of Z_{eff}, caused only by uncertainty of the Thomson data, indicated by two dashed lines in Figs. 5.5 (a) and (b), are shown with dashed lines in Fig. 5.5 (d). However, these error bars of Z_{eff}, due to the edge density and temperature profiles, are about 50% of the total enlarged error bars outside of the plasma. The other source of error is quite unclear at present. As a possible source, we consider that these enlarged error bars originate in the magnetic surface structure used in the analysis. In SDC plasmas, an extremely large magnetic axis shift has been observed after pellet injection. It is then difficult to solve the magnetic surface structure in the usual way using VMEC calculation. Further theoretical study of magnetohydrodynamic (MHD) equilibrium is now being carried out to find accurate magnetic surface structure in such SDC plasmas with extremely peaked pressure profiles.

The uncertainty of the Z_{eff} profile due to magnetic surface deformation is checked at the plasma core using two different magnetic surfaces with $\beta = 0$ and 1.07%. The plasma axis shift used in the analysis is 0.2 m when $\beta = 1.07\%$. Two bremsstrahlung emissivity profiles obtained from the two magnetic surfaces, shown in Fig. 5.4(c), are quite similar, whereas a small difference appears in the plasma core. Since the visible bremsstrahlung emission is horizontally observed from the outboard side of the torus, the effect on the magnetic surface distortion becomes much less than that in vertical measurement. In particular, the difference in the Z_{eff} value can be neglected in the outer plasma region, because magnetic surface distortion occurs mainly in the plasma core. This strongly suggests that the uncertainty in the Z_{eff} profile on the assumed magnetic surface is quite small, at least in the plasma core, compared to that of the density and temperature profiles in the present diagnostic system with the exception of SDC plasmas. Another uncertainty of the Z_{eff} profile at the edge ($\rho \geq 0.75$) due to scattered Thomson data is shown with dashed lines in Fig. 5.4(e). The uncertainty of the density and temperature profiles are shown with dashed lines in Figs. 5.4(a) and (b), respectively. It is finally found that errors in the Z_{eff} profile are caused mainly by scattered Thomson data for the plasma at 1.82 s. In particular, the uncertainty of the edge density profile has a large effect on Z_{eff} error estimation, whereas the edge profile data are not scattered, as seen in Fig. 5.4(a).

Next, the Z_{eff} profile is analyzed for a flat density profile. The data are taken from stable plasma discharge at $R_{\mathrm{ax}} = 3.6$ m. Figure 5.6 shows the discharge waveforms of

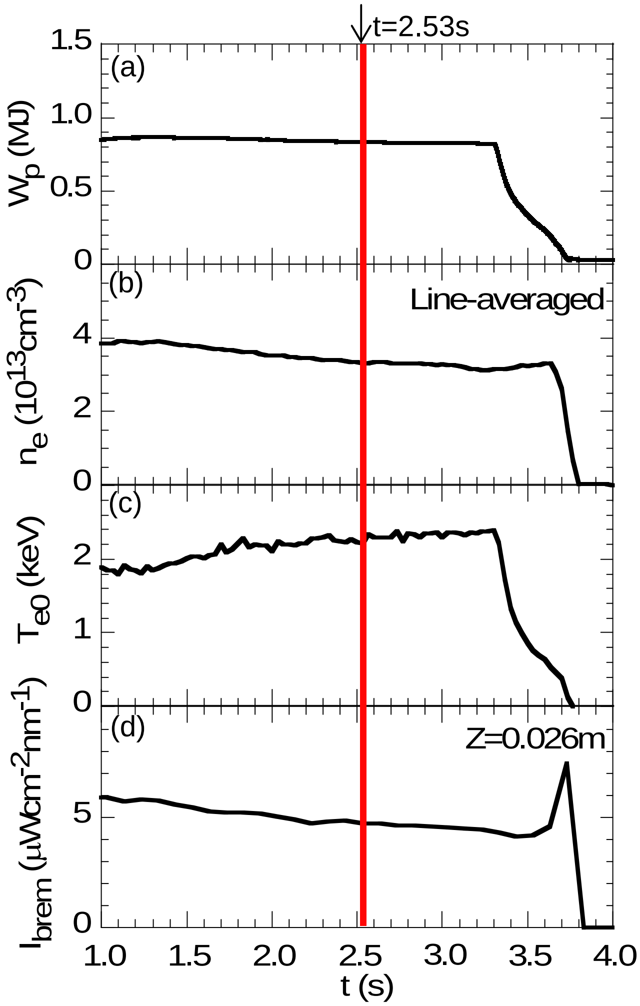

Fig. 5.6. Waveforms of stable discharge for flat density profile: (a) W_p, (b) n_e, (c) T_{e0}, and (d) I_{brem}.

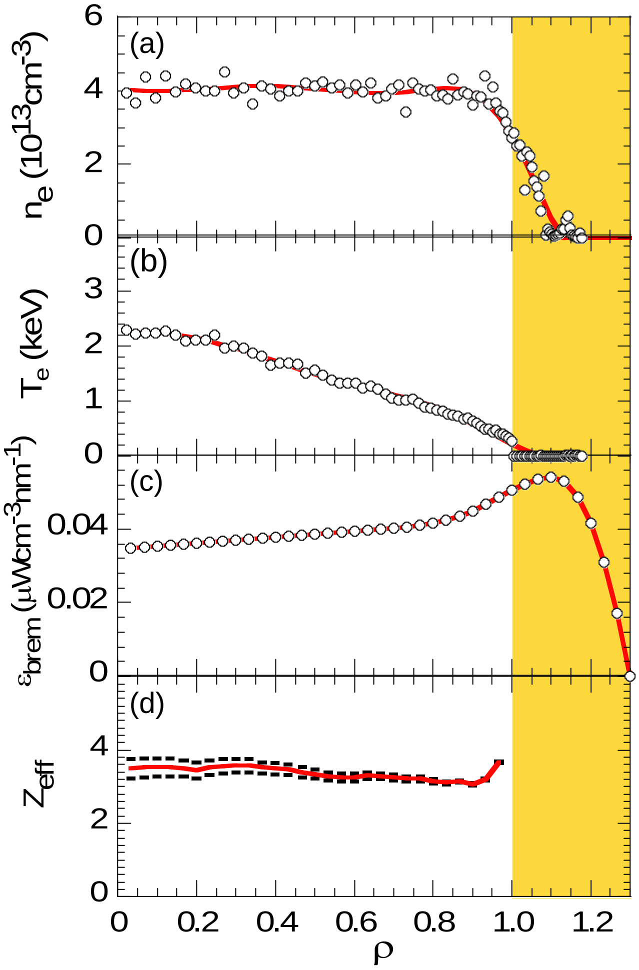

Fig. 5.7. Radial profiles as a function of normalized radius ρ at t = 2.53 s, indicated by a vertical line in Fig. 5.6: (a) n_e, (b) T_e, (c) ε_{brem}, and (d) Z_{eff}.

SN#85124: (a) plasma stored energy W_p, (b) line-averaged electron density $\overline{n_e}$, (c) central electron temperature T_{e0}, and (d) chord-integrated bremsstrahlung emission I_{brem} at Z = 0.026 m. The plasma energy is constantly sustained from 0.8 s to 3.3 s. The line-averaged electron density is kept at roughly 3.5×10^{13} cm^{-3}, and the central electron temperature increases slightly, from 2.0 keV to 2.2 keV, during the steady phase according to the gradual decrease in the density. The chord-integrated bremsstrahlung emission behaves similarly to the density. The β value is 0.88% at the steady phase. Figure 5.7 shows radial profiles of (a) n_e, (b) T_e, (c) $\varepsilon_{\mathrm{brem}}$, and (d) Z_{eff} at 2.53 s in Fig. 5.6. The density profile is entirely flat at $\rho < 0.9$, whereas the temperature profile is peaked. The bremsstrahlung emissivity profile after Abel inversion becomes slightly hollow. This indicates that there is little temperature dependence in the visible bremsstrahlung emission. The Z_{eff} profile is flat, with values near 3.4. Analysis in the ergodic layer is still difficult. The error bars of the Z_{eff} profile gradually increase toward the plasma core; the maximum error bar appears as 12% at the plasma center. Clearly, the increase in the error bars at the plasma core originates in the local emissivity calculation of the bremsstrahlung based on the Abel inversion method, in addition to error bars from density profile fitting from $0.2 < \rho < 0.4$.

The hollow density profile is observed in the density rise phase at R_{ax} = 3.60 m. Figure 5.8 shows the discharge waveforms. The line-averaged electron density gradually increases from 0.5–1.5 s and finally reaches 6×10^{13} cm^{-3}, although the plasma energy remains constant. The central plasma temperature then decreases from 1.8 to 1.2 keV. The chord-integrated bremsstrahlung emission also increases according to the density rise. The β value is 0.58% in the discharge. Figure 5.9 depicts radial profiles of (a) n_e, (b) T_e, (c) $\varepsilon_{\mathrm{brem}}$, and (d) Z_{eff} at 1.13 s in Fig.8. A hollow density profile forms, having its peak value at $\rho = 0.9$. In contrast, the temperature profile is peaked and forms a triangular shape. The bremsstrahlung emissivity decreases greatly at the plasma core, and the profile becomes hollower than the density profile. The Z_{eff} profile is also flat, with values around 2.3. In the case of a hollow density profile, analysis is generally difficult because of relatively large error bars in the density profile and difficulty in calculating the Abel inversion. The error bars in the Z_{eff} profile also increase in this case, i.e., ~14%, at the plasma core.

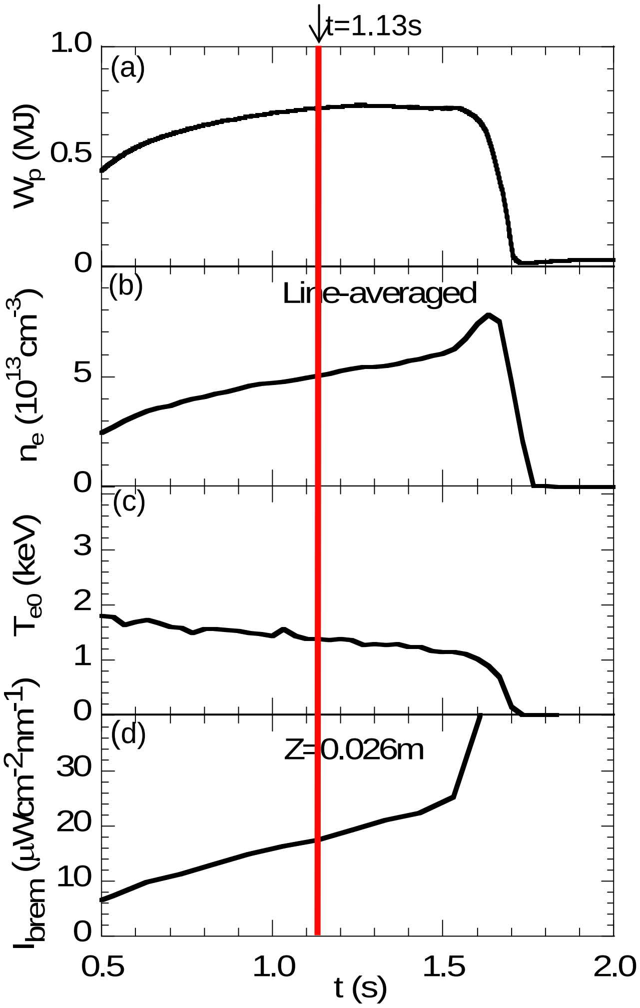

Fig. 5.8. Waveforms of density rise discharge for hollow density profile: (a) W_p, (b) n_e, (c) T_{e0}, and (d) I_{brem}.

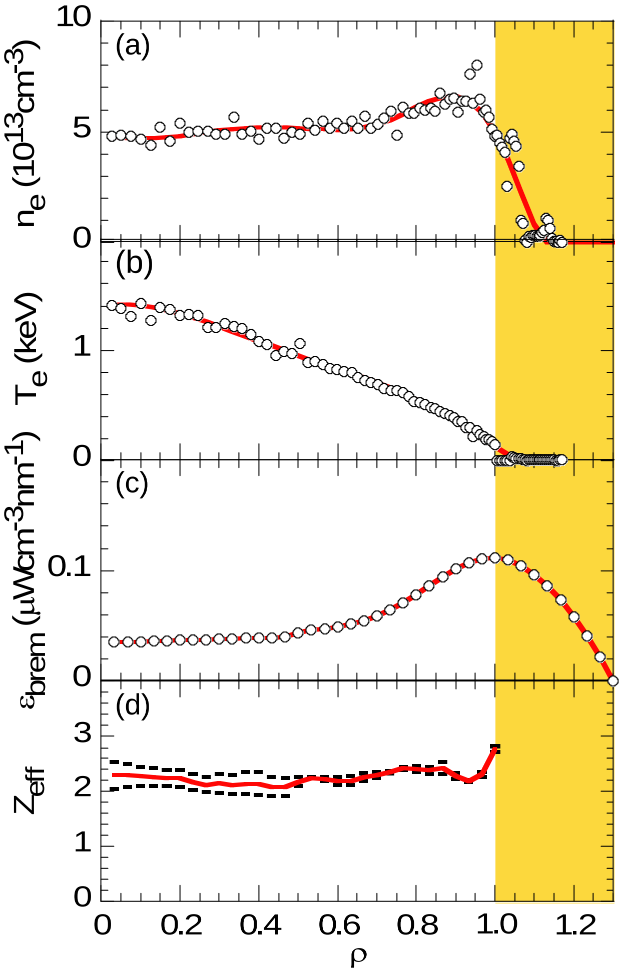

Fig. 5.9. Radial profiles at 1.13 s, indicated by a vertical line in Fig. 5.8, as a function of normalized radius ρ: (a) n_e, (b) T_e, (c) ε_{brem}, and (d) $Z_{eff.}$

5.4 Z_{eff} profiles for NBI discharges with single C pellet

Z_{eff} profile is studied in NBI discharges with single C pellet injection. Typical waveforms of the discharge are plotted in Fig. 5.10 as (a) plasma stored energy, W_p, and carbon emission, CIV, (b) line-averaged electron density, n_e, (c) central electron temperature, T_{e0}, (d) chord-integrated bremsstrahlung emission, I_{brem} at Z = 0.026m. The hatched area during t = 1.85-2.01s denotes density decay phase after the C pellet injection. A cylindrical C pellet with the size of $\phi 1.4mm^2 \times 1.4mm$ is injected by pressurized helium gas from the impurity pellet injector. After the carbon emission largely increases at the plasma edge, the electron density is drastically increased and reaches peak value of 4.5×10^{13} cm^{-3}, whereas the electron temperature is decreased from 3keV to 2keV. The chord-integrated bremsstrahlung emission is also quickly increased. Here, it should be noticed that the sampling time of 80ms in the visible bremsstrahlung signal is much longer than those in other signals. During the decay phase, the plasma stored energy is slowly recovered with gradual reduction of the electron density and the electron temperature.

The profile of Z_{eff} during the density decay phase is analyzed at the three different discharge times denoted with vertical lines in Fig. 5.10 for the transport study. The result is shown in Fig. 5.11(a) as a function of normalized radius. The value of Δt means the elapsed time after the pellet injection. The effect of the C pellet injection is clearly seen in the Z_{eff} profiles of which the central values are increased from 2.0 to 5.6. The carbon ion density profile can be derived from the Z_{eff} profile because the Z_{eff} value is uniquely given by the carbon. The result is plotted in Fig. 5.11(b) at three different discharge times. The density profile at Δt = 72ms clearly indicates that the injected carbon pellet is ablated at ρ = 0.65. The vertical dashed line indicates the radial position of at ρ = 0.45 in the figure indicates a critical position in the carbon radial transport. The carbon ion density increases from 0.05 to 0.5 $\times10^{13}$ cm^{-3} inside the critical position and decreases outside the critical position. The carbon ions seem to behave the radial transport to recover the flat Z_{eff} profile.

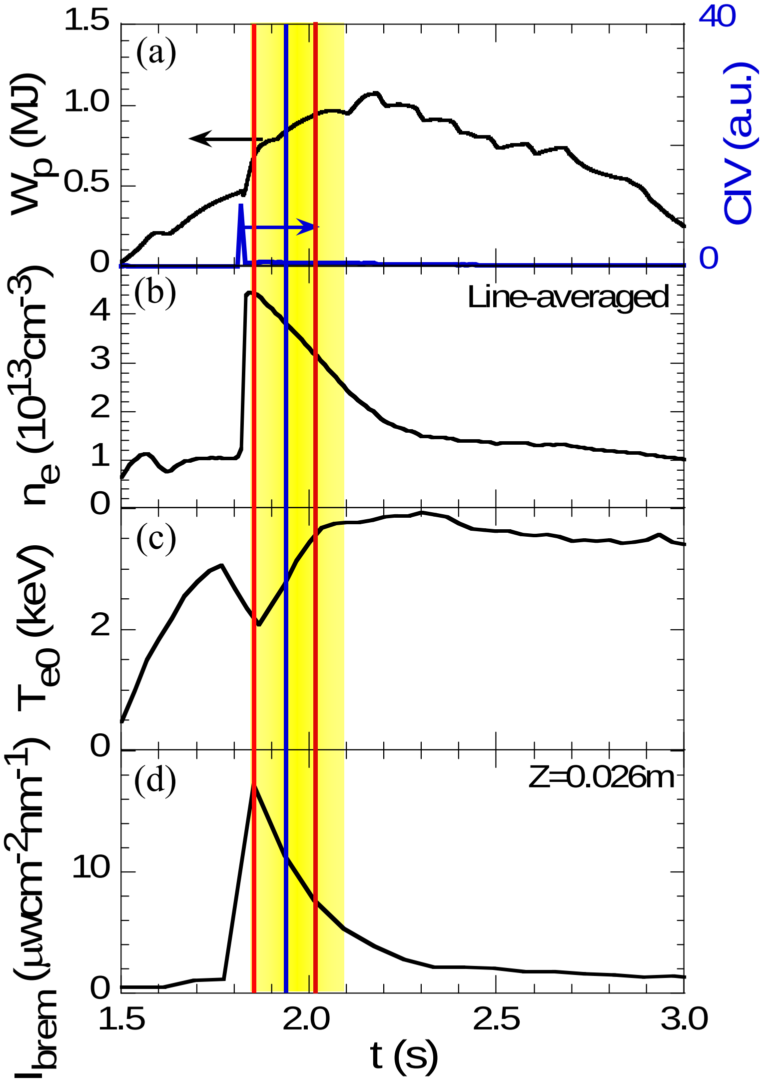

Fig. 5.10. Discharge waveforms with single C pellet injection: (a) W_p and CIV, (b) n_e, (c) T_{e0}, and (d) I_{brem}. Hatched area denotes density decay phase after C pellet injection and three vertical lines indicate the timing for profile analysis.

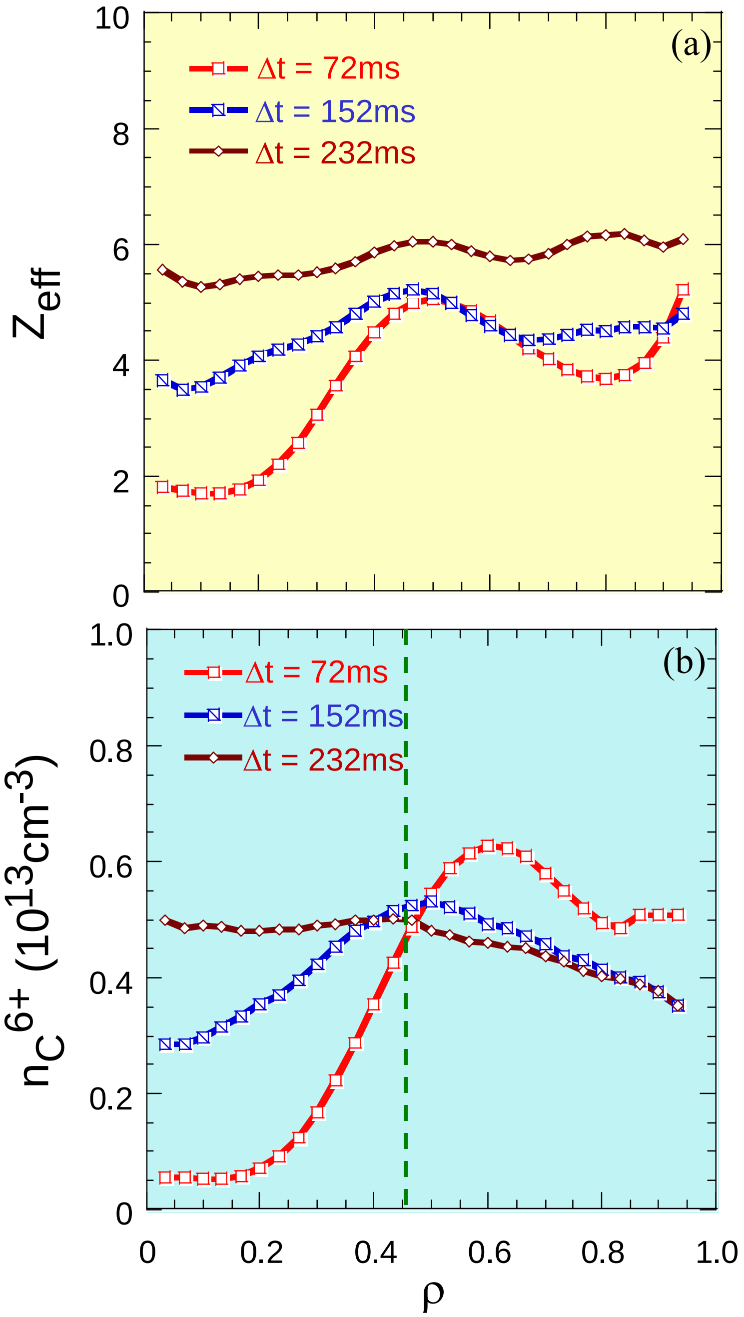

Fig. 5.11. (a) Z_{eff} and (b) carbon ion density profiles for three different discharge times during the density decay phase denoted in Fig. 5.10 as a function of normalized radius. Vertical dashed line at ρ = 0.45 indicates critical radial position and Δt means the elapsed time after C pellet injection.

5.5 Summary

The present Z_{eff} diagnostics system is experimentally verified in discharges with H_2 multi-pellet and C pellet injections. Reasonable Z_{eff} values are obtained for both two cases. Z_{eff} profiles from visible bremsstrahlung measurement are analyzed for peaked, flat, and hollow density profiles in LHD plasmas. An essentially flat Z_{eff} profile is obtained for all different density profiles. This indicates that the impurity partial pressure is constant in typical LHD discharges. The error bars seen in the Z_{eff} profiles originate mainly in fitting curves to express the electron temperature and density profiles and in calculating the Abel inversion calculation. The uncertainty in magnetic surface distortion is relatively small except for SDC plasmas. Evolvement of Z_{eff} profiles has been reported in NBI discharges with single C injection. Further impurity transport analysis is being progressed followed by optimizing the magnetic surface used in the calculation and modifying the method of calculating the Abel inversion.

References

[1] R. D. Petrasso, D. J. Sigmar, K. W. Wenzel et al., Phys. Rev. Lett., 1986. **57**: p. 707.

[2] R. B. Howell, J. Terry, and E.S. Marmar, Rev. Sci. Instrum., 1990. **61**: p. 3087.

[3] J. A. Konings, G. M. D. Hogeweij, N. J. Lopes Cardozo et al., Nucl. Fusion, 1997. **37**: p. 199.

[4] H. Nozato, S. Morita, M. Goto et al., Phys. Plasmas, 2004. **11**: p. 1920.

[5] H. Nozato, S. Morita, M. Goto et al., Phys. Plasmas, 2006. **13**: p. 092502.

[6] F. Wagner and U. Stroth, Plasma Phys. Controlled Fusion, 1993. **35**: p. 1321.

[7] R. Sakamoto,, M. Kobayashi, J. Miyazawa et al., Nucl. Fusion, 2009. **49**: p. 085002.

[8] R. Katai,, S. Morita, M. Goto et al., Jpn. J. Appl. Phys., 2007. **46**: p. 3667.

[9] Y. Takeiri, S. Morita, K. Ikeda et al., Nucl. Fusion, 2007. **47**: p. 1078.

[10] S. Morita, M. Goto, Y. Takeiri et al., Nucl. Fusion, 2003. **43**: p. 899.

[11] H. Y. Zhou, S. Morita, M. Goto and M. B. Chowdhuri et al., Rev. Sci. Instrum., 2008. **79**: p. 10F536.

[12] H. Nozato, S. Morita, and M. Goto, J. Plasma Fusion Res. SERIES, 2002. **5**: p. 442.

[13] K. Narihara, I. Yamada, H. Hayashi et al., Rev. Sci. Instrum., 2001. **72**: p. 1122.

Chapter 6

Evaluation of total bremsstrahlung radiation

6.1 Introduction

Since the bremsstrahlung radiation is caused by the acceleration of charged particles and practically emitted by electrons in high-temperature plasmas based on the free-free coulomb collision with ions, the amount of the bremsstrahlung largely depends on the electron density. Therefore, the bremsstrahlung radiation becomes crucial in high-density operation of fusion devices [1-2], although the energy confinement can be generally improved with the density. In next-generation fusion devices with D-T burning such as International Thermonuclear Experimental Reactor (ITER), the bremsstrahlung radiation plays a significant role [3] on the heat load reduction of plasma facing components [4-5] in addition to the impurity line radiation at plasma edge. The impurity radiation has been studied in many devices [6-8] using noble gases such as neon and argon. However, the bremsstrahlung radiation [9] has not been experimentally studied so far. In LHD, high-density discharges [10] ($n_e<10^{14}cm^{-3}$) have been recently achieved in NBI-sustained plasmas by injecting hydrogen multi-pellets. An alternative direction to fusion reactor is considered in such a high-density operational regime, which is basically free of Greenwald limit [11] seen in tokamaks. Investigation on the bremsstrahlung radiation profile followed by the study of total bremsstrahlung radiation loss is thus important in high-density discharges of LHD.

Visible bremsstrahlung emission and its spatial profile have been newly measured using a visible spectrometer [12] with an optical fiber array instead of an interference filter. The line emission [13] is successfully eliminated from the signal with the new approach, whereas the contamination of the line emissions was a main problem in the visible bremsstrahlung measurement with interference filter. The pure bremsstrahlung emission can be obtained in several wavelength intervals of the visible spectrum, e.g., 530-540nm. Local bremsstrahlung emissivity is then analyzed from the line-integrated visible bremsstrahlung profile using Abel inversion method, in which the magnetic surface deformation due to β-effect is taken into account [14]. The radial bremsstrahlung emission profile can be calculated in different energy ranges as a function of electron temperature. The total bremsstrahlung radiation is thus obtained by integrating the local bremsstrahlung emissivity against the plasma volume and the energy. The use of soft X-ray profile measurement is difficult in the high-density operation of LHD, since the electron temperature is considerably low. The present method gives the best way to determine the total bremsstrahlung radiation in a wide range of the electron temperature.

6.2 Experimental setup

The visible bremsstrahlung intensity profile is measured by a spectroscopic system consisting of an astigmatism-corrected Czerny-Turner-Type visible spectrometer, a charge-coupled device (CCD) and a 44 optical fibers parallel array. The fiber array is installed on LHD along the vertical direction ($-0.6\text{m} \le Z \le 0.6\text{m}$) for viewing the whole vertical profile at horizontally elongated plasma cross section. Optical lenses are placed in front of the optical fibers to define a spatial resolution for each chord. The spatial resolution of the chord is 30mm at the plasma center. The spectral range of 460-600nm is usually measured at the central wavelength of 530nm with 300 grooves/mm grating. The wavelength interval of 530-540nm is commonly considered to be free of line emissions in magnetically confined high-temperature plasmas. It is also confirmed in LHD discharges. The CCD is operated in multi-track mode with time resolution of 80 or 100ms. The present diagnostic system is absolutely calibrated using a standard integrating sphere under the same geometric arrangement as the real experimental setup. The electron density and temperature profiles are measured by YAG Thomson scattering system [15]. The line-averaged density is also derived from the Thomson data.

Since the magnetic field for plasma confinement of LHD is in principle produced by a pair of helical coils with toroidal/poloidal pitch numbers of 2/10, the magnetic surface becomes elliptical and stochastic magnetic field region, so called 'ergodic layer', is naturally created at the outside of the core plasma due to the presence of higher Fourier components of the helical coils. Although the major radius, R, of the helical coils is 3.9m, the plasma axis position, R_{ax}, can be easily changed by vertical field coils in a range of $3.5 \le R_{ax} \le 4.1$m. The averaged minor radius of the LHD plasma, a, takes the maximum value of 0.64m at R_{ax}=3.6m, so called 'standard configuration'.

Most of discharges are fueled by H_2 gas puffing from the plasma periphery, and heated and maintained by neutral beam injection (NBI). Here, we define these discharges as 'gas-puff discharge'. In these discharges the averaged-electron density, n_e, is stably maintained up to 10^{14}cm^{-3}. In the present study the visible bremsstrahlung profile is measured during stable phase of the gas-puff discharges in range of $3.0 \le n_e \le 9.5 \times 10^{13}$cm^{-3} under the beam deposition power, P_{NBI_dep}, $4 \le P_{NBI_dep} \le 10$MW, which denotes the birth beam deposition. Then, the beam deposition power is equal to the port-through power at higher densities. Typical waveforms in the gas-puff discharges with R_{ax}=3.6m configuration are shown in Figs. 6.1(a)-(d). The discharge is constantly sustained at $n_e = 5.0 \times 10^{13}$cm^{-3} during 1.5s. The visible bremsstrahlung intensity at central chord plotted in (d) also seems to be constant, whereas the central electron temperature is decreased with reduction of the NBI deposition power at t=1.3s. The visible bremsstrahlung emission is insensitive to the electron temperature due to the extremely low photon energy (~2eV).

On the other hand, the solid H_2 multi-pellets are injected in NBI plasmas to increase the density and to make better fueling efficiency instead of the gas puff fueling. Most of the H_2 pellets are deposited near the plasma center except for the first few pellets. The operational range in LHD is reasonably extended with the H_2 pellet injection up to the central electron density of 10^{15}cm^{-3}. Here, we define these discharges as 'pellet discharge'. The bremsstrahlung profile is analyzed for the pellet discharges in range of $10 \le n_e \le 40 \times 10^{13}$cm^{-3} and $8 \le P_{NBI_dep} \le 14$MW. Typical discharge waveforms are shown in Figs. 6.1(f)-(j). Nine H_2 pellets are injected in outwardly shifted configuration of R_{ax}=3.85m during a short time of t=1.7-2.1s. The line-averaged density quickly increases and reaches 50×10^{13}cm^{-3} under P_{NBI_dep}=14MW, while the central electron temperature drastically decreases to 0.2

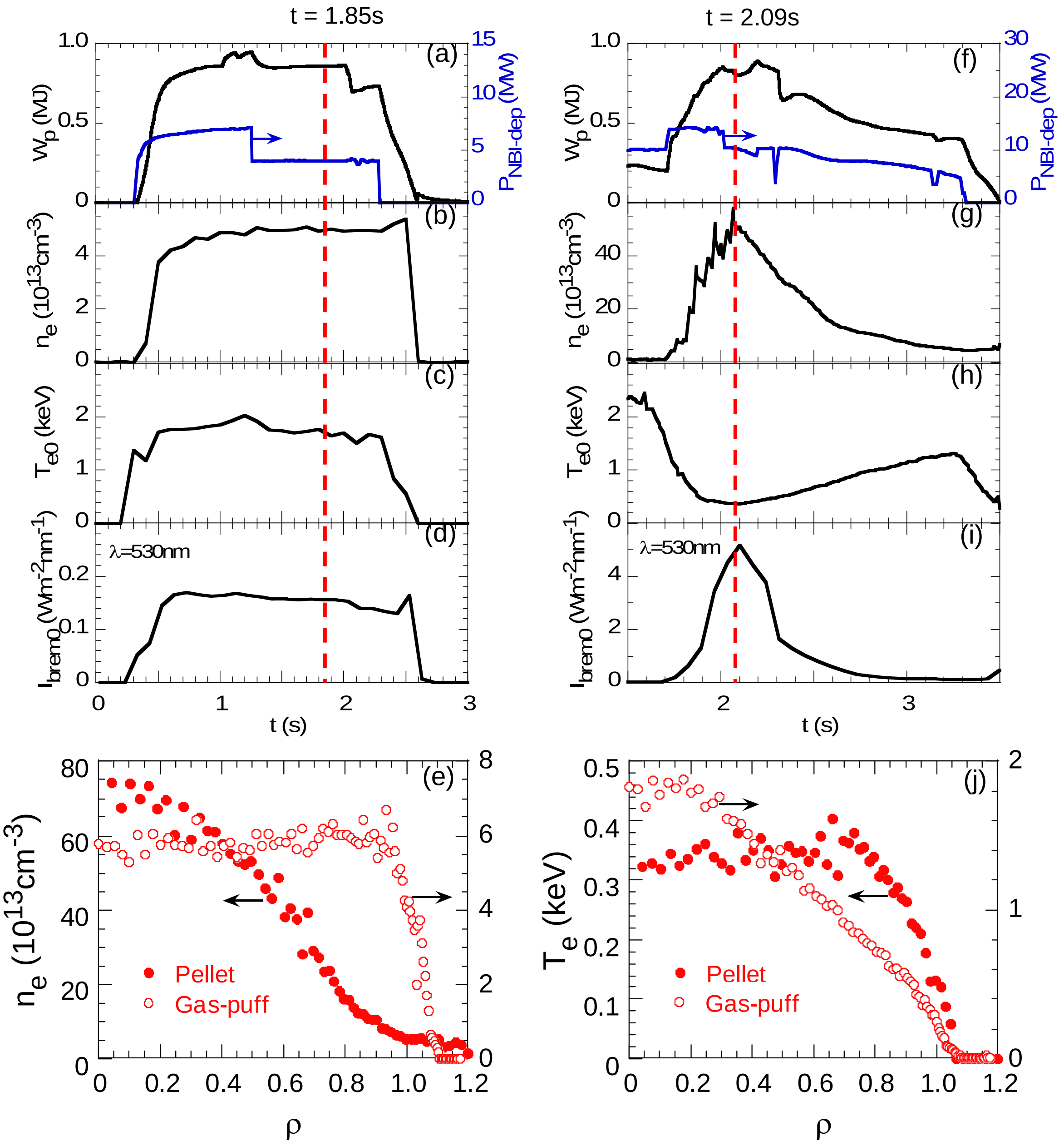

FIG. 6.1. Typical waveforms of (a)-(d) gas-puff discharge and (f)-(i) pellet discharge ((a), (f): plasma stored energy and NBI birth deposition power, (b), (g): line-averaged electron density, (c), (h): central electron temperature and (d), (i): central bremsstrahlung intensity) and radial profiles of (e) electron density and (j) electron temperature. Vertical dashed lines in waveforms indicate time frames at which radial profiles are measured by Thomson diagnostic.

keV. The visible bremsstrahlung intensity at the central chord also behaves similarly to the electron density (see Fig. 6.1 (i)).

The electron density and temperature profiles are compared between the two clearly different discharges, as shown in Figs. 6.1(e) and (j), respectively. The data are taken at t=1.85s for the gas-puff discharge and at t=2.09s for the pellet discharge. The density profile is entirely peaked in the pellet discharge, whereas it is slightly hollow in the gas-puff discharge. In contrast, the temperature profile is slightly hollow in the pellet discharge, but it is peaked in the gas-puff discharge. The visible bremsstrahlung emissivity profile for the two discharges is discussed in section 6.4.

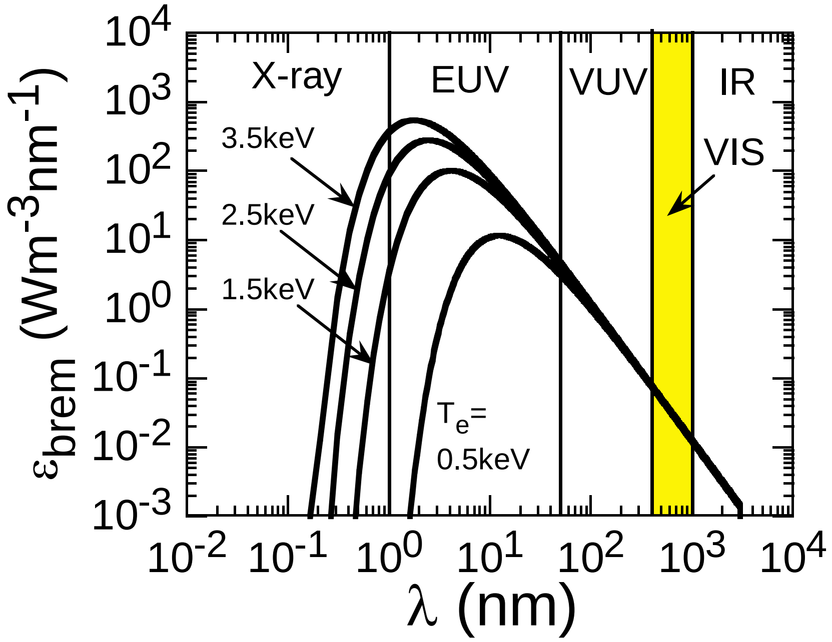

FIG. 6.2. Calculated bremsstrahlung radiation as a function of wavelength for different central electron temperatures. Wavelength range is divided in five ranges of X-ray (λ≤1nm), EUV (1≤λ≤50nm), VUV (50≤λ≤400nm), visible (400≤λ≤1000nm: hatched area) and infrared (1000≤λ≤3000nm).

6.3 Analysis of total bremsstrahlung radiation

In high-temperature plasmas, the bremsstrahlung radiation is mainly generated by the acceleration of electrons based on the Coulomb collision with fuel and impurity ions. The radiation power of the bremsstrahlung per unit wavelength is expressed as

$$\varepsilon_\lambda = \frac{1.89\times10^{-28} n_e^2 Z_{eff} g_{ff}}{T_e^{1/2}\lambda^2}\exp(-\frac{12400}{T_e\lambda})\ (\mathrm{W\cdot cm^{-3}\cdot Å^{-1}}), \tag{6.1}$$

where n_e, T_e and λ are the electron density ($\mathrm{cm^{-3}}$), the electron temperature (eV) and the wavelength of the bremsstrahlung emission (Å), respectively. Here, the effective ion charge, Z_{eff}, is defined by

$$Z_{eff} = \frac{\sum_{j,z} n_{j,z} Z_j^2}{\sum_{j,z} n_{j,z} Z_j} = \frac{\sum_{j,z} n_{j,z} Z_j^2}{n_e}, \tag{6.2}$$

where $n_{j,z}$ is the ion density in a charge state of certain ion species, Z_j. The gaunt-factor, g_{ff}, can be approximated by the following equation [16] in the range of 0.03 keV ≤ T_e ≤ 10.0 keV;

$$g_{ff} = 1.35 T_e^{0.15}. \tag{6.3}$$

Figure 6.2 illustrates the bremsstrahlung radiation spectra as a function of wavelength for different electron temperatures. The electron density of $6\times10^{13}\mathrm{cm^{-3}}$ and Z_{eff} value of 2.0, which are typical parameters in LHD, are assumed in the calculation. The hatched area denotes the wavelength range where the visible bremsstrahlung is measured. The bremsstrahlung radiation power in the X-ray (λ<1nm) and EUV (extreme ultraviolet: 1≤λ≤50nm) ranges is almost three orders of magnitude stronger than that in the visible region, while such shorter wavelength ranges are sensitive to the electron temperature. Therefore, the X-ray and EUV bremsstrahlung radiation practically determine the total bremsstrahlung radiation. In order to derive the bremsstrahlung radiation from LHD plasmas as a function of wavelength, the Eq. (6.1) can be replaced by

$$\varepsilon_\lambda = \varepsilon_{\lambda 0}\lambda_0^2 \exp\left(-\frac{12400}{T_e\lambda}\right) \Big/ \left(\lambda^2 \exp\left(-\frac{12400}{T_e\lambda_0}\right)\right), \tag{6.4}$$

where $\varepsilon_{\lambda 0}$ is the visible bremsstrahlung radiation measured at certain visible wavelength of λ_0. The total bremsstrahlung radiation is thus obtained by integrating the whole wavelength range and the plasma volume of LHD as follows

$$P_{brems\_tot} = \int_{v}\int_{\lambda} \varepsilon_{\lambda} d\lambda dV \ . \tag{6.5}$$

The radial profiles of the bremsstrahlung and the electron temperature and density are of course taken into account in the calculation of the total bremsstrahlung radiation.

6.4 Core bremsstrahlung radiation in different density regimes

6.4.1 Emissivity profile of bremsstrahlung radiation

An nonuniform visible bremsstrahlung profile is frequently observed when the vertical profile is measured at horizontally elongated plasma cross section in the gas-puff discharge, as shown in Fig. 6.3(a). It is found that the visible bremsstrahlung consisting of the nonuniform part at the upper-half profile in the figure is originated in the edge ergodic layer near the inboard side X-point (also see Fig. 3.2). Since the temperature is sufficiently low and the density is high in the ergodic layer, the visible bremsstrahlung radiation becomes relatively strong. In particular, the low temperature and high density plasma is widely distributed at the inboard side of the ergodic layer. In the lower half profile denoted with hatched area, however, the effect of the nonuniform plasma in the ergodic layer seems to be very less, because the observation chord does not include the inboard side X-point. The local bremsstrahlung emissivity profile can be then obtained from the lower half profile. The Abel inversion method is applied to the lower half profile taking into account the deformation of the magnetic surface due to the plasma pressure. The result is shown in Fig. 6.3(b). The local emissivity profile is hollow and the peak emission is appeared in the ergodic layer ($1.0< \rho\leq 1.3$).

In contrast, a symmetric visible bremsstrahlung profile is usually observed in the pellet discharge, as plotted in Fig. 6.3(c). In the pellet discharge the bremsstrahlung profile is extremely peaked as well as the density profile. The edge bremsstrahlung radiation in the ergodic layer is negligible compared to the core radiation. The profile is always symmetric in the pellet discharges for all the magnetic configurations. Figure 6.3(d) shows the localized bremsstrahlung emissivity profile after Abel inversion. The emissivity profile is also peaked and the edge boundary seems to shrink, i.e., ρ=1.0. As a result, the bremsstrahlung radiation in the pellet discharge is two orders stronger than that in the gas-puff discharge at the plasma center, because the Z_{eff} values are similar each other.

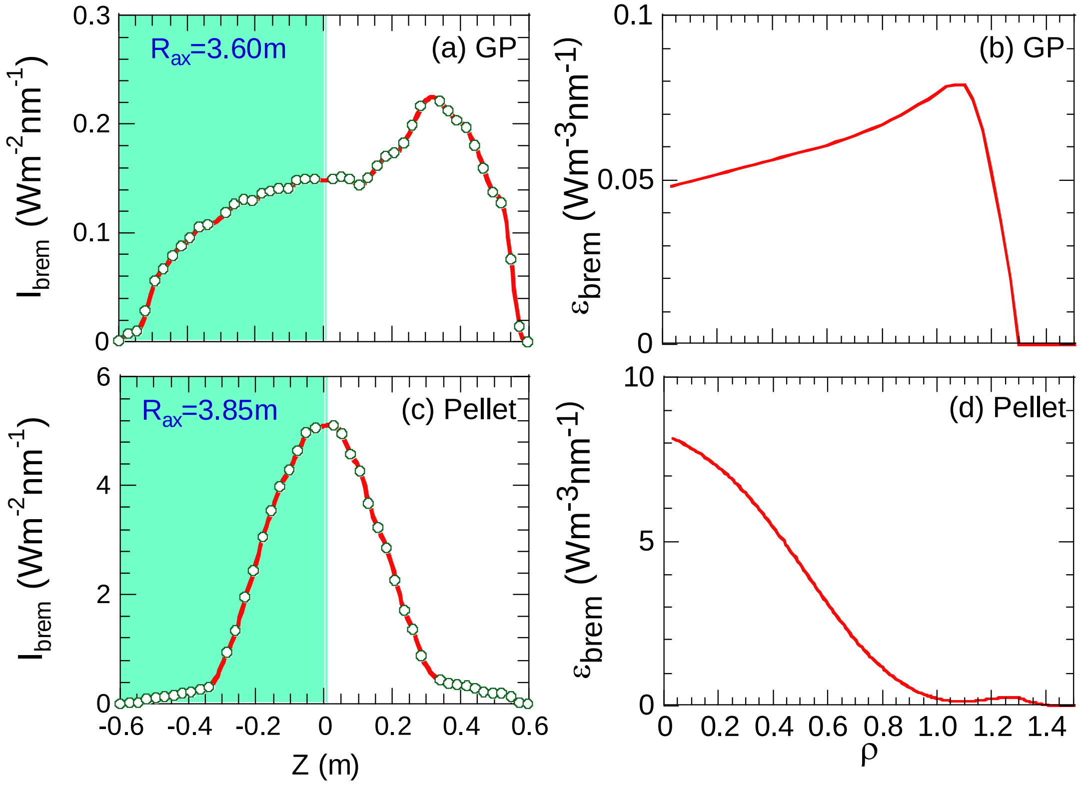

FIG. 6.3. Typical visible bremsstrahlung profiles measured along vertical direction in horizontally elongated plasma cross section for (a) gas-puff discharge and (c) pellet discharge and local emissivity bremsstrahlung profiles against normalized radius for (b) gas-puff discharge and (d) pellet discharge. Hatched areas in (a) and (c) indicate lower half of the profile used for Abel inversion.

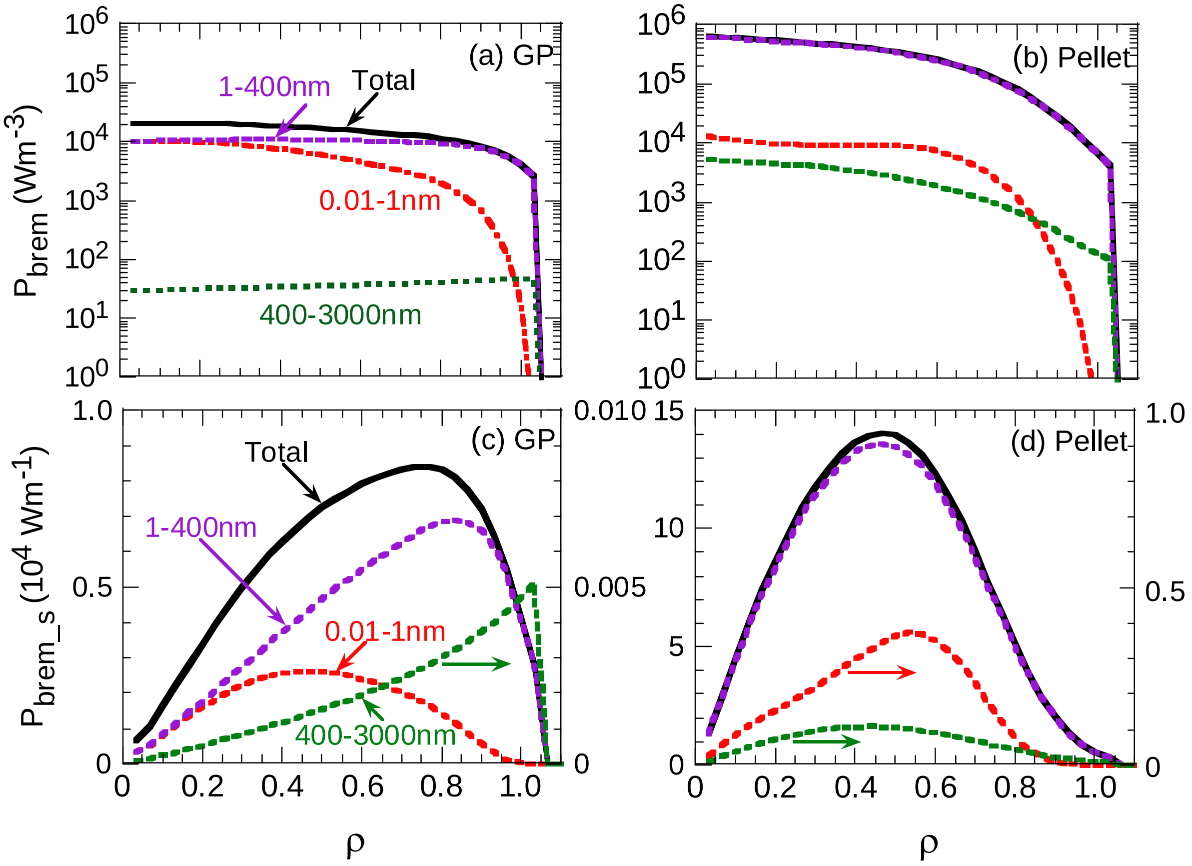

FIG. 6.4. Wavelength-integrated bremsstrahlung radiation per unit volume, P_{brem}, for (a) gas-puff discharge and (b) pellet discharge and bremsstrahlung radiation per unit normalized radius, P_{brem_s}, calculated by integrating the toroidal volume between two adjacent magnetic flux surfaces for (c) gas-puff discharge and (d) pellet discharge as a function of normalized radius.

Next, the local bremsstrahlung emissivity is calculated as a function of wavelength using Eq. (6.4). It should be noticed that the bremsstrahlung profiles are only derived in the core region of $\rho \leq 1.05$, since the uncertainty of the temperature profile measured with the Thomson scattering diagnostic becomes large in $\rho > 1.05$. The bremsstrahlung radiation profile is calculated by integrating certain wavelength interval as wavelength-integrated bremsstrahlung radiation, P_{brem}. The wavelength-integrated bremsstrahlung profiles calculated are shown in Figs. 6.4 (a) and (b) for gas-puff and pellet discharges, respectively. It is understood that the bremsstrahlung radiation in EUV and VUV ranges occupies the dominant part in the total bremsstrahlung radiation power for the both discharges. The fraction of the P_{brem} occupied by both of the EUV and VUV ranges to the total P_{brem} is estimated to be 71% and 97% for the gas-puff and pellet discharges, respectively. The P_{brem} in X-ray range is usually dominant in the central column of the plasma. This fraction is approximately 28% for the gas-puff discharge, but it is much small (2.3%) for the pellet discharge. The P_{brem} in the visible range is quite low, in particular, for the gas-puff discharges.

The bremsstrahlung radiation power per unit volume (P_{brem}) is replaced into the bremsstrahlung radiation power per unit normalized radius, which is calculated by integrating the toroidal volume (P_{brem_s}) between two adjacent magnetic flux surfaces. Using the P_{brem_s} we can easily find the radial location in which the bremsstrahlung radiation power takes the maximum. The results are shown in Figs. 6.4(c) and (d) for the gas-puff and pellet discharges, respectively. The peak value of the P_{brem_s} locates in $\rho=0.75$ for the gas-puff discharge, but it moves to inner side for the pellet discharge, i.e., $\rho=0.48$. It indicates that the radiation loss can be reduced at the outside of the plasma in the high-density discharges with the pellet injection, suggesting the favorable character for the performance improvement of discharges.

6.4.2 Density dependence of total bremsstrahlung radiation

Total bremsstrahlung radiation, P_{brem_tot}, is derived by integrating the wavelength (0.01-3000nm) and plasma volume ($\rho \leq 1.05$) in the local bremsstrahlung radiation. Figure 6.5 shows the relation between the total bremsstrahlung radiation and the line-averaged electron density for different magnetic axis configurations. The solid curve is a calculation with assumptions of T_e=0.4 keV and Z_{eff} =1.5 and other two dashed curves are calculated with assumptions of T_e=0.4±0.2 keV and Z_{eff} =1.5. The parameters assumed in the calculation are usually seen in the pellet discharge case. In LHD the accessibility to high-density operation using the pellet injection is much easier in the outwardly shifted configurations (R_{ax}≥3.75m) than in inwardly shifted configurations (R_{ax}≤3.60m). It is believed that the difference is originated in the MHD stability. Therefore, the high-density operation becomes difficult in R_{ax}=3.575m. The P_{brem_tot} is almost constant against n_e in the gas-puff discharge regime, whereas it quickly increases with n_e in the pellet discharge regime, as scaled by the square of n_e. The maximum value of the total bremsstrahlung radiation around 3.5 MW is observed in the extremely high-density discharge at $n_e=3\times10^{14}cm^{-3}$.

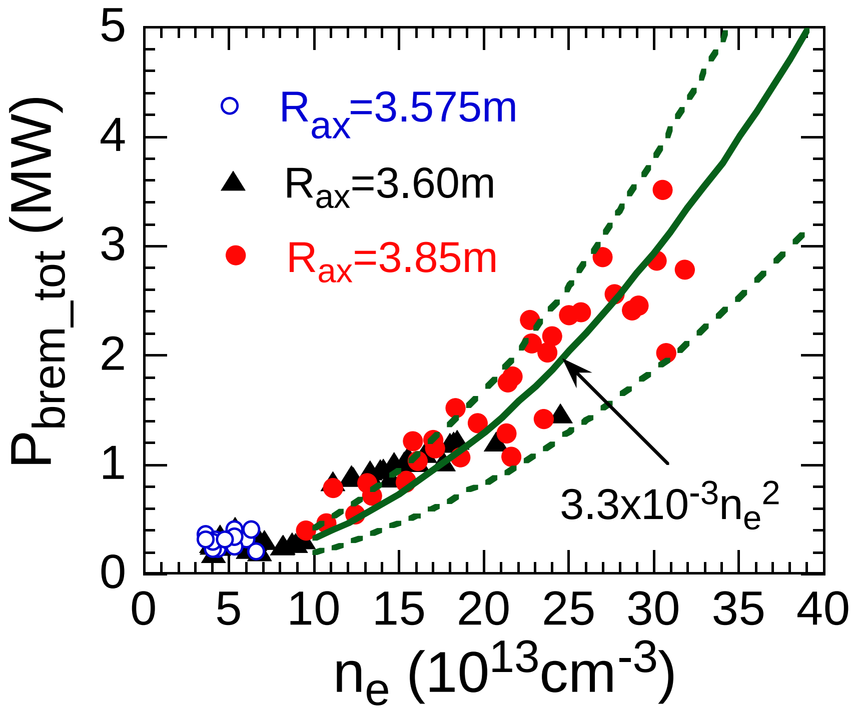

FIG. 6.5. Total bremsstrahlung radiation, $P_{brem\_tot,}$ for different magnetic axis configurations as a function of line-averaged electron density. Data at $n_e\leq10\times10^{13}cm^{-3}$ and $n_e\geq10\times10^{13}cm^{-3}$ are plotted for gas-puff and pellet discharges, respectively. Solid curve denotes result calculated with T_e=0.4 keV and Z_{eff} =1.5 and upper and lower dashed curves denotes results calculated with T_e=0.6 keV and 0.2 keV, respectively which are scaled by the square of density.

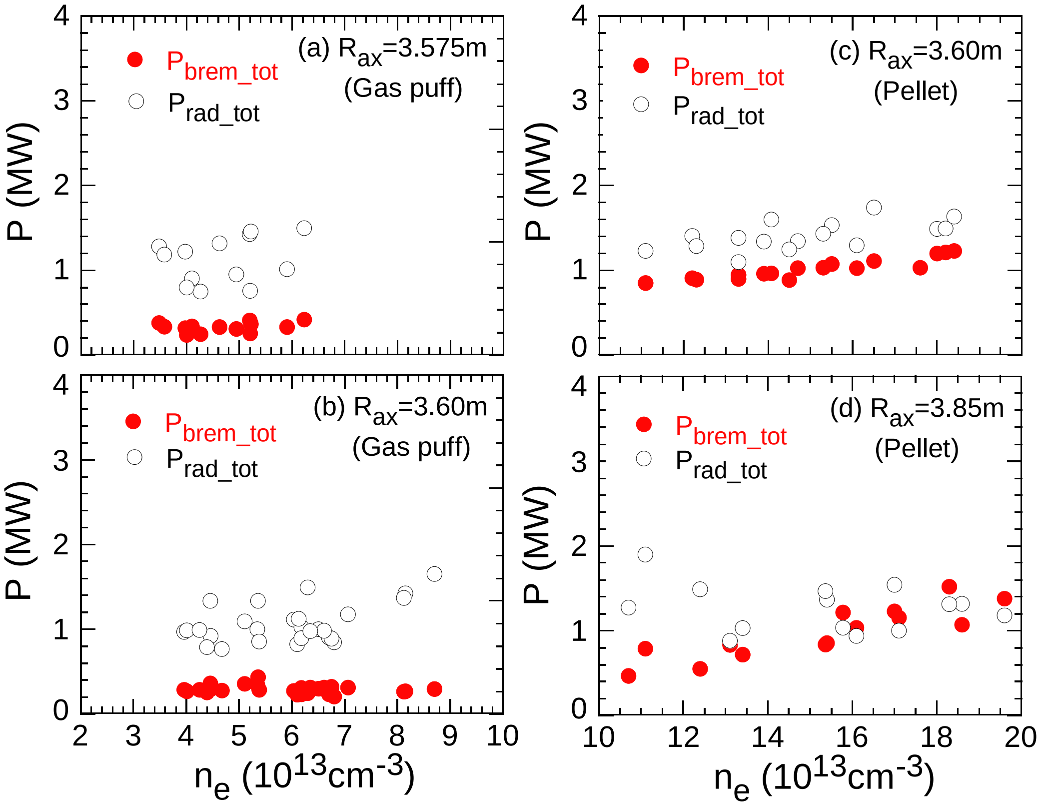

FIG. 6.6. Total radiation loss, P_{rad_tot}, and total bremsstrahlung radiation, P_{brem_tot}, as a function of line-averaged electron density in gas-puff discharges at (a) R_{ax}=3.575m and (b) R_{ax}=3.60m and in pellet discharges at (c) R_{ax}=3.60m and (d) R_{ax}=3.85m.

The total bremsstrahlung power is compared with the total radiation power, P_{rad_tot}. The results are shown in Figs. 6.6(a) and (b) as a function of averaged-electron density in the gas-puff discharges with magnetic configurations of R_{ax}=3.575m and 3.60m, respectively. The P_{rad_tot} and P_{brem_tot} are generally constant against n_e, although the P_{rad_tot} data are a little scattered due to the shot-by-shot variation. The total radiation power is considerably higher than the total bremsstrahlung power, e.g., by a factor of 5, indicating the line emission is the main component of the total radiation loss. Both of the P_{rad_tot} and P_{brem_tot} seem to have less dependence on the magnetic axis position. The comparison is also made for the pellet discharges, as seen in Figs. 6.6(c) and (d). The result is entirely different from the gas-puff discharge case. The amount of the total bremsstrahlung radiation is very close to the total radiation, suggesting the bremsstrahlung radiation fully dominates the total radiation in the high-density operation with H_2 pellets. We also clearly find a large reduction of the line radiation in the pellet discharge, when Fig. 6.6(c) is compared with Fig. 6.6(b). The reduced particle recycling in the pellet discharge is probably the reason why the line radiation quickly decreases in the pellet discharge. When the plasma magnetic axis is shifted outwardly, we notice the P_{brem_tot} is entirely the same as the P_{rad_tot}, as plotted in Fig. 6.6(d). The impurity screen [17] becomes effective for the outwardly shifted configuration such as R_{ax}=3.85m at which the ergodic layer is thicker.

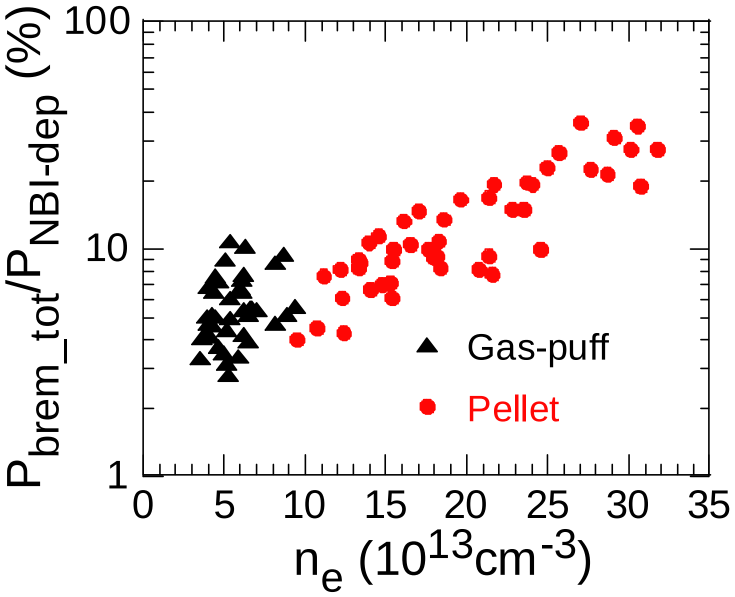

FIG. 6.7. Ratio of total bremsstrahlung radiation, P_{brem_tot}, to NBI birth deposition power, $P_{NBI\text{-}dep}$, as a function of line-averaged electron density (solid triangles: gas-puff discharges, solid circles: pellet discharges). All data from R_{ax}=3.575m, 3.60m and 3.85m are plotted in the figure.

In order to check a simple power balance, the total bremsstrahlung radiation is compared with the NBI deposition power as a function of the line-averaged electron density, as shown in Fig. 6.7. The ratio of the total bremsstrahlung power to the NBI deposition power, $P_{brem\_tot}/P_{NBI\text{-}dep}$, increases with n_e in the pellet discharge, whereas it does not change against the density in the gas-puff discharge keeping the values smaller than 10%. The peak value of the ratio reaches 35% at $n_e=3\times10^{14}cm^{-3}$ for pellet discharges.

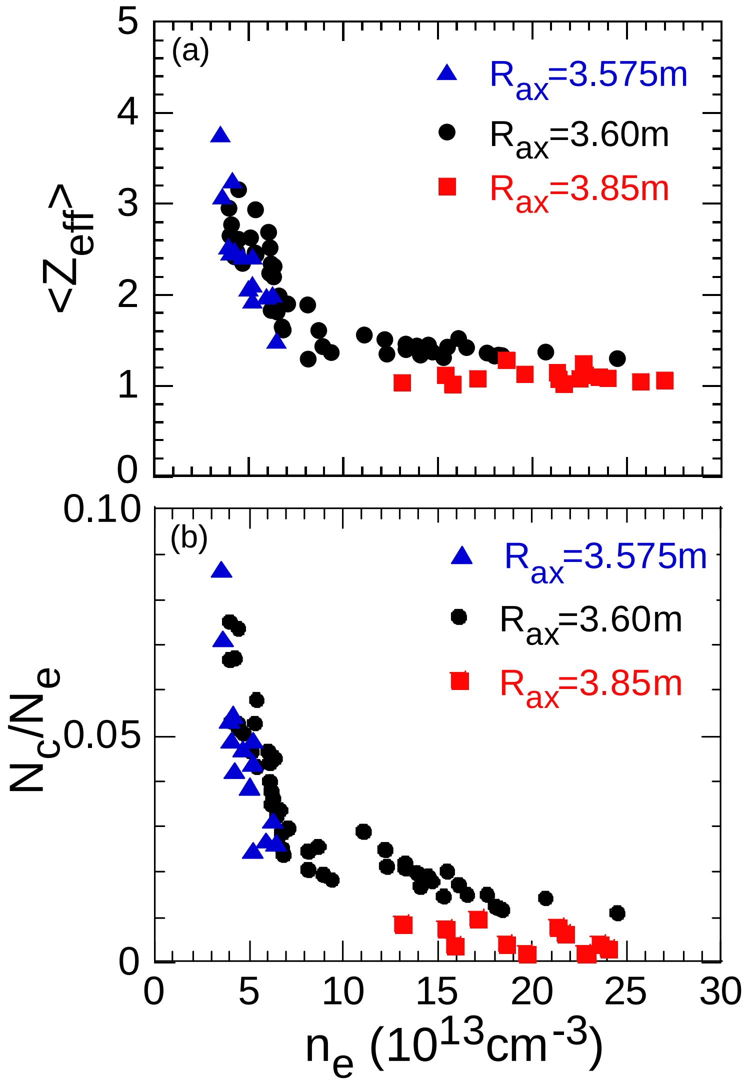

FIG. 6.8. (a) Line-averaged effective ion charge, $\langle Z_{eff} \rangle$, and (b) ratio of total number of carbon ions, N_c, to total number of electrons, N_e, as a function of line-averaged electron density for different magnetic configurations. Data at $n_e \le 10\times10^{13}cm^{-3}$ and $n_e \ge 10\times10^{13}cm^{-3}$ are plotted for gas-puff and pellet discharges, respectively.

6.4.3 Behavior of Z_{eff}

Behavior of Z_{eff} values is investigated in both of the gas-puff and pellet discharges. Here, we define the line-averaged Z_{eff} as $<Z_{eff}>$ as well as the line-averaged density in order to study the global behavior. The line-averaged Z_{eff} gives a very similar value to the central Z_{eff}, since the Z_{eff} profile is usually flat as mentioned later. The results are summarized for three different magnetic axis positions in Fig. 6.8(a) as a function of line-averaged electron density. All the data behave similarly to the density. The line-averaged Z_{eff} quickly decreases from 3.8 to 1.4 as the line-averaged density increases from 3 to $9\times10^{13}cm^{-3}$ in the gas-puff density regime. In the pellet density regime ($1\leq n_e\leq3\times10^{14}cm^{-3}$), however, it roughly keeps constant against the density, although the gradual reduction is seen in R_{ax}=3.60m case.

In LHD the impurity is fully dominated by carbon and other impurities such as oxygen and iron entirely have less amount. Then, the carbon density is easily calculated from the Z_{eff} value when the impurity density is only replaced by the carbon density. The origin of the carbon is divertor plates on which the magnetic field lines are finally touched through the divertor legs. The carbon is fully ionized in the plasma core. Total number of carbon ion, N_c, and total number of electron, N_e, are derived by integrating carbon ion density and electron density against the plasma volume, respectively. Figure 6.8(b) shows the ratio of the total number of carbon to the total number of electron, N_c/N_e, as a function of line-averaged density for different magnetic axis configurations. The ratio decreases by a factor of 4 as the density increases in the gas-puff discharges and reaches 2% at $n_e=7\times10^{13}cm^{-3}$. Magnetic axis dependence is not observed, at least between R_{ax}=3.575m and 3.60m which are the inwardly shifted configurations. The ratio changes a little in range of 2-3% for R_{ax}=3.60m configuration in the pellet discharges, whereas the density largely changes from 0.7 to $2.5\times10^{14}cm^{-3}$. However, the ratio is clearly reduced when the magnetic axis moves to R_{ax}=3.85m and it distributes at ranges less than 1%. It also indicates that the impurity screen is enhanced in the outwardly shifted configuration.

On the other hand, radial Z_{eff} profiles are analyzed for the gas-puff and pellet discharges. Typical profiles are plotted for different magnetic axis configurations in Fig. 6.9. The profiles show a fairly flat one for all the configurations. In LHD such a flat Z_{eff} profile [18] has been usually observed in most of discharges. This indicates the carbon percentage is radially constant to the electron density, suggesting the impurity partial pressure is radially constant to the electron pressure or to the bulk ion pressure. Pure hydrogen plasmas closed to Z_{eff}=1 are maintained at high-density regime in the pellet discharges, at least just after injection of H_2 pellets.

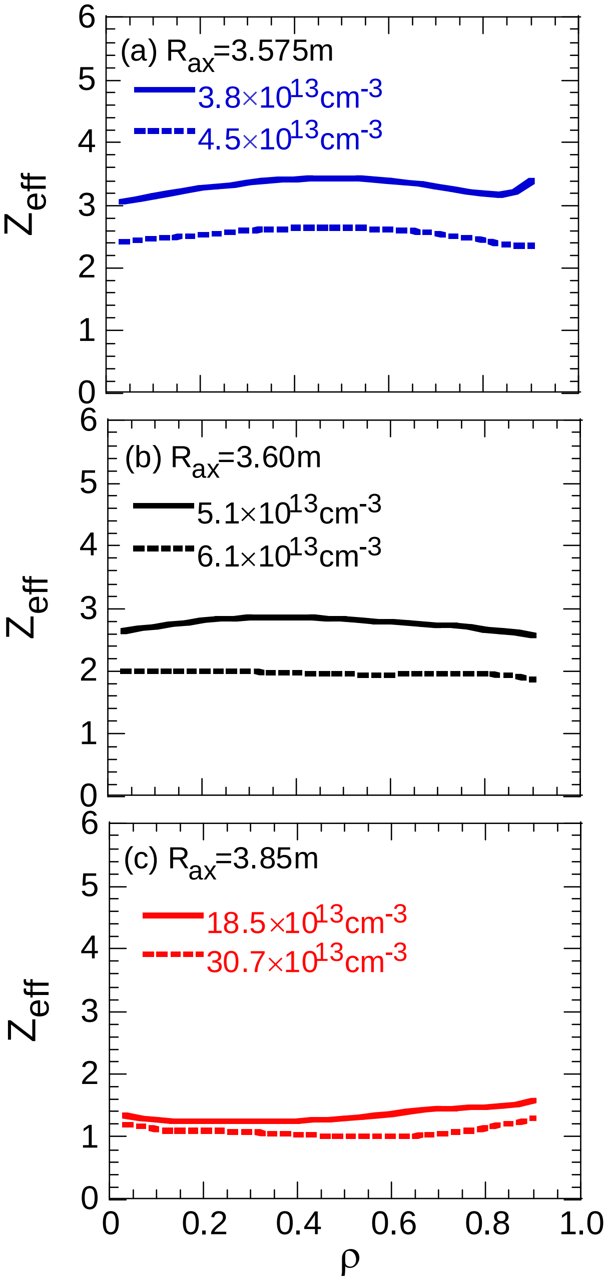

FIG. 6.9. Radial Z_{eff} profiles for discharges with different densities in (a) R_{ax}=3.575m (gas puff), (b) R_{ax}=3.60m (gas puff) and (c) R_{ax}=3.85m (pellet) as a function of normalized radius.

6.4.4 Bremsstrahlung radiation from ergodic layer

The visible bremsstrahlung radiation localized in the edge ergodic layer ($1.0<\rho\leq 1.3$) is analyzed as a parameter of wavelength in the gas-puff discharge. The bremsstrahlung emissivity profile is calculated at different wavelengths based on the visible bremsstrahlung emissivity profile and electron temperature profile. Since the edge electron temperature is only measured in $\rho\leq1.05$, the outside profile between $\rho=1.05$ and 1.30 is determined by extrapolating the measured profile. The result is shown in Figs. 6.10(a)-(d) for different wavelengths of 530, 50, 10 and 1nm, respectively. The hatched region at $1.0\leq\rho\leq1.3$ indicates the ergodic layer. It is clearly understood that the edge boundary of the bremsstrahlung emission moves to the inside of the ergodic layer as a function of the wavelength. The bremsstrahlung radiation per nm at 1nm from the plasma center is almost five orders of magnitude larger than that at 530nm. Here, it should be noticed here that the energy interval also increases in two and half orders of magnitude (1240eV (1nm) /2.34eV (530nm) =530). The bremsstrahlung radiation from the ergodic layer is negligible in the total radiation power. The calculation of the total bremsstrahlung radiation within $\rho\leq1.05$ gives the accurate result.

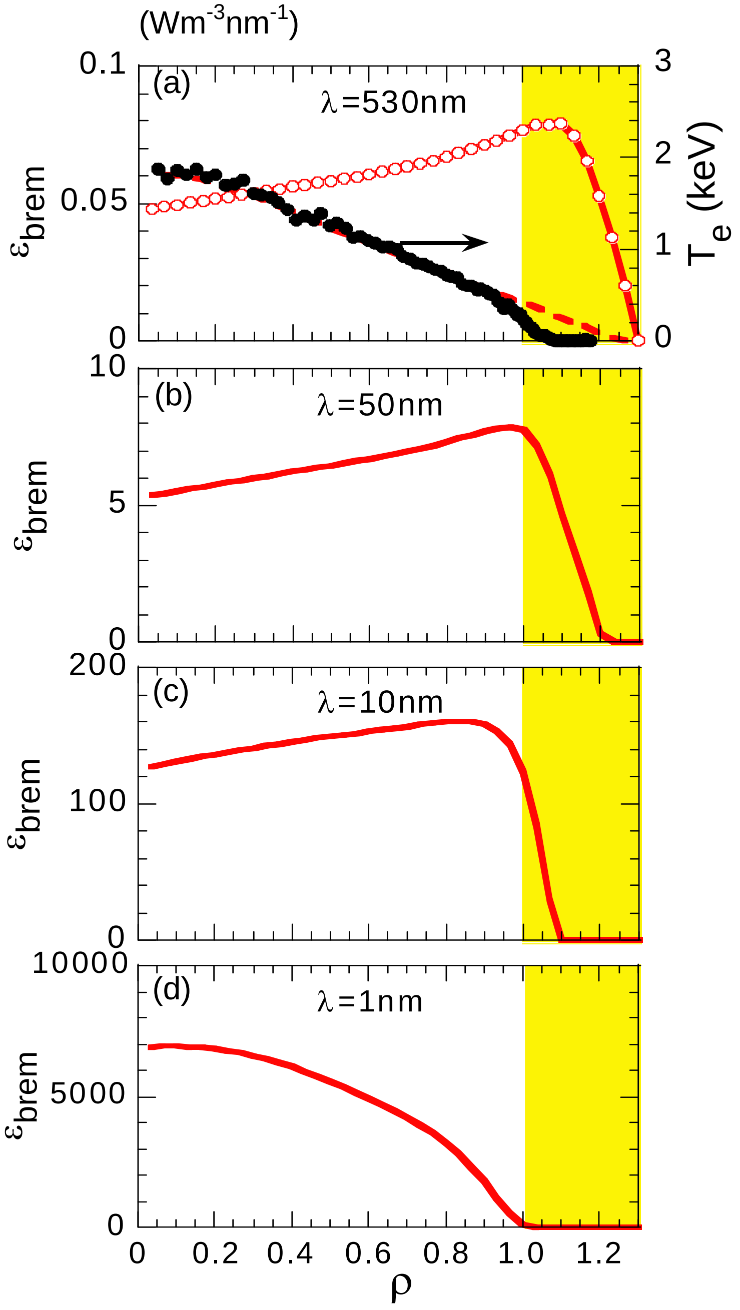

FIG. 6.10. Radial profiles of local bremsstrahlung emissivity at wavelengths of (a) 530nm, (b) 50nm, (c) 10nm and (d) 1nm as a function of normalized radius. Electron temperature profile is plotted with solid circles in (a). Dashed line denotes edge temperature profile extrapolated from experimental data. Hatched area indicates ergodic layer (1.0< ρ≤1.3).

6.5 Summary

The bremsstrahlung intensity profiles have been measured at visible wavelength range of 530-540nm. The total bremsstrahlung radiation are investigated in the middle-density discharges ($3 \leq n_e \leq 9 \times 10^{13}cm^{-3}$) with gas puffing and high-density discharges ($10 \leq n_e \leq 30 \times 10^{13}cm^{-3}$) with H_2 multi-pellets. The total bremsstrahlung radiation is dominated by the EUV (1-50nm) range, in particular, for pellet discharges. The peak position of the bremsstrahlung radiation profile per unit normalized radius is located at $\rho=0.75$ for the gas-puff discharge and at $\rho=0.48$ for the pellet discharge. The total bremsstrahlung radiation quickly increases with the density in the pellet discharges, whereas it is almost constant with the density in the gas-puff discharges. The total bremsstrahlung radiation is compared with the total radiation loss. As a result, it is found that the line emissions are the main component of the total radiation loss in the gas-puff discharges and the total radiation loss is fully dominated by the bremsstrahlung radiation in the pellet discharges instead of the line radiation. The total bremsstrahlung radiation increased with the density reaches 35% of the total deposition power of NBI in the pellet discharges, while it is less than 10% in the gas-puff discharges not depending on the density.

References

[1] M. A. Mahdavi, T.H. Osborne, A. W. Leonard et al., Nucl. Fusion, 2002. **42**: p. 52.

[2] J. Stober, O. Gruber, M. Kaufmann et al., Plasma Phys. Control. Fusion 2002. **44**: p. A159.

[3] D. Post, J. Abdallah, R. E. H. Clark et al., Phys. Plasmas, 1995. **2**: p. 2328.

[4] G. Becker, Nucl. Fusion, 1999. **39**: p. 937.

[5] R. Parker, G. Janeschitz, H. D. Pacher et al., J. Nucl. Mater, 1997. **241-243**: p. 1.

[6] H. Kubo, S. Sakurai, N. Asakura et al., Nucl. Fusion, 2001. **41**: p. 227.

[7] O. Gruber, A. Kallenbach, M. Kaufmann et al., Phys. Rev. Lett. , 1995. **74**: p. 4217.

[8] R. R. Weynants, A.M. Messiaen, J. Ongena et al., Nucl. Fusion, 1999. **39**: p. 1637.

[9] H.Yamazaki, S. Morita, M. Goto et al., Fusion Engineering and Design, 2006. **81**: p. 2817.

[10] R. Sakamoto, M. Kobayashi, J. Miyazawa et al., Nucl. Fusion, 2009. **49**: p. 085002.

[11] M. Greenwald, J. Terry, S. Wolfe et al., Nucl. Fusion, 1988. **28**: p. 2199.

[12] H. Y. Zhou, S. Morita, M. Goto and M. B. Chowdhuri, Rev. Sci. Instrum., 2008. **79**: p. 10F536.

[13] H. Nozato, S. Morita, and M. Goto, J. Plasma Fusion Res. SERIES, 2006. **7**: p. 14.

[14] H. Y. Zhou, S. Morita, M. Goto and C. F. Dong, J. Appl. Phys., 2010. **107**: p. 053306.

[15] K. Narihara, I. Yamada, H. Hayashi et al., Rev. Sci. Instrum., 2001. **72**: p. 1122.

[16] S. Morita and J. Baldzuhn, IPP-report III/199 (Max-Planck-Institut für Plasmaphysik, Garching , Germany, 1994).

[17] M. B. Chowdhuri, S. Morita and M. Kobayashi et al., Phys. Plasmas, 2009. **16**: p. 062502.

[18] H. Y. Zhou, S. Morita, M.Goto, K. Narihara and I. Yamada, Plasma Fusion Res., 2010. **2**: p. S1033.

Chapter 7

Alternative approach to Z_{eff} diagnostics

7.1 Introduction

One of critical issues in fusion research is the impurity contamination, which leads to fuel dilution and substantial fusion power loss through the bremsstrahlung and line radiation. Effective ion charge, Z_{eff}, is a useful parameter to characterize the impurity content in the fusion plasmas. When the spatial distribution is measured, it can easily express the radial transport of impurities. Therefore, the values of Z_{eff} have been measured in many fusion devices. The Z_{eff} is usually derived from the visible bremsstrahlung continuum measured with an interference filter [1-3] or a visible spectrometer [4-6], of which the sensitivity has to be absolutely calibrated *in situ*. In Large Helical Device (LHD), the interference filter coupled with photomultipliers [7] was first adopted for measuring a wavelength interval of 6.2nm at a central wavelength of 536.6nm. However, this diagnostic method could not clearly eliminate the contamination of line emissions existing in the vicinity of the wavelength. In order to solve this problem, a Czerny-Turner-Type visible spectrometer [8] was developed with a 300 grooves/mm grating (blaze: 500nm) and the visible bremsstrahlung continuum has been measured at the wavelength interval of 530-540nm. The influence of the line emissions could be perfectly removed, but the problem still remained in the intensity profile of the visible bremsstrahlung continuum. Finally, it became identified that the profile is deformed by nonuniform bremsstrahlung emission originating in the edge boundary of the thick ergodic layer surrounding the main plasma, which consists of stochastic magnetic field lines in LHD. Although the Z_{eff} profile measurement was difficult in a significant number of discharges, it was possible only in a few limited discharge conditions with inwardly shifted magnetic-axis configurations (R_{ax}≤3.60m), in which the volume of the ergodic layer is relatively small. The thickness of the ergodic layer quickly increases when the plasma axis is outwardly shifted. Thus, it was experimentally confirmed that the nonuniform visible bremsstrahlung emission from the ergodic layer is extremely enhanced in the outwardly shifted configurations (R_{ax}>3.60m).

On the other hand, it is expected that the bremsstrahlung continuum emission from the ergodic layer with low-temperature and high-density plasmas disappears at higher photon energy or shorter wavelength, e.g., 100eV (12.4nm). For the purpose, a space-resolved flat-field extreme ultraviolet (EUV) spectrometer [9] was adopted to measure the bremsstrahlung continuum in the EUV wavelength range (6-40nm). The Z_{eff} measurement is also possible in lower densities ($n_e \leq 2.0\times10^{13}\mathrm{cm}^{-3}$), because the bremsstrahlung continuum intensity rapidly increases in high-temperature toroidal plasmas when the wavelength is shorter. In this chapter, the Z_{eff} profile diagnostic in the EUV range is presented for the first time and the results are compared with the Z_{eff} measurement using the visible bremsstrahlung.

7.2 EUV spectrometer for bremsstrahlung profile measurement

The EUV bremsstrahlung profile is measured by the space-resolved flat-field EUV spectrometer system. The EUV spectrometer system is equipped with an entrance slit, a spatial resolution slit, a holographic laminar-type varied-line-space (VLS) grating (1200 grooves/mm) and a charge-coupled device (CCD). The entrance slit width of 100 μm and the spatial resolution slit of 0.5 mm are usually used for the experiment. The grating has effective area of 26 mm (groove length) × 46 mm (groove distance) with curvature radius of 5606 mm. The EUV spectrometer is set perpendicular to the toroidal magnetic field of LHD. The upper half of the elliptical plasma can be observed with the EUV spectrometer, as illustrated in FIG. 7.1(a). The vertical range for the profile measurement varies from 51.7 cm to 52.8 cm when the wavelength is changed from 6 nm to 40 nm.

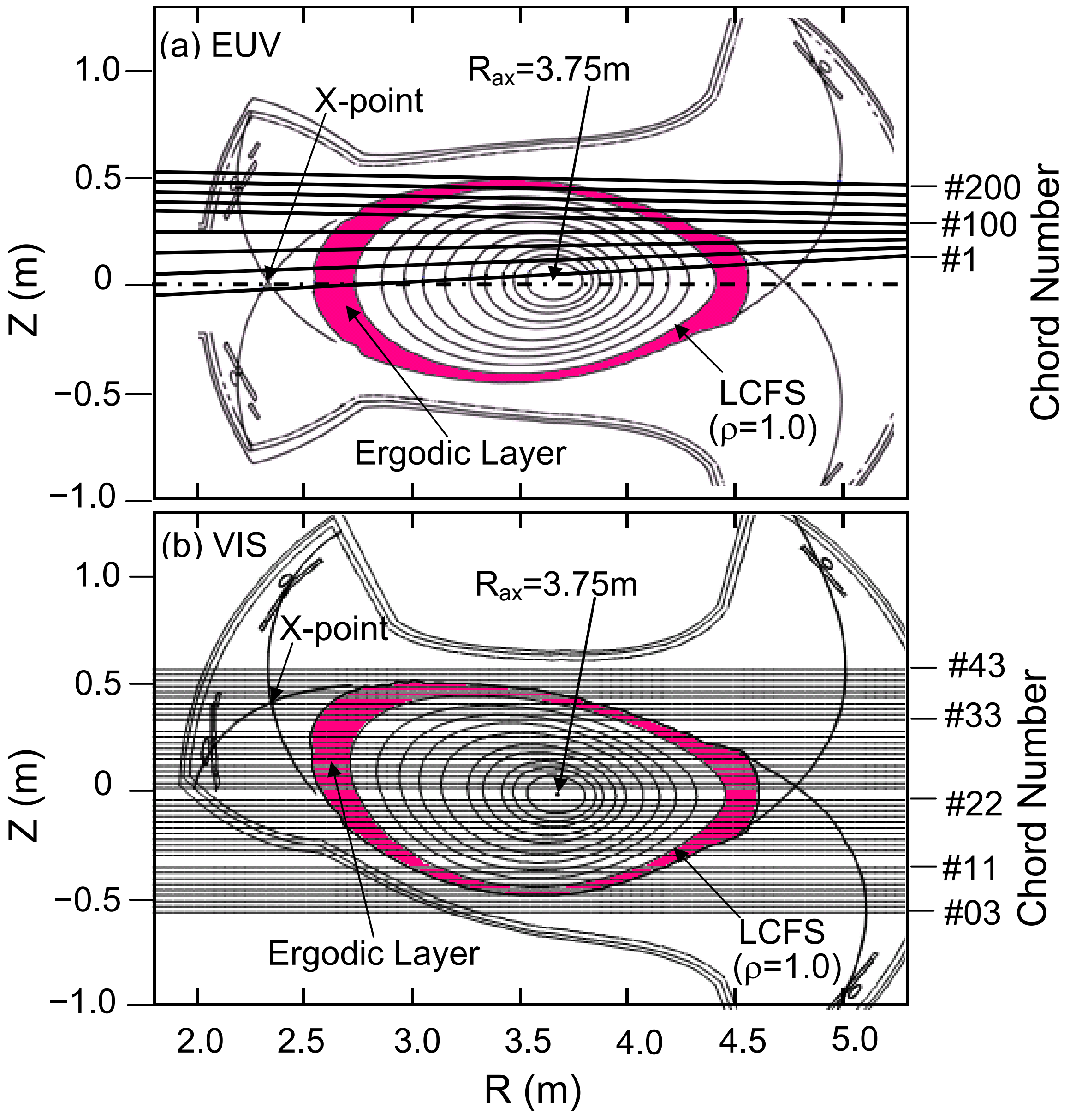

FIG. 7.1. Arrangement of view chords at horizontally elongated plasma cross section in R_{ax}=3.75m for (a) EUV spectrometer and (b) visible spectrometer. Ten magnetic surfaces are shown with the boundary denoted by LCFS and ergodic layer is shown with hatched area at ρ≥1.0.

The vertical profile can be also measured at different toroidal positions by scanning the toroidal angle of the EUV spectrometer. The vacuum pressure of the spectrometer evacuated by magnetically floating turbo-molecular pump is maintained at 1×10^{-8} torr. The CCD detector (Andor DO420-BN) with a sensitive area of 26.6×6.6 mm^2 (1024×255 pixels, 26×26 μm^2/pixel) is usually operated at -20°C to provide a sufficient signal-to-noise ratio. The vertical profile is recoded along the CCD long side of 26.6mm. Every 5 pixels are summed up in the binning operation mode of the CCD. The wavelength dispersion is obtained along the short side of 6.6mm with the same binning mode. The total data points are then 204 (=1024/5: vertical profile) × 51 (=255/5: wavelength) channels in a single frame. The profile can be observed with sampling time of 200 ms observation in the present binning condition. The measured wavelength can be externally controlled by moving the CCD position in the range of 6-40 nm.

The visible bremsstrahlung profile is measured by the astigmatism-corrected Czerny-Turner-Type visible spectrometer. A 44-fibers array and a CCD (Andor SOLIS-DU934N) are attached to the spectrometer. The vertical profile is also observed with the 44-fibers array, as shown in FIG. 7.1(b). The view angle of the fiber array is tilted by an angle of 6° from the perpendicular direction to the toroidal magnetic field. Therefore, the poloidal cross section for the radial profile measurement is slightly distorted compared to the EUV case. The spatial resolution of 30 mm is defined by the lens coupled with the fiber. The visible spectrometer consists of a removable entrance slit, four mirrors and three gratings. The relatively small focal length of 300 mm permits a wide wavelength observation range with the use of 300 grooves/mm grating. The wavelength of 450-600 nm is usually measured at central wavelength of 530 nm. The CCD size is 13.3×13.3 mm^2 with 1024×1024 pixels. The profile data are acquired in each 100ms with exposure time of 31ms. The visible spectrometer system is absolutely calibrated with an integrating sphere and the EUV spectrometer is calibrated through the EUV bremsstrahlung continuum [10] compared with the visible bremsstrahlung emission.

7.3 Comparison between visible and EUV bremsstrahlung profiles

7.3.1 Visible and EUV spectra

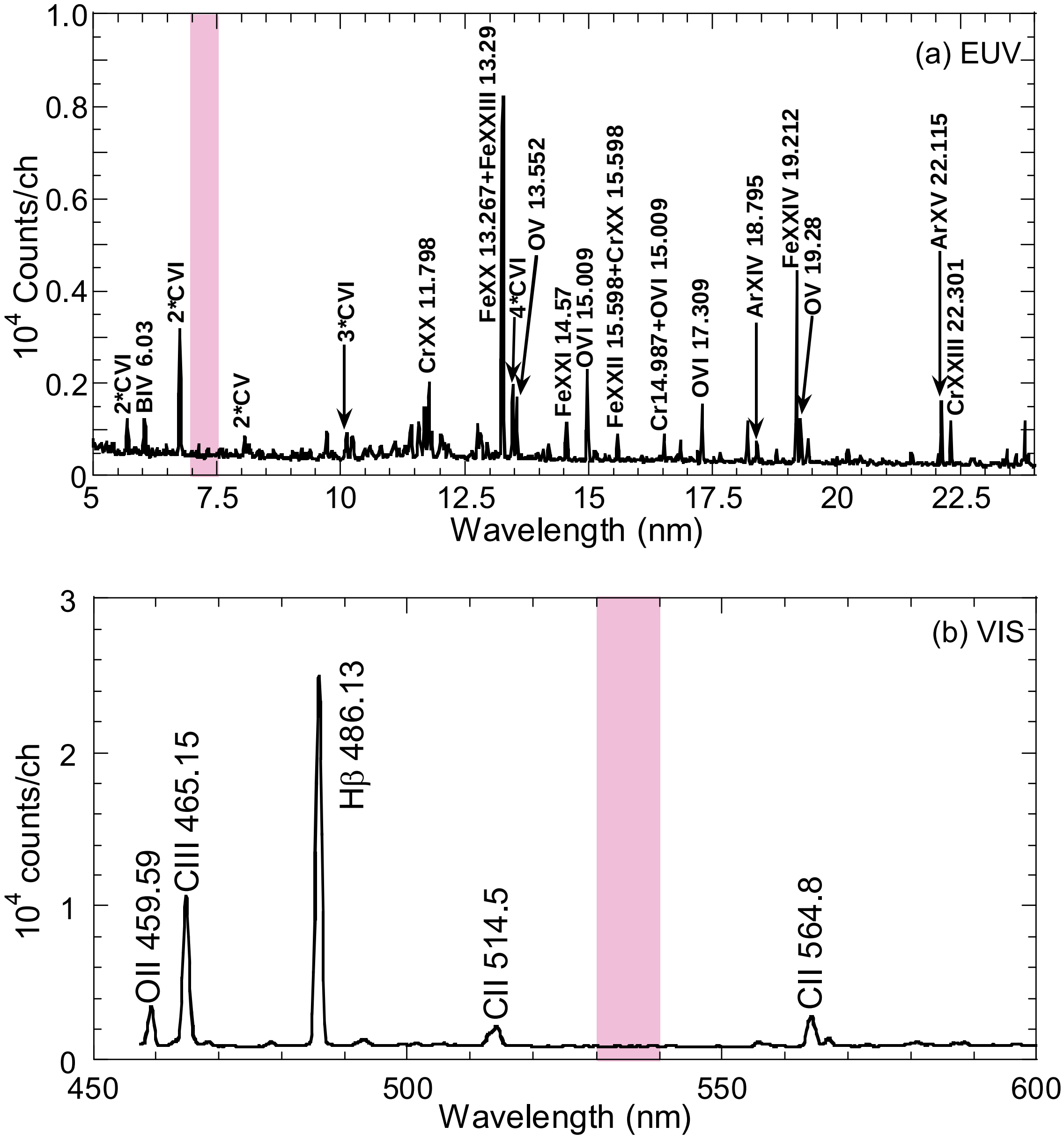

FIG. 7.2. (a) EUV spectrum at 5-24 nm and (b) visible spectrum at 450-600 nm. Hatched regions denote wavelength interval for bremsstrahlung continuum measurement.

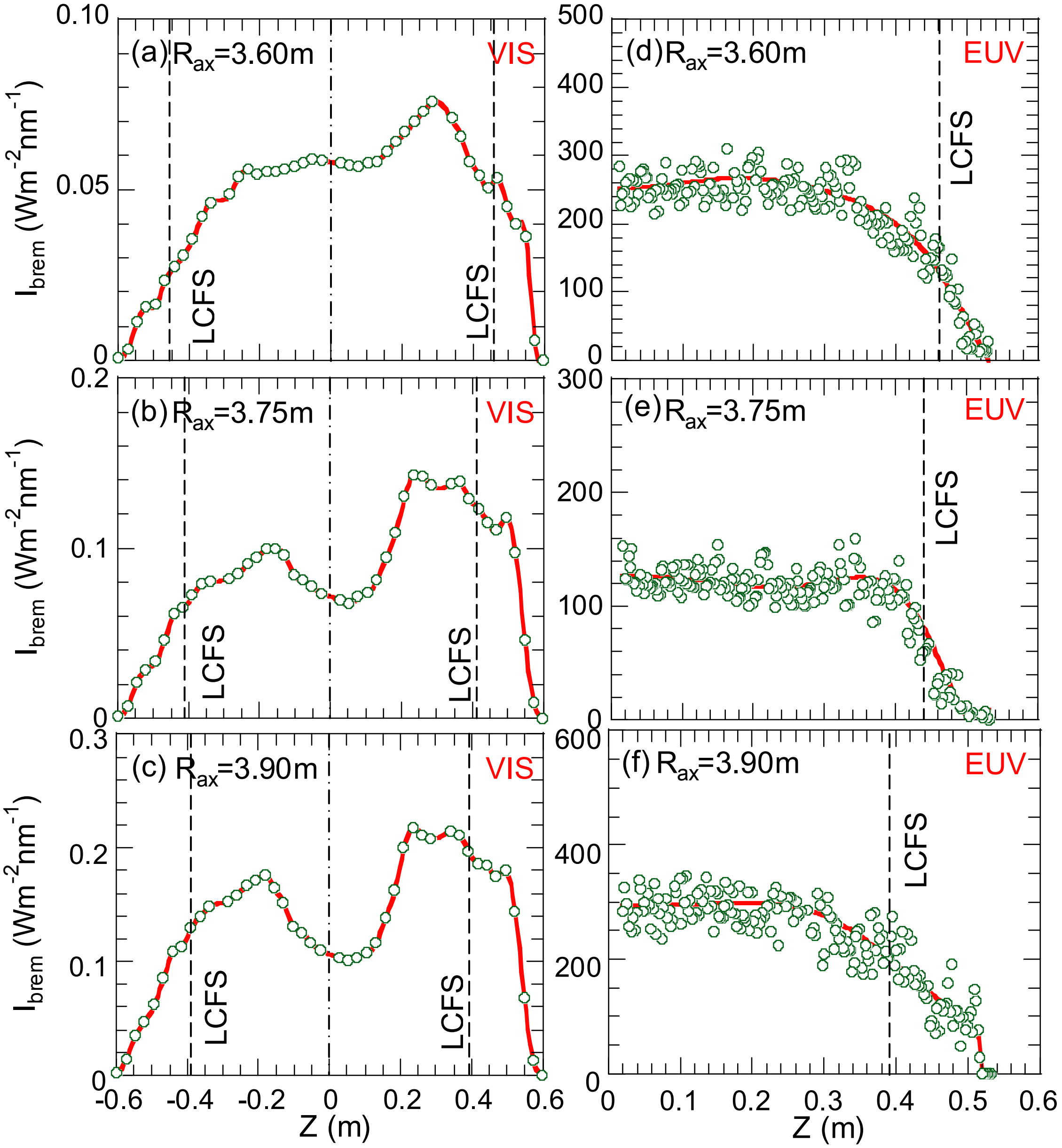

FIG. 7.3. Visible bremsstrahlung intensity profiles at (a) R_{ax}=3.60m, (b) R_{ax}=3.75m and (c) R_{ax}=3.90m and EUV bremsstrahlung intensity profiles at (d) R_{ax}=3.60m, (e) R_{ax}=3.75m and (f) R_{ax}=3.90m. Dashed and dashed-dotted lines indicate last closed flux surface (LCFS) and plasma center.

A typical example of the EUV spectrum in the wavelength range of 5-24 nm is displayed in FIG. 2(a). The shorter wavelength range of 7.0-7.5 nm with relatively high energy of 170 eV is used for the bremsstrahlung continuum measurement, as denoted by hatched area. The visible spectrum in the wavelength range of 450-600 nm is plotted in FIG. 2(b) for the comparison. The visible range of 530-540 nm, denoted by hatched region, is selected for the bremsstrahlung continuum measurement. Since the photon energy is extremely low, i.e., 2.3 eV, in the wavelength range, the visible bremsstrahlung emission has no temperature dependence.

7.3.2 Visible and EUV bremsstrahlung profiles

FIGURE 7.3 presents the comparison between EUV and visible bremsstrahlung intensity profiles measured along the view chord in three typical magnetic configurations. The position of last closed flux surface (LCFS) is denoted by dashed lines for both cases. When the magnetic axis is shifted outwardly, the low-temperature and high-density plasma in the ergodic layer quickly expands, in particular, near the X-point (see FIG. 7.1). This effect can be clearly seen in the visible bremsstrahlung profile. The profile becomes much hollow and nonuniform when the plasma axis is outwardly shifted (see FIGS. 7.3(a), (b) and (c)). On the contrary, the upper EUV bremsstrahlung intensity profile is free of the nonuniform bremsstrahlung emission for all the magnetic configurations (see FIGS. 3(d), (e) and (f)). In addition, the edge boundary of the upper EUV bremsstrahlung profile is shrunk to Z=0.52m, whereas that of the visible bremsstrahlung profile is in the vicinity of Z=0.6m. Here, it is experimentally verified that the EUV bremsstrahlung intensity profile can give a more accurate method by avoiding the nonuniform edge bremsstrahlung emission.

In the R_{ax}=3.60m configuration, the lower half of the visible bremsstrahlung profile ($-0.6\text{m} \leq Z \leq 0\text{m}$) is not disturbed by the nonuniform bremsstrahlung emission, as shown in FIG. 7.3(a). The analysis of the Z_{eff} profile is hence possible in the R_{ax}=3.60m configuration for both visible and EUV bremsstrahlung profiles.

7.4 Analysis of radial Z_{eff} profile from EUV bremsstrahlung

The radial bremsstrahlung emissivity profile is derived from the measured intensity profile based on the Abel inversion method, in which the magnetic surface distortion caused by β-effect is taken into account [11]. The magnetic surface structures with finite β-effect are calculated by the three-dimensional equilibrium code, VMEC [12]. The radial Z_{eff} profile can be thus analyzed from the bremsstrahlung emissivity profile by considering the electron density and temperature profiles measured by Thomson scattering diagnostics [13].

The Z_{eff} profile analyzed from EUV bremsstrahlung profile is compared with that from the visible bremsstrahlung profile, as shown in FIG. 7.4. The both profiles are obtained in the R_{ax}=3.6m configuration with the thinnest ergodic layer. The density profile is slightly hollow, which is a typical character of helical plasmas, and the edge density decreases to zero at ρ=1.1, as seen in FIG. 7.4(a). The peaked temperature profile shows the central value of 2 keV, as plotted in FIG. 7.4(b). The bremsstrahlung emissivity profiles are also hollow reflecting the density profile, as plotted in FIG. 7.4(c), since the bremsstrahlung emission increases with the square of the density. It is clear from the figure that the edge bremsstrahlung emission begins to increase at different radial positions, i.e., ρ=1.2 for the EUV bremsstrahlung and ρ=1.3 for the visible bremsstrahlung. The difference is caused by the energy dependence of the bremsstrahlung emission, i.e., 170eV for the EUV bremsstrahlung and 2.3eV for the visible bremsstrahlung. Furthermore, it is experimentally confirmed that the EUV bremsstrahlung emissivity is four orders of magnitude stronger than the visible emissivity. Seeing FIGS. 7.4(a) and (c), we notice that there is a small difference in the edge boundary between the bremsstrahlung and density profiles. The present Thomson system is not applicable in the extremely low temperature range of $T_e \leq \sim$20eV. Therefore, the density measurement becomes also difficult in this temperature range.

The Z_{eff} profiles analyzed from the EUV and visible bremsstrahlung emissivity are shown in FIGS. 7.4(d) and (e), respectively. Both results have the flat profile inside ρ=0.7 with entirely similar values of Z_{eff}=3, although a little discrepancy is appeared in ρ>0.7. The error bars seen in the Z_{eff} profiles are due to uncertainties in the electron density profile as well as the temperature profile. Therefore, the Z_{eff} measurement using the EUV bremsstrahlung emission brings a little larger error at outer region of the plasma, because the temperature dependence of the EUV bremsstrahlung becomes large in such a low temperature range. The Z_{eff} analysis in the ergodic layer is difficult because of the increased uncertainty of the Thomson data and the absence of the reliable magnetic surface.

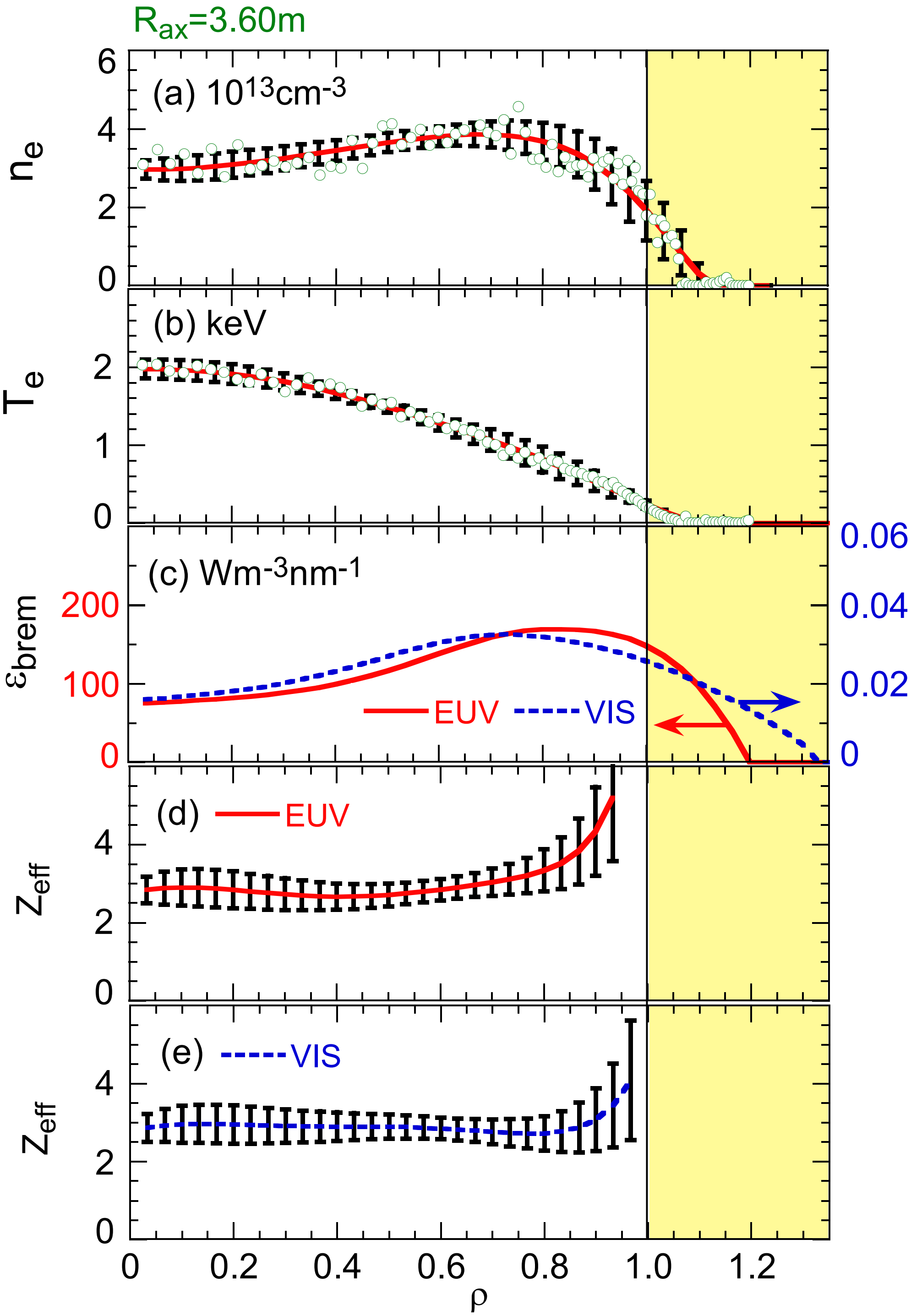

FIG. 7.4. Radial profiles of (a) electron density, (b) electron temperature, (c) bremsstrahlung continuum emissivity (solid: EUV, dashed: visible), (d) effective ion charge from EUV bremsstrahlung and (e) effective ion charge from visible bremsstrahlung. Hatched region denotes ergodic layer.

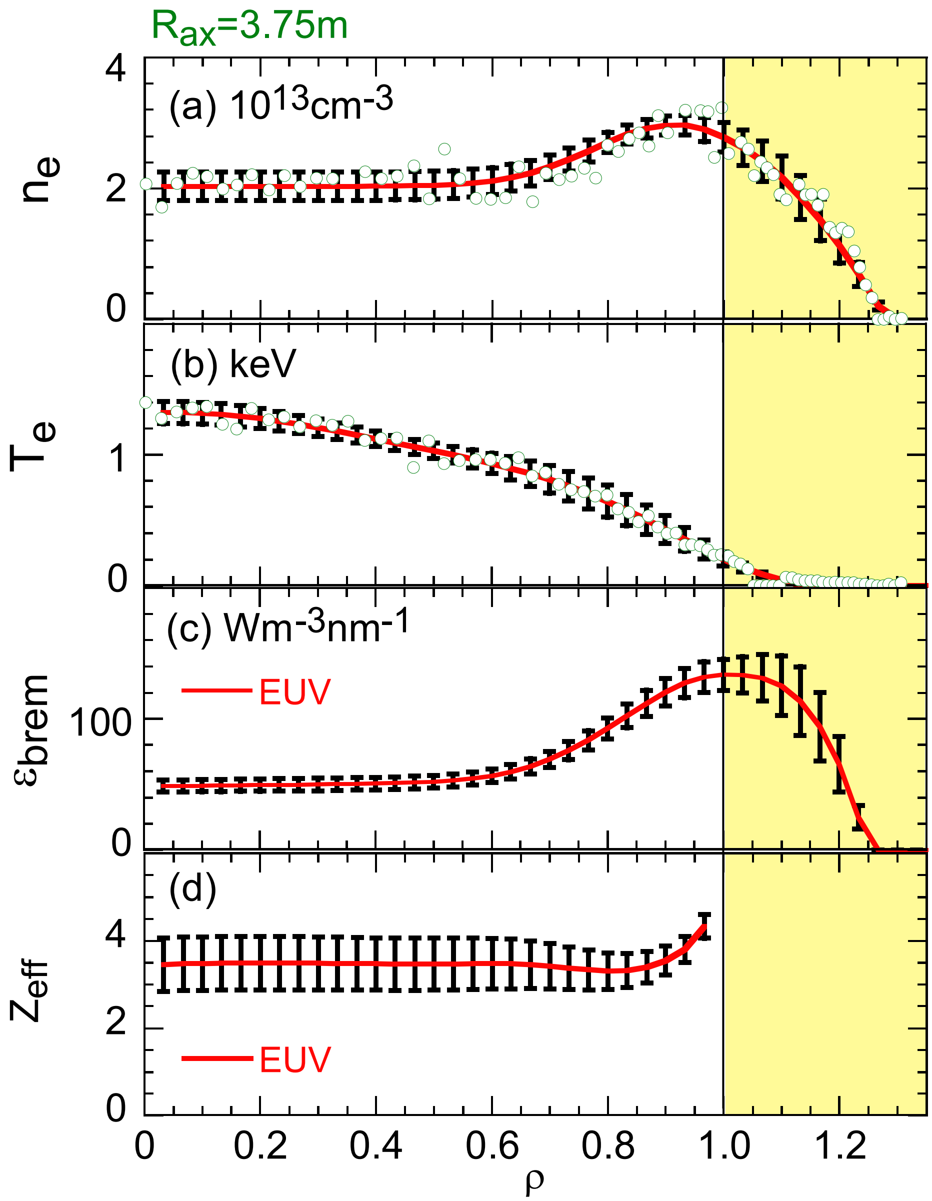

FIG. 7.5. Radial profiles of (a) electron density, (b) electron temperature, (c) EUV bremsstrahlung continuum emissivity and (d) effective ion charge from EUV bremsstrahlung. Hatched region denotes ergodic layer.

The Z_{eff} profile is studied with the EUV bremsstrahlung continuum for the outwardly shifted plasma axis positions of R_{ax}=3.75m, in which the Z_{eff} analysis using the visible bremsstrahlung was difficult (see FIG.7.3). A typical result is shown in FIG. 7.5. The density profile is more hollow than that in R_{ax}=3.60m, whereas the electron temperature profiles are similar in both plasma axes. Reflecting the hollow density profile, the EUV bremsstrahlung emissivity profile becomes extremely hollow, as seen in FIG. 7.5(c). The Z_{eff} profile analyzed from the EUV emissivity profile is shown in FIG. 7.5(d). The result also indicates a fairly flat Z_{eff} profile as well as the case of R_{ax}=3.6m. The error of the analyzed Z_{eff} value estimated from the three profiles of n_e, T_e and ε_{brem} is to be ±14%. Furthermore, it is pointed out as the advantage of the EUV bremsstrahlung continuum measurement that the Z_{eff} profile analysis becomes possible at lower density ranges such as $n_e=2.0 \times 10^{13}cm^{-3}$. The Z_{eff} profile analysis for even lower density is also promised, if several different wavelength intervals in the EUV bremsstrahlung continuum are summed up.

7.5 Summary

Radial profile measurement of Z_{eff} using visible bremsstrahlung (530nm) in the Large Helical Device (LHD) has often encountered difficulties because the intensity profile was largely deformed by the nonuniform visible bremsstrahlung emissions from the edge ergodic layer surrounding the core plasma. A space-resolved flat-field extreme ultraviolet (EUV) spectrometer has been newly adopted to measure the Z_{eff} profile using the EUV bremsstrahlung continuum in the wavelength range of 7.0-7.5nm. The EUV bremsstrahlung intensity profiles have been measured and checked for all the magnetic configurations with totally different magnetic field structures in the ergodic layer of LHD. It is found that the nonuniform bremsstrahlung emission from the thick ergodic layer can be entirely eliminated by use of the EUV emission with relatively high photon energy of 170eV. As a result, the Z_{eff} profile can be successfully measured for most of discharges regardless of magnetic field structures of the ergodic layer. The Z_{eff} profiles measured in the EUV range are compared with those measured in the visible range at a magnetic configuration with the thinnest ergodic layer thickness. The result verifies that the use of the EUV bremsstrahlung continuum is an alternative way for the Z_{eff} measurement in toroidal plasmas with nonuniform bremsstrahlung emissions at the edge. Typical results from the EUV bremsstrahlung measurement are presented showing a fairly flat Z_{eff} profile with error bars of ±14%.

References

[1] M. E. Foord, E. S. Marmar and J. L. Terry, Rev Sci Instrum, 1982. **53**(9): p. 1407.

[2] G. Verdoolaege, G. Telesca, E. Delabie et al., Rev. Sci. Instrum., 2006. **77**: p. 10F310.

[3] B. Schunke, G. T. A. Huysmans and P. R. Thomas, Rev. Sci. Instrum., 2005. **76**: p. 083501.

[4] K. Kadota, M. Otsuka and J. Fujita, Nucl. Fusion, 1980. **20**(2): p. 209.

[5] H. Meister, R. Dux, L. D. Horton et al., Rev. Sci. Instrum., 2003. **74**: p. 4625.

[6] M. Krychowiak, R. König, T. Klinger and R. Fischer, J. Appl. Phys., 2004. **96**: p. 4784.

[7] H. Nozato, S. Morita, and M. Goto, J. Plasma Fusion Res. SERIES, 2002. **5**: p. 442.

[8] H. Y. Zhou, S. Morita, M. Goto and M. B. Chowdhuri, Rev. Sci. Instrum., 2008. **79**: p. 10F536.

[9] C. F. Dong, S. Morita, M. Goto and H. Y. Zhou, Rev Sci Instrum, 2010. **81**: p. 033107.

[10] M. B. Chowdhuri, S. Morita, M. Goto et al., Rev Sci Instrum, 2007. **78**: p. 023501.

[11] H. Y. Zhou, S. Morita, M. Goto and C. F. Dong, J. Appl. Phys., 2010. **107**: p. 053306.

[12] S. P. Hirshman, W. I. V. Rij and P. Merkel, Comput. Phys. Commum., 1986. **43**: p. 143.

[13] K. Narihara, I. Yamada, H. Hayashi et al., Rev. Sci. Instrum., 2001. **72**: p. 1122.

Chapter 8

Summary and conclusion

The effective ion charge, Z_{eff}, has been measured from visible bremsstrahlung continuum. The Z_{eff} diagnostic system using a visible spectrometer has been newly designed and constructed instead of an old interference filter system to eliminate line emissions from the signal and to measure the Z_{eff} value in low-density plasmas. An astigmatism-corrected Czerny-Turner-type visible spectrometer coupled with a charge-coupled device (CCD) has been installed in LHD to measure the visible bremsstrahlung continuum at 530nm. The system utilizes 44 optical fibers vertical array for radial profile measurement. The spectrometer is equipped with an additional toroidal mirror for further reduction of the astigmatism in addition to a flat and two spherical mirrors and three gratings (120, 300, and 1200 grooves/mm) with 30cm focal length. The circular images from all the 44 optical fibers with the core diameter of 100μm can be detected without astigmatism in the wavelength range of 200-900nm. Combination of the optical fiber with a lens (focal length: 30mm) provides spatial resolution of 30mm at the plasma center. A performance test clearly indicates an extremely good focus image of the fiber and suggests the absence of the cross-talk between adjacent fiber images. The diagnostic system has been absolutely calibrated using a standard tungsten lamp and an integrated sphere to analyze the visible bremsstrahlung continuum quantitatively.

A full vertical profile has been observed from the elliptical plasmas of LHD at horizontally elongated plasma cross section through the 44-fiber parallel array with vertical observation length of ~1m. The line emissions can be entirely eliminated by use of the visible spectrometer instead of the interference filter. However, a nonuniform bremsstrahlung emission profile, which is originated in the thick ergodic layer surrounding the main plasma, has been unfortunately observed for normal discharges ($n_e \leq 10^{14}cm^{-3}$) using H_2 gas puffing in all the magnetic configurations of LHD. After analyzing the detailed structure of the nonuniform bremsstrahlung, the lower half of the vertical bremsstrahlung emission profile is found to be free of the strong edge nonuniform bremsstrahlung emission in inwardly shifted magnetic axis configurations ($R_{ax} \leq 3.60m$). The visible bremsstrahlung intensity is checked against the density. At present, it is found that the Z_{eff} measurement is possible at low densities of $2 \leq n_e \leq 4 \times 10^{13}cm^{-3}$, whereas the density threshold was $3\text{-}4 \times 10^{13}cm^{-3}$ when the interference filter was used for the measurement. On the other hand, the nonuniform bremsstrahlung emission is vanished in extremely high-density discharges ($n_e \geq 10^{14}cm^{-3}$) maintained with solid H_2 multi-pellet injection because the plasma edge boundary at the outside of the ergodic layer is shrunk and the large poloidal nonuniformity of the plasma parameters is removed from the edge plasma. As a result, the profile analysis of the visible bremsstrahlung continuum becomes possible for all the configurations in such high-density discharges with H_2 pellets.

When the chord-integrated signal is converted into the local emissivity using Abel inversion technique, the solution is very sensitive to the distortion of the magnetic surface structure. The influence of the magnetic surface distortion based on the finite β effect is examined as the error estimation in addition to the unclear edge plasma boundary due to the presence of the ergodic layer. The analytical result indicates that the determination of the normalized minor radius for each observation chord gives a larger influence on the Abel inversion rather than the determination of the chord length. When the observed chord-integrated bremsstrahlung intensity profile is flat, the resultant uncertainty seen in the bremsstrahlung emissivity profile becomes large, in particular, at the plasma center. The Z_{eff} profile is therefore checked with density and temperature profiles, which are measured from Thomson scattering diagnostic, in order to verify the diagnostic reliability. The performance test of the present diagnostic system is quantitatively done using neutral-beam-heated discharges with H_2 and C pellet injections, where the Z_{eff} values should be principally close to 1 and 6, respectively. The result is Z_{eff}=1.2 for the H_2 pellet injection and Z_{eff}=7 for the carbon pellet injection. Taking into account intrinsic impurity ions existing in the plasmas, which are originated in the pressurized gas used for the pellet acceleration and the plasma facing components, respectively, the values evidently proves the validity of the present Z_{eff} diagnostic.

Values of the Z_{eff} quickly vary with densities in a range of $1 \le Z_{eff} \le 4$. In particular the Z_{eff} becomes large at the lower density range of $n_e \le 5 \times 10^{13} cm^{-3}$ and at inwardly shifted magnetic axis positions of $R_{ax} \le 3.60m$. In LHD the effect of impurity screening is remarkably enhanced when the density increases or the magnetic axis is shifted outwardly. This seems to be the reason for the observed Z_{eff} behavior. The Z_{eff} profiles are also analyzed for peaked, flat and hollow density profiles. A flat Z_{eff} profile is obtained for all different density profiles. The present experimental result indicates that the impurity partial pressure is radially constant to the electron or ion pressure.

Visible bremsstrahlung emission profiles have been studied over a wide range of electron densities in H_2 gas-puff and solid H_2 pellet fueled discharges. Peaked profiles are observed in high-density discharges ($n_e \ge 10^{14} cm^{-3}$) with the pellet injection, whereas hollow profiles appeared in the normal discharges ($n_e \le 10^{14} cm^{-3}$) with gas puffing. The total bremsstrahlung radiation is analyzed from the visible bremsstrahlung profile by integrating the energy and plasma volume. It is found that the total bremsstrahlung radiation quickly increases with the density in the pellet discharges, of which the increment is scaled by the square of density, while it is roughly constant against the density in the gas-puff discharges. The total bremsstrahlung radiation becomes equal to the total radiation loss in the pellet discharges. The ratio of the total bremsstrahlung radiation to the total input power only ranges in 3-10% for the gas-puff discharge. In contrast, the ratio increases with the density and reaches 30-40% for the pellet discharge. Flat Z_{eff} profiles are observed not only in the gas-puff discharges as mentioned above but also in the pellet discharges. It indicates that any impurity accumulation is not occurred in the high-density operation using the H_2 pellet injection.

On the other hand, the radial profile measurement of Z_{eff} using visible bremsstrahlung in LHD has often encountered difficulties, because the intensity profile is largely deformed by the nonuniform visible bremsstrahlung emissions from the edge ergodic layer surrounding the core plasma as mentioned above. For that purpose a space-resolved flat-field extreme ultraviolet (EUV) spectrometer has been newly adopted to measure the Z_{eff} profile using the EUV bremsstrahlung continuum in the wavelength range of 7.0-7.5nm. The EUV bremsstrahlung intensity profiles have been measured and checked for all the configurations in LHD. As a result, it is found that the nonuniform bremsstrahlung emission from the thick ergodic layer is entirely eliminated by use of the EUV emission because the EUV bremsstrahlung with such relatively high photon energy of 170eV cannot be emitted in the low-temperature region such as the outside of the ergodic layer. The Z_{eff} profile can be successfully measured for most of discharges regardless of magnetic field structures of the ergodic layer. The Z_{eff} profiles measured in the EUV range show a fairly good agreement with those measured in the visible range. The present result clearly reveals that the use of the EUV bremsstrahlung continuum is an alternative way for the Z_{eff} measurement in toroidal plasmas with nonuniform bremsstrahlung emissions at the edge. Typical results from the EUV bremsstrahlung measurement also shows a totally flat Z_{eff} profile with error bars of ±14%. The intensity of the EUV bremsstrahlung is four orders of magnitude higher than that of the visible bremsstrahlung. Therefore, it is expected that the Z_{eff} measurement based on the present alternative method becomes possible at further low-density ranges such as $1\text{-}2\times10^{13}\text{cm}^{-3}$.

In conclusion, the astigmatism-corrected Czerny-Turner-type visible spectrometer has been worked well for the bremsstrahlung continuum measurement showing good spatial resolution and high sensitivity. The Z_{eff} profiles are analyzed in neutral-beam heated plasmas for different density profiles and different density ranges after absolute calibration of the spectrometer. The flat Z_{eff} profile is observed for all different density profiles and different density ranges. It indicates that the impurity partial pressure is radially constant. The total bremsstrahlung radiation becomes equal to the total radiation loss in high-density operation with H_2 multi-pellets. The Z_{eff} measurement based on the EUV bremsstrahlung continuum is newly demonstrated as the alternative approach to eliminate the nonuniform bremsstrahlung emission from the ergodic layer.

Acknowledgements

The doctoral thesis is completed through three-year study on the impurity behavior in fusion plasmas of Large Helical Device (LHD) at National Institute for Fusion Science (NIFS), Toki, Japan. Here, I would like to thank all the persons who have kindly helped me to finish this work.

At first, I express my deepest and most sincere gratitude to my supervisor, Professor Shigeru Morita. I greatly appreciate his elaborate instruction, constant encouragement and valuable suggestions done during my doctor course. His physical intuition and foresight has been indispensable guidance throughout the entire thesis. Without his help, the completion of this study would not have been possible.

I gratefully acknowledge Dr. Motoshi Goto for his essential support in experimental works and for the helpful suggestions on data analysis and visible spectroscopy. My appreciation is extended to Dr. Malay Bikas Chowdhuri, Ms. Chunfeng Dong, and Mr. Jun Yanagibayashi for their help.

I wish to express sincere gratitude to Dr. I. Yamada for his help on Thomson data, Dr. R. Sakamoto for his information on pellet injection, Prof. K. Y. Watanabe for his discussion on VMEC data, Dr. M. Koubiti for his knowledge on atomic physics, and Dr. S. Muto for his kind help. I also wish to express my appreciation to all members of LHD experimental group and staffs of NIFS and the Graduate University of Advance Studies (SOKENDAI) for their supports. I would like to acknowledge the financial support over three years by Japanese Government (MEXT) Research Student Scholarship.

I am deeply grateful to Professors Zhengying Cui and Yong Liu in Southwestern Institute of Physics (SWIP), Chengdu, China, for their help and encouragements to this PhD. study. In particular, my special thanks go to Professor Qingwei Yang, my supervisor in SWIP, for his guidance during my master course and his essential support for the overseas education. I also appreciate all the staffs in SWIP for their help.

Finally, my great thanks are expressed to all my family for their supports and encouragements. I would like to express great thanks to my father and mother for their endless supports and attentions. I heartily appreciate Ms. Chunfeng Dong for her constant mental support and encouragement. My sincere gratitude is expressed to my uncle’s family, my aunt’s family and my younger aunt’s family for their supports.

Publications

(1) “Z_{eff} profile measurement system with an optimized Czerny–Turner visible spectrometer in large helical device”,
H. Y. Zhou, S. Morita, M. Goto and M. B. Chowdhuri
Review of Scientific Instruments **79** (2008) 10F536-1-3.

(2) “Application of Z_{eff} profile analysis based on visible bremsstrahlung measurement to different density profiles in the LHD”,
H. Y. Zhou, S. Morita, M. Goto, K. Narihara and I. Yamada
Plasma Fusion Research **5** (2010) S1021-1-6.

(3) “Z_{eff} profile diagnostics using visible bremsstrahlung continuum for nonaxisymmetric plasmas with finite β in large helical device”,
H. Y. Zhou, S. Morita, M. Goto and C. F. Dong
Journal of Applied Physics **107** (2010) 053306-1-11.

(4) “Z_{eff} measurement using EUV bremsstrahlung emission in LHD”,
H. Y. Zhou, S. Morita, M. Goto, C. F. Dong, J. Yanagibayashi and M. Hasuo
To be published in Review of Scientific Instruments **81** (2010).

(5) “Investigation on total bremsstrahlung radiation in high-density operation of LHD based on visible bremsstrahlung profile measurement”,
H. Y. Zhou, S. Morita, M. Goto and C. F. Dong
To be published in Japanese Journal of Applied Physics **49** (2010).